

INFRARED OPTICAL PARAMETRIC  
FLUORESCENCE AND PARAMETRIC OSCILLATION

THESIS

by

James E. Pearson

In Partial Fulfillment of the Requirements  
for the Degree of  
Doctor of Philosophy

California Institute of Technology  
Pasadena, California

1972

(Submitted May 16, 1972)

#### ACKNOWLEDGMENTS

The success of this research resulted from the contributions of many people. I would first like to thank my research advisor, Dr. Amnon Yariv; his talents and encouragement have served as the stimuli for my research. I am also indebted to Dr. Uri Ganiel of the Weizmann Institute of Science, Rehovot, Israel. His valuable assistance while working as a Postdoctoral Fellow at Caltech contributed a great deal to the initial parametric fluorescence work and to the operation of the first parametric oscillator. His enthusiasm and friendship will be remembered far beyond this research.

I would like to thank Mr. Gary Evans for construction of the Nd:YAG laser used in the later experiments and for his assistance in some of the parametric fluorescence measurements. I wish him success in his future graduate work. The able technical assistance of Mr. Desmond Armstrong was also invaluable in solving numerous problems with the experimental apparatus.

During the course of this work, our research group has had the good fortune of a close working relationship with the Hughes Research Laboratories in Malibu, California. I would like to thank those of Hughes Research who made this arrangement possible and in particular, Dr. Viktor Evtuhov and Dr. David Tseng. Their technical advice and helpful discussions were greatly appreciated.

Every research project requires financing and this one had a generous benefactor in General Dynamics' Pomona Division. Their contract support over the last three years made possible the large capital

expenditures necessary to start up a nonlinear optics research effort. The personal financial aid that I received from the Fannie and John Hertz Foundation is also gratefully acknowledged. The Foundation's generous support made the burdens of graduate life much easier to bear.

My thanks go also to the secretaries in the Electrical Engineering Department. Without the skill and patience of Mrs. Ruth Stratton, Mrs. Aldré Khoury, and Mrs. Karen Current, the many onrushing deadlines would never have been met.

The greatest debt is acknowledged last. The encouragement, love, and understanding of my wife, Nanci, made the hard times easier and the good times that much better. The importance of her contribution to all my graduate work is beyond measure.

## ABSTRACT

The properties of optical parametric fluorescence and parametric oscillation are considered in detail. Parametric fluorescence occurs when a pump light source (usually a laser) is incident on a nonlinear crystal; an input pump photon is "split" into two new photons whose energies sum to that of the pump. The frequencies of the fluorescence output can be tuned by varying the nonlinear crystal refractive indices. In a parametric oscillator, an optical resonator is used to provide feedback at the fluorescence frequencies so that coherent oscillations occur. The result is a coherent, narrow bandwidth light source which is wavelength-tunable over thousands of angstroms.

For use in theoretical discussions, the nonlinear equations which describe three-wave parametric interactions are derived from Maxwell's equations. The interaction equations are given in a general form which exhibits the spatial and temporal dependence of the fields. The equations are solved for the case of a steady-state, non-depleted pump, parametric amplifier.

The power, bandwidth, and angular dependence of parametric fluorescence are theoretically discussed in detail. Experimental measurements using a  $1.06\mu$ , Nd:YAG laser are in good agreement with the theory. The experiments constitute the first observation of parametric fluorescence in the infrared.

The theoretical properties of parametric oscillators are discussed using a simple but rigorous Fabry-Perot analysis. The analysis gives the threshold and oscillation frequencies of a parametric oscillator and the results are used to provide some insights into an oscillator's bandwidth and stability. The rise time of a pulsed parametric oscillator driven by a Q-switched pump is analyzed rigorously for the first time. The analysis gives a minimum peak pump power for oscillation which can be substantially larger than the "cw" threshold power.

Measurements on a  $1.06\mu$ -pumped, internal,  $\text{LiNbO}_3$  parametric oscillator are presented. The threshold, bandwidth, mode spectra, tuning range, and time behavior are discussed and compared to theory. The experimental results show good qualitative agreement with theory except that the bandwidth is nearly an order of magnitude smaller than expected. Peak power conversion efficiencies of 50% are observed along with 10% average power conversion. Several suggestions are made for improving the performance of this type of parametric oscillator.

TABLE OF CONTENTS

	Page
ACKNOWLEDGMENTS	ii
ABSTRACT	iv
TABLE OF CONTENTS	vi
1. INTRODUCTION	1
Chapter 1 References	5
2. NONLINEAR INTERACTION EQUATIONS	
A. Introduction	6
B. Derivation of the Interaction Equations	7
C. Steady-State Solution	15
Chapter 2 References	19
3. OPTICAL PARAMETRIC FLUORESCENCE	
A. Introduction	21
B. Theory	23
C. Fluorescence Power	28
D. Bandwidth	37
E. Experimental Measurements	38
Chapter 3 References	48
4. PARAMETRIC OSCILLATOR: THEORY	
A. Introduction	51
B. Fabry-Perot Analysis of a Parametric Oscillator	51
C. Oscillation Threshold	56
D. Rise Time of Pulsed Parametric Oscillators	67
E. Oscillator Bandwidth and Stability	84

Chapter 4	References	92	
5.	1.06 $\mu$ -PUMPED OPTICAL PARAMETRIC OSCILLATION		
A.	Introduction	95	
B.	Oscillator Design	96	
C.	Prediction of OPO Tuning Characteristics	98	
D.	Experimental Oscillator Tuning Characteristics	101	
E.	Oscillator Threshold	103	
F.	Output Power and Efficiency	107	
G.	Oscillator Bandwidth and Spectra	110	
H.	Time Behavior		
I.	Suggestions for Improving Oscillator Performance	118	
	Chapter 5	References	120
6.	CONCLUSION	124	
APPENDICES			
I.	Effective Nonlinear Coefficients	128	
	Appendix I	References	135
II.	Mode-Coupling Coefficients for Parametric Interactions	136	
	Appendix II	References	143
III.	Optimum Laser Output Coupling Using Internal		
	Optical Parametric Oscillation	144	
	Appendix III	References	150

## Chapter 1

### INTRODUCTION

The first coherent light source flashed on in 1960 [1]. Since that first demonstration of a ruby laser by Maiman, many successful efforts have been made to improve laser operation, to increase the number of available wavelengths, and to apply this intense light source to the solution of practical as well as research problems. One such success was the demonstration of second-harmonic generation by Franken, et al in 1961 [2]. Each laser was then capable of producing at least two frequencies if suitable doubling materials could be found. Another major advance occurred in 1965 when Giordmaine and Miller reported the observation of optical parametric oscillation [3]. Driven by a laser, the optical parametric oscillator produces a coherent light output which has all the properties of ordinary laser light but which can be continuously tuned over a wide wavelength range. By using parametric oscillators, tunable coherent light can now be produced at wavelengths ranging from the infrared at  $9.6\mu$  [4] all the way through the visible region to  $0.4\mu$  [5,6]. The advent of the parametric oscillator has thus greatly increased the useful potential of the laser.

This thesis discusses many of the properties of the optical parametric oscillator (OPO) and of the basic physical process which drives it, optical parametric fluorescence. For those who are unfamiliar with this new and rapidly changing area of quantum electronics and nonlinear optics, the following list briefly defines some of the terms which appear frequently in subsequent chapters.

1. Nonlinear crystal. Parametric oscillation can occur because some materials have a nonzero, nonlinear component in the dielectric polarization. That is,  $P = \epsilon E + dE^2$  and  $d \neq 0$ . Any material which lacks inversion symmetry can have this property and is called "nonlinear". For OPO applications, high optical quality is required so all materials used to date have been crystals\*. In addition, the crystals used so far have been birefringent so that "phase-matching" can be achieved (see item 4 below). This last restriction has severely limited the number of crystals which can be successfully used in parametric oscillators.

2. Pump, signal, and idler. These terms are carry-overs from microwave parametric devices; they name the laser which drives the OPO (the pump) and the two lower frequencies which are produced by the parametric interaction. By convention, the signal frequency is greater than or equal to the idler frequency.

3. Doubly-resonant and singly-resonant. An OPO is constructed by using a high-Q optical cavity to provide feedback at the signal frequency and perhaps also at the idler frequency. If the optical cavity is resonant at both the signal and idler frequencies, the OPO is called "doubly-resonant". If feedback occurs at only one frequency (either signal or idler), the OPO is "singly-resonant".

4. Phase-matching. In normally-dispersing materials, the polarization wave generated by the nonlinear mixing of two fields will

---

\* See Ref. 7 for a good summary of nonlinear materials available up to 1970.

usually travel at a different velocity than the "free" wave it radiates. The fields produced at different points in the material will thus be out of phase and will interfere destructively throughout most of the material. This interference will prevent efficient parametric interactions. Giordmaine [8] and Maker, et al [9] simultaneously realized that the use of birefringent materials could eliminate this problem. By suitably selecting the polarization directions of the interacting fields, the phase velocities of the waves could be made equal. This equalizing of phase velocities is known as "phase-matching" or "index-matching" since the phase velocity is related to the index of refraction.

5. Phase-matching angle. The two different waves which can propagate in a birefringent material are known as the "extraordinary wave" and the "ordinary wave". The index of refraction seen by the extraordinary wave can be changed by changing the direction the wave propagates through the crystal [10]. The angle between the z(optic)-axis of the crystal and the extraordinary wave vector is called the "phase-matching angle". In most parametric oscillators, this angle is the one between the pump propagation direction and the crystal z-axis.

This brief introduction should help to clarify some of the discussions in subsequent chapters. The following chapter uses Maxwell's equations to derive the nonlinear interaction equations which describe a general three-wave interaction in a nonlinear material. A steady-state solution for the optical parametric amplifier is also presented. Chapter 3 discusses the properties of optical parametric fluorescence. After a review of the basic theoretical

aspects, experimental results in the infrared are compared to theory with good agreement. The experimental observations constitute the first measurements of optical parametric fluorescence in the infrared.

Chapter 4 discusses theoretically the important parameters of parametric oscillators including threshold, rise time and bandwidth. The OPO threshold is found using a simple but highly useful Fabry-Perot analysis. The risetime of a pulsed parametric oscillator driven by a Q-switched laser is derived rigorously for the first time. Chapter 5 presents observations on the properties and operating characteristics of a  $1.06\mu$ -pumped parametric oscillator. Good power conversion efficiencies are reported and suggestions are made for further improving the performance of this type of OPO.

Chapter 1

References

1. T. H. Maiman, "Stimulated Optical Radiation in Ruby", *Nature* 187, pp. 493-494 (1960).
2. P. A. Franken, A. E. Hill, C. W. Peters, and G. Weinreich, "Generation of Optical Harmonics", *Phys. Rev. Lett.* 7, pp. 118-119 (1960).
3. J. A. Giordmaine and R. C. Miller, "Tunable Coherent Parametric Oscillation in  $\text{LiNbO}_3$  at Optical Frequencies", *Phys. Rev.* 14, pp. 973-976 (1965).
4. R. L. Herbst and R. L. Byer, "CdSe Infrared Parametric Oscillator" presented at the VII International Quantum Electronics Conference in Montreal, Canada, May 1972.
5. R. W. Wallace, "Stable, Efficient, Optical Parametric Oscillators Pumped with Doubled Nd:YAG", *Appl. Phys. Lett.* 17, pp. 491-499 (1970).
6. J. M. Yarborough and G. A. Massey, "Efficient High-Gain Parametric Generation in ADP Continuously Tunable Across the Visible Spectrum", *Appl. Phys. Lett.* 18, pp. 438-440 (1971).
7. R. Bechmann and S. K. Kurtz, "Second Harmonic Generation in Crystalline Solids" in Landolf-Börnstein, Group III: Crystal and Solid State Phys., Vol. 1 (Springer-Verlag, Berlin, 1970), pp. 167-232.
8. J. A. Giordmaine, "Mixing of Light Beams in Crystals", *Phys. Rev. Lett.* 8, pp. 19-20 (1962).
9. P. D. Maker, R. W. Terhune, M. Nisenoff, and C. M. Savage, "Effects of Dispersion and Focusing on the Production of Optical Harmonics", *Phys. Rev. Lett.* 8, pp. 21-22 (1962).
10. See, for example, A. Yariv, Quantum Electronics (John Wiley and Sons, New York, 1967), Chap. 18.

## Chapter 2

### NONLINEAR INTERACTION EQUATIONS

#### A. Introduction

This chapter is devoted to deriving the differential equations which describe the changes in an optical field due to a nonlinear polarization. Previous derivations of the nonlinear interaction equations either have assumed steady-state, harmonic-time dependence [1,2], considering only spatial variations, or have expanded the fields in eigenmodes of a cavity resonator [3,4], thus treating only the time variation of the field amplitudes. Phase considerations have been limited to the case of constant phase, with the relative phase between the waves chosen for maximum power transfer between the fields. In general, both the amplitude and phase of a wave driven by a nonlinear polarization can vary and such variations can occur both in space and in time. The derivation presented here gives the interaction equations in a general form which allows for both temporal and spatial variations in the phase as well as the amplitude of the separate fields.

To derive the interaction equations, a nonlinear polarization term proportional to the square of the total electric field is added to Maxwell's equations. Using various approximations, the equations are then simplified to find the coupled equations describing the changes in the electric fields of interest. A steady-state solution of these equations concludes the chapter.

## B. Derivation of the Interaction Equations

The starting point in the derivation is Maxwell's equations in MKS units for a polarizable, charge-free medium:

$$\nabla \times \vec{H} = \frac{\partial \vec{D}}{\partial t} + \vec{J} \quad (2.1)$$

$$\nabla \times \vec{E} = -\frac{\partial \vec{B}}{\partial t} \quad (2.2)$$

$$\nabla \cdot \vec{D} = 0 \quad (2.3)$$

$$\nabla \cdot \vec{B} = 0 \quad (2.4)$$

The necessary constitutive relations are

$$(a) \quad \vec{D} = \epsilon_0 \vec{E} + \vec{P}$$

$$(b) \quad \vec{B} = \mu \vec{H}$$

$$(c) \quad \vec{J} = \sigma \vec{E} \quad (2.5)$$

Substituting Eq. (2.1) in (2.2) and using (2.5) gives the vector wave equation,

$$-\nabla \times \nabla \times \vec{E} = \nabla^2 \vec{E} - \nabla(\nabla \cdot \vec{E}) = \mu_0 \sigma \frac{\partial \vec{E}}{\partial t} + \mu_0 \frac{\partial^2}{\partial t^2} (\vec{\epsilon} \cdot \vec{E}) + \mu_0 \frac{\partial^2 \vec{P}_{NL}}{\partial t^2} \quad (2.6)$$

where  $\sigma = \sigma(\omega)$ ,  $\mu = \mu_0$ , and the tensor quantities in (2.6) are defined by

$$(a) \quad [\epsilon(\omega)]_{ij} = \epsilon_0 \{ \delta_{ij} + [\chi_L(\omega)]_{ij} \}$$

$$(b) \quad (P_{NL})_i = d_{ijk} E_j E_k$$

$$(c) \quad \vec{D} = \tilde{\epsilon} \cdot \vec{E} + \vec{P}_{NL} \quad . \quad (2.7)$$

The subscripts  $i$ ,  $j$ , and  $k$  refer to arbitrary cartesian directions and summation is assumed on repeated indices. Equation (2.7c) is a direct result of Eqs. (2.5a), (2.7a), and (2.7b). The quantity  $\chi_L(\omega)$  is the usual linear dielectric susceptibility,  $\sigma(\omega)$  is an "effective conductivity" to account for any losses, and the nonlinear polarization term is  $\vec{P}_{NL}$ . The origins of the nonlinear polarization have been discussed by a number of authors [1,4,6] so in this discussion, the nonlinear term is a given quantity. Although Eq. (2.3) requires  $\nabla \cdot \vec{D} = 0$ , for most applications the anisotropic character of the medium can be neglected so that  $\nabla \cdot \vec{D} \approx \epsilon \nabla \cdot \vec{E} = 0$ . Making this assumption assumes that  $\vec{D}$  and  $\vec{E}$  are parallel (or equivalently,  $\chi_{ij} \approx \chi \delta_{ij}$  where  $\chi$  is the total optical susceptibility). This assumption is not strictly true in an anisotropic medium, so in order to trace the polarization source for each component of a radiated wave back to the wave equation, Eq. (2.6), the following analysis must be carried out in general vector form with  $\nabla \cdot \vec{D} = 0$  and  $\vec{D}$  given by Eq. (2.7c). An analysis of this type is given in Ref. 1 and an example of when such considerations might be important is given in Ref. 7. In the following treatment, this complication is ignored since it adds only a small and unimportant correction to the final result. Elimination of the  $\nabla \cdot \vec{E}$  term in Eq. (2.6) also allows the vector nature of the differential equation to be removed.

The following assumptions about the fields of interest are also useful:

1) The field amplitude and phase variations occur only in the direction of propagation, taken as the z-direction for each wave (not the same as the z(optic)-axis of the crystal). When double refraction effects are present, this assumption is not strictly true, since energy flows in a direction normal to the index surface. Here such problems are neglected by assuming the fields extend far enough in the transverse (x and y) directions so that spatial separation of the waves does not occur. The influence of double refraction on parametric gain is discussed in Ref. 8. All differences in propagation direction will be included in the phase mismatch  $\Delta k$  discussed below.

2) Time variations are nearly harmonic and consequently only fluctuations slow compared with the optical frequency are considered.

3) The phase fronts are planar, although a general transverse variation of the fields will be retained. This assumption is equivalent to a near-field approximation for Gaussian beams wherein diffraction effects are neglected. The transverse beam profile is thus independent of z and the phase is independent of the transverse coordinates x and y.

4) There are only three fields of interest designated the "signal", "idler", and "pump" and represented by subscripts 1, 2, and 3. The frequencies of the three fields obey the relationship  $\omega_3 = \omega_1 + \omega_2$  and by convention,  $\omega_3 > \omega_1 > \omega_2$ .

With the above assumptions, the fields can be written as

$$(a) \quad \vec{E}_j(\omega_j, \vec{k}_j, x, y, z, t) = \frac{1}{2} \vec{E}_j(x, y, z, t) e^{i(\omega_j t - k_j z)} + \text{complex conjugate}]$$

$$(b) \vec{E}_j(x,y,z,t) = \vec{E}_j(x,y,z,t) e^{i\phi_j(z,t)}, \quad j = 1,2,3 \quad (2.8)$$

The quantities  $\omega_j$  and  $k_j$  are chosen so that in the absence of losses and the nonlinear interaction ( $\sigma = 0, \vec{P}_{NL} = 0$ ), the wave equation is satisfied when  $\vec{E}_j(r,z,t) = \text{constant vector}$  and  $\phi_j(z,t) = \text{constant}$ . This implies the relationship

$$k_j^2 = \mu_0 \epsilon_j \omega_j^2 \quad (2.9)$$

The previous assumption of  $\nabla \cdot \vec{E} = 0$  allows the linear dielectric constant to be defined as  $\epsilon_j = \epsilon_0 (1 + \chi_j(\omega_j))$ . The complex amplitudes  $\vec{E}_j(r,z,t)$  in Eq. (2.8) are the traveling wave amplitudes and thus for resonant fields are only half of the maximum field amplitude.

The wave equation must be satisfied separately for each frequency of interest. Equivalently, "nonsynchronous" terms which vary at optical frequencies other than those satisfying  $\omega_3 = \omega_1 + \omega_2$  will average to zero over periods long compared to an optical cycle but short compared to time variations of  $\vec{E}_j(r,z,t)$ . Consider first the signal wave of frequency  $\omega_1$ . The assumption that the field amplitudes vary slowly in one wavelength and during one optical cycle can be written as

$$(a) \quad \frac{\partial^2 \vec{E}_1}{\partial z^2} \ll k_1 \frac{\partial \vec{E}_1}{\partial z} \quad (2.10)$$

$$(b) \quad \frac{\partial^2 \vec{E}_1}{\partial t^2} \ll \omega_1 \frac{\partial \vec{E}_1}{\partial t} \quad .$$

All derivatives of the nonlinear polarization are neglected so that

$$\frac{\partial^2 \vec{P}_{NL}(\omega_j)}{\partial t^2} = -\omega_j^2 \vec{P}_{NL} .$$

Putting Eqs. (2.8) and (2.9) into Eq. (2.6) and using the above assumptions gives

$$\begin{aligned} \frac{\partial \vec{E}_1}{\partial z} + \frac{n_1}{c} \left(1 - \frac{i\sigma_1}{2\epsilon_1\omega_1}\right) \frac{\partial \vec{E}_1}{\partial t} + \frac{\sigma_1 n_1}{2\epsilon_1 c} \vec{E}_1 = \\ - \frac{i\omega_1 n_1}{2\epsilon_1 c} \vec{E}_2^* \vec{E}_3 e^{-i\Delta k z} \end{aligned} \quad (2.11)$$

where  $\Delta k = |\vec{k}_3 - \vec{k}_1 - \vec{k}_2|$  is the phase-mismatch,  $\sqrt{\mu_0 \epsilon_1} = n_1/c$  and  $n_1$  is the index of refraction at  $\omega_1$ .

A brief diversion is useful at this point to discuss the mismatch term  $\Delta k$ . Examination of Eq. (2.11) shows that if  $\Delta k \neq 0$ , the contributions to the signal mode amplitude from differential path elements  $dz$  will get out of phase and interfere destructively in a distance  $l_c = \pi/\Delta k$ . This distance is known as the "coherence length." On the other hand, if  $\Delta k = 0$ , the entire nonlinear crystal acts as a phase-arrayed dipole radiating in the direction of propagation. The condition  $\Delta k = 0$  is equivalent to requiring that the phase velocity of the nonlinear polarization wave equal that of the radiated (free) wave in the crystal. Consequently, the requirement  $\Delta k = 0$  is known as the "phase-matching" condition or, since  $k = n\omega/c$ , as "index matching".

The index-matching condition  $\Delta k = 0$  is always satisfied in vacuum, but is ordinarily not possible in normally dispersive materials where  $n(\omega)$  increases with  $\omega$ . Giordmaine [9], and Maker, et al [10],

however, concurrently realized that index-matching could be achieved in birefringent materials by suitably selecting the direction of propagation and the polarizations of the fields (see Appendix I).

A unique set of polarizations  $\vec{e}^1$ ,  $\vec{e}^2$ , and  $\vec{e}^3$  for the three modes is now selected on the basis of the nonlinear crystal class and the desired parametric process. An effective nonlinear coupling coefficient can thus be defined by

$$d = d_{ijk} e_i^1 e_j^2 e_k^3 \quad (2.12)$$

where  $i$ ,  $j$ , and  $k$  refer to cartesian directions and summation is implied by repeated indices. The exact form of  $d$  for various crystals of interest is given in Appendix I.

When the distributed losses represented by  $\sigma_j/\epsilon_j$  at each frequency are small,  $\sigma_j/2\omega_j\epsilon_j \approx 0$ . The resulting equation describing the time and spatial dependence of the complex field amplitude at  $\omega_1$  is

$$\frac{\partial E_1}{\partial z} + \frac{n_1}{c} \frac{\partial E_1}{\partial t} + a_1 E_1 = - \frac{i\omega_1 dn_1}{2\epsilon_1 c} E_2^* E_3 e^{-i\Delta kz} \quad (2.13)$$

where  $a_1 = n_1\sigma/(2\epsilon_1 c)$  is the fractional field loss per unit distance at  $\omega_1$ .

A useful normalization for the field amplitude at  $\omega_j$  is defined by

$$E_j(x,y,z,t) = \left(\frac{\omega_j}{n_j}\right)^{1/2} u_j(x,y) A_j(z,t) \quad (2.14)$$

The transverse dependence of the fields has been explicitly factored out in the function  $u_j(x,y)$ . The amplitudes  $A_j$  have the useful physical significance that  $A_j^2$  is proportional to the photon flux (photons/sec) at the frequency  $\omega_j$ . The transverse functions  $u_j(x,y)$  are normalized so that

$$\int_{-\infty}^{\infty} \int_{-\infty}^{\infty} u_j^2(x,y) dx dy = 1 \quad (2.15)$$

With this normalization the time-averaged power at  $\omega_j$  (averaged over an optical cycle) is  $P_j = \frac{1}{2} \epsilon_0 c \omega_j |A_j|^2$ .

When (2.14) is put in Eq. (2.13), and Eq. (2.15) is used to integrate out the transverse dependence, the final expression is

$$\frac{\partial A_1}{\partial z} + \frac{n_1}{c} \frac{\partial A_1}{\partial t} + a_1 A_1 = -i \Gamma A_2^* A_3 e^{-i \Delta k z} \quad (2.16)$$

where

$$\Gamma = \frac{d}{2} \left( \frac{\omega_1 \omega_2 \omega_3 \mu_0}{n_1 n_2 n_3 \epsilon_0} \right)^{1/2} I \quad (2.17)$$

and

$$I = \int_{-\infty}^{\infty} \int_{-\infty}^{\infty} u_1 u_2 u_3 dx dy \quad (2.18)$$

The value of  $I$  is evaluated in Appendix II for various combinations of the functions  $u_j$ .

A similar derivation gives the equations for the idler and pump fields. The results are given in Eqs. (2.19) and (2.20):

$$\frac{\partial A_2^*}{\partial z} + \frac{n_2}{c} \frac{\partial A_2^*}{\partial t} + a_2 A_2^* = i\Gamma A_1 A_3^* e^{i\Delta kz} \quad (2.19)$$

$$\frac{\partial A_3}{\partial z} + \frac{n_3}{c} \frac{\partial A_3}{\partial t} + a_3 A_3 = -i\Gamma A_1 A_2 e^{i\Delta kz} \quad (2.20)$$

The phase variation can be treated separately by using Eq. (2.8b) in Eqs. (2.16), (2.19), and (2.20). The resulting equations for the real amplitudes and phases are

$$(a) \quad \frac{\partial A_1}{\partial z} + \frac{n_1}{c} \frac{\partial A_1}{\partial t} + a_1 A_1 = \Gamma A_2 A_3 \sin \theta(z)$$

$$(b) \quad \frac{\partial A_2}{\partial z} + \frac{n_2}{c} \frac{\partial A_2}{\partial t} + a_2 A_2 = \Gamma A_1 A_3 \sin \theta(z)$$

$$(c) \quad \frac{\partial A_3}{\partial z} + \frac{n_3}{c} \frac{\partial A_3}{\partial t} + a_3 A_3 = -\Gamma A_1 A_2 \sin \theta(z)$$

$$(d) \quad \frac{\partial \theta}{\partial z} + \frac{1}{c} \frac{\partial}{\partial t} (n_3 \phi_3 - n_1 \phi_1 - n_2 \phi_2) \\ = -\Delta k + \Gamma \left( \frac{A_1 A_3}{A_2} + \frac{A_2 A_3}{A_1} - \frac{A_1 A_2}{A_3} \right) \cos \theta(z) \quad (2.21)$$

where  $\theta(z) = \phi_3(z, t) - \phi_1(z, t) - \phi_2(z, t) - \Delta kz = \Delta\phi - \Delta kz$  and all second order terms in  $\phi$  such as  $(\partial\phi/\partial t)^2$  and  $\partial^2\phi/\partial t^2$  have been neglected. Equation (2.21d) is actually a sum of three equations combined to exhibit the functional dependence of  $\Delta\phi$ .

Equations (2.21) are very similar to the amplitude and phase equations derived by Lamb [11] using the concept of cavity modes in Maxwell's equations. In Lamb's analysis  $\partial E/\partial z$  and  $\partial\phi/\partial z$  are both zero, with the only spatial variation of the fields occurring in the

cavity modes. In addition, there is a "mode-pulling" term on the left-hand side of the phase equation, (Eq. (21d) above)). This term is  $(\omega_1 - \Omega_{1m})$  where  $\omega_1$  is the actual oscillating frequency and  $\Omega_{1m} = \frac{\pi mc}{L}$  is the  $m^{\text{th}}$  cavity mode frequency for a cavity of length  $L$ . Although frequency-pulling effects may be important in determining the exact frequency of a resonant field, such complications are neglected here. Note that in the present treatment, a finite value for  $\Delta k$  can play the same role as the frequency-pulling term in Lamb's equations.

Equations (2.16) - (2.21) are the principal results of this section. These equations can now be used to derive various properties of three-wave optical parametric interactions.

### C. Steady-State Solution

The steady-state solution to Eqs. (2.21) is the simplest case to consider and gives some insights to the characteristics of three-wave parametric interactions. In order to further simplify the solution of the equations, the pump field is assumed to be unaffected by the interaction (nondepleted pump) and each field amplitude is allowed to carry its own phase. The small gain solutions found with these approximations have a particularly simple form and are useful in discussing parametric fluorescence and in calculating the threshold of a parametric oscillator. Steady-state solutions which include pump depletion are given in Ref. 1.

The equations to be solved are Eqs. (2.16) and (2.19) with  $\partial/\partial z = 0$  :

$$(a) \quad \frac{\partial A_1}{\partial z} = -ig A_2^* e^{-i\Delta kz}$$

$$(b) \quad \frac{\partial A_2^*}{\partial z} = ig^* A_1 e^{i\Delta kz} \quad (2.22)$$

where

$$g = \Gamma A_3 \quad (2.23)$$

All losses in the nonlinear material have been neglected so  $a_1 = a_2 = 0$ . The solution of Eqs. (2.22) is facilitated by the substitutions [7]

$$\begin{aligned} A_1(z) &= m_1 \exp(\gamma - i \frac{\Delta k}{2}) z \\ A_2^*(z) &= m_2^* \exp(\gamma + i \frac{\Delta k}{2}) z \end{aligned} \quad (2.24)$$

where  $m_1$  and  $m_2^*$  are independent of  $z$ . Substitution of Eq. (2.24) in Eq. (2.22) gives a determinantal equation for  $\gamma$  whose solution is

$$\gamma^2 = g^2 - (\frac{\Delta k}{2})^2 \quad (2.25)$$

The boundary conditions are taken to be

$$A_j(0) = A_{j0} e^{i\phi_{j0}}, \quad j = 1, 2, 3 \quad (2.26)$$

where the amplitudes  $A_{j0}$  and phases  $\phi_{j0}$  are real quantities. Using these boundary conditions and solving for the fields at the output of the nonlinear crystal gives

$$\begin{aligned} A_1(\ell) &= (\alpha A_{10} + \beta^* A_{20}) e^{i\phi_{10}} \\ A_2^*(\ell) &= (\alpha^* A_{20} + \beta A_{10}) e^{-i\phi_{20}} \end{aligned} \quad (2.27)$$

where

$$\alpha = (\cosh \gamma \ell + \frac{i\Delta k}{2\gamma} \sinh \gamma \ell) \exp(-\frac{i\Delta k \ell}{2})$$

$$\beta = \frac{ig}{\gamma} \sinh \gamma \ell \exp[-i(\Delta\phi - \frac{\Delta k \ell}{2})] \quad . \quad (2.28)$$

The nonlinear crystal length is  $\ell$  and  $\Delta\phi = \phi_{30} - \phi_{10} - \phi_{20}$  is the initial value of the relative phase. Note that when  $\Delta k \neq 0$ ,  $\Delta\phi(\ell) \neq \Delta\phi$  as expected from Eq. (2.21d). For collinear propagation, the phase-mismatch is

$$\Delta k = k_3 - k_1 - k_2 = \frac{1}{c}(n_3\omega_3 - n_1\omega_1 - n_2\omega_2) \quad . \quad (2.29)$$

Equations (2.27) and (2.28) are the solutions for a low-gain parametric amplifier with inputs at both  $\omega_1$  and  $\omega_2$ .

An optimum value for the initial relative phase can be found by examining the signal output power. From Eq. (2.27) the signal power at  $z = \ell$  is

$$P_1(\ell) \propto |A_1(\ell)|^2 = A^2 + B^2 + 2AB \sin(\Delta\phi - \xi) \quad (2.30)$$

where

$$A^2 = |\alpha A_{10}|^2 = A_{10}^2 (1 + \frac{g^2}{\gamma^2} \sinh^2 \gamma \ell) \quad (2.31)$$

$$B^2 = |\beta A_{20}|^2 = A_{20}^2 \frac{g^2}{\gamma^2} \sinh^2 \gamma \ell \quad (2.32)$$

and

$$\xi = \tan^{-1}(\frac{\Delta k}{2\gamma} \frac{\sinh \gamma \ell}{\cosh \gamma \ell}) \quad . \quad (2.33)$$

The signal power will be maximum when  $\Delta\phi - \xi = \pi/2$ . Consequently, the optimum relative phase  $\Delta\phi_m$  is

$$\cot \Delta\phi_m = -\tan \xi = -\frac{\Delta k}{2\gamma} \tanh \gamma \ell \quad . \quad (2.34)$$

This result has also been derived by Smith [12]. The maximum signal power is

$$[P_1(\ell)]_{\max} = P_{10} + \left( P_{10} + \frac{\omega_1}{\omega_2} P_{20} \right) f^2 + 2 \left( \frac{\omega_1}{\omega_2} P_{10} P_{20} \right)^{\frac{1}{2}} f (1+f^2)^{\frac{1}{2}} \quad (2.35)$$

where

$$f = \frac{g}{\gamma} \sinh \gamma \ell \quad (2.36)$$

and  $P_{j0} = \epsilon_0 c \omega_j A_{j0}^2 / 2$  is the input power at  $\omega_j$ . Inputs at either  $\omega_1$  or  $\omega_2$  will be amplified to produce an output at  $\omega_1$ . Of course, the same conclusion also holds for the field at  $\omega_2$ .

If the one or both of the inputs to a parametric amplifier have randomly varying phases or if the pump phase fluctuates (non-coherent pump [13,14]),  $\Delta\phi$  will be a randomly varying function of time. In this case, there is no correlation between the inputs at  $\omega_1$  and  $\omega_2$  and the last term in Eq. (2.30) will average to zero. The net effect is to reduce the gain of the parametric amplifier [14]. The signal output power in this case is

$$P_1(\ell) = P_{10} + \left( P_{10} + \frac{\omega_1}{\omega_2} P_{20} \right) \frac{g^2}{\gamma^2} \sinh^2 \gamma \ell \quad (2.37)$$

The travelling-wave parametric amplifier will thus work even for completely incoherent sources although the gain is less than when the inputs are perfectly coherent.

Chapter 2

References

1. J. A. Armstrong, N. Bloembergen, J. Ducuing, and P. S. Pershan, "Interactions between Light Waves in a Nonlinear Dielectric", Phys. Rev. 127, pp. 1918-1939 (1962).
2. A. Yariv, Quantum Electronics (John Wiley and Sons, Inc., New York, 1967), Chapter 21.
3. W. H. Louisell, A. Yariv, and A. E. Siegman, "Quantum Fluctuations and Noise in Parametric Processes. I", Phys. Rev. 124, pp. 1646-1654 (1961).
4. R. L. Byer, "Parametric Fluorescence and Optical Parametric Oscillation", Ph.D. Thesis, (available as M. L. Report No. 1711), Stanford University, 1968.
5. N. Bloembergen, Nonlinear Optics (W. A. Benjamin, Inc., New York, 1965).
6. N. Bloembergen and Y. R. Shen, "Quantum Theoretical Comparison of Nonlinear Susceptibilities in Parametric Media, Lasers, and Raman Lasers", Phys. Rev. 133, pp. A37-A49 (1964).
7. A. Yariv and J. E. Pearson, "Parametric Processes, in Progress in Quantum Electronics, Vol. 1 (Pergamon Press, 1969).
8. G. D. Boyd and D. A. Kleinman, "Parametric Interaction of Focused Gaussian Light Beams", J. Appl. Phys. 39, pp. 3597-3639 (1968).
9. J. A. Giordmaine, "Mixing of Light Beams in Crystals", Phys. Rev. Lett. 8, pp. 19-20 (1962).
10. P. D. Maker, R. W. Terhune, M. Nisenoff, and C. M. Savage, "Effects of Dispersion and Focusing on the Production of Optical Harmonics", Phys. Rev. Lett. 8, pp. 21-22 (1962).
11. W. E. Lamb, Jr., "Theory of an Optical Maser", Phys. Rev. 134, A1429-A1450 (1964).
12. R. G. Smith, "Effects of Momentum Mismatch on Parametric Gain", J. Appl. Phys. 41, pp. 4121-4124 (1970).

13. B. Crosignani, U. Ganiel, S. Solimeno and A. Yariv, "Some Consequences of Pump Coherence on Energy Exchange in Nonlinear Optical Processes," Phys. Rev. Lett. 27, pp. 237-239 (1971).
14. B. Crosignani, P. DiPorto, U. Ganiel, S. Solimeno, and A. Yariv, "The Effect of Pump Coherence on Frequency Conversion and Parametric Amplification," to be published.

Chapter 3

OPTICAL PARAMETRIC FLUORESCENCE

A. Introduction

The steady-state solution of the nonlinear interaction equations found in the preceding chapter gave the outputs of an optical parametric amplifier in terms of its inputs. An important quantity for any amplifier is the noise of the device. That is, what is the amplifier output with no external input? In a parametric amplifier, the source of the noise is a process called "optical parametric fluorescence". This fluorescence or "parametric noise" can be viewed as the nonlinear optics analog to the familiar spontaneous emission which produces the noise in a laser amplifier. The analogy goes even further. In a laser, the magnitude and spectral width of the spontaneous emission determine the gain (threshold) and the linewidth of the laser output. In a parametric oscillator, it is the parametric fluorescence which gives the threshold and bandwidth of the device.

The phenomenon of parametric fluorescence is illustrated schematically in Fig. 3-1. A pump field at  $\omega_3$  is incident on a nonlinear material and there are no other inputs. The pump interacts with the material to produce output signal ( $\omega_1$ ) and idler ( $\omega_2$ ) frequencies which satisfy the relation

$$\omega_3 = \omega_1 + \omega_2 \quad . \quad (3.1)$$

Although there are an infinite number of frequency pairs which can satisfy Eq. (3.1), the parametric output is limited by the phase-matching requirement to the frequencies and directions which can also satisfy

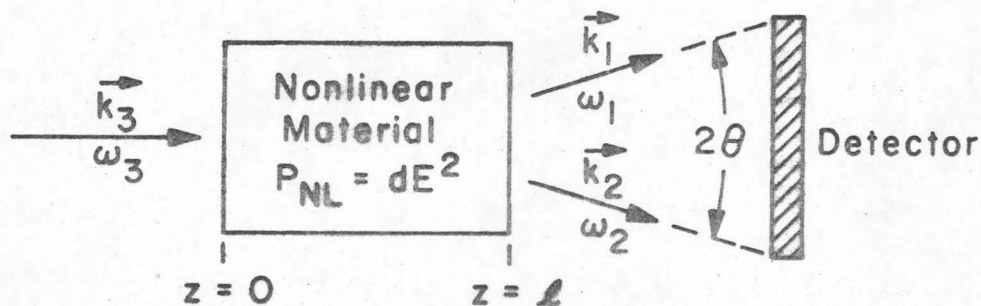


Figure 3-1. Generation of optical parametric fluorescence. The pump field at  $\omega_3$  generates new frequencies  $\omega_1$  and  $\omega_2$  by interacting with the nonlinear crystal. The detector accepts only those frequencies produced within the cone of half-angle  $\theta$ .

the condition

$$\Delta k = |\vec{k}_3 - \vec{k}_1 - \vec{k}_2| \lesssim \pi/l \quad . \quad (3.2)$$

The length of the nonlinear crystal is  $l$  and  $\vec{k}_j$  is the wave vector of the field at  $\omega_j$ .

A useful way of viewing parametric fluorescence is to consider it as a quantum-mechanical photon scattering process in the nonlinear crystal. Because of the crystal nonlinearity, there is a finite probability that an input pump photon will "spontaneously" split into two new photons. Conservation of energy then gives Eq. (3.1) and conservation of photon momentum gives Eq. (3.2) with  $\Delta k = 0$ . The process can also be viewed as parametric amplification where the amplifier inputs are the uncorrelated zero-point vibrations of the electromagnetic field. Parametric fluorescence is thus a direct demonstration of the interaction of a physical system with the zero-point energy of the electromagnetic field.

This chapter studies both theoretically and experimentally the properties of parametric fluorescence. A review of the theory of parametric fluorescence is presented first. Studies of total-emitted fluorescence power are then presented. Finally, the fluorescence bandwidth and angular distribution are studied and the theoretical predictions are confirmed by the first experimental measurements of narrow bandwidth infrared-pumped fluorescence.

### B. Theory

The phenomenon of spontaneous parametric fluorescence was first discussed in 1961 by Louisell, Yariv, and Siegman [1]. Since that time, comprehensive theoretical treatments have appeared [2-4], along with numerous experimental observations [3,5-16]. A completely rigorous theoretical treatment of parametric fluorescence requires a quantum mechanical analysis [2,4]. A semiclassical analysis gives the correct results, however, and is very appealing because of its simplicity. The following analysis follows the plane-wave theory of Byer and Harris [3].

Consider an interaction of plane waves in a parametric amplifier. The amplifier is driven by the pump field at  $\omega_3$  and has inputs at both the signal and the idler frequencies. For calculation of the signal parametric fluorescence output at  $\omega_1$ , these inputs are not externally applied but are assumed to arise from the zero-point energy of the electromagnetic field. That is, there is an input energy flux of  $\hbar\omega/2$  per blackbody mode at both  $\omega_1$  and  $\omega_2$ . The differential inputs are thus given by the product of the energy per mode multiplied by the appropriate velocity in the crystal and by the differential number of modes which can interact in the crystal. For the idler input at

$\omega_2$ , the result is

$$P_{20} = d\left(\frac{P_2}{A}\right)_0 = \frac{\hbar\omega_2 c}{2n_2} \frac{d^3 k_2}{(2\pi)^3} \quad (3.3)$$

Since this is a plane-wave analysis,  $A$  is the cross-sectional area of the crystal (or pump beam for finite beams),  $c/n_2$  is the idler velocity in the crystal, and  $\hbar$  is Planck's constant.

Using the geometry of Fig. 3-2 and assuming cylindrical symmetry

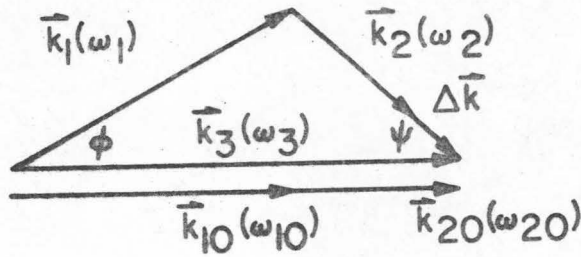


Figure 3.2 Geometry for parametric fluorescence. The collinear frequencies  $\omega_{10}$  and  $\omega_{20}$  are assumed to be exactly phase-matched ( $|\Delta k| = 0$ ).

about the pump allows the  $k_2$ -space volume differential to be written as

$$d^3 k_2 = 2\pi \sin \psi \, d\psi \, \frac{n_2^3}{c} \omega_2^2 \, d\omega_2 \quad (3.4)$$

where  $|\vec{k}_2| = k_2 = n_2 \omega_2 / c$ . From Eq. (3.1),  $d\omega_2 = -d\omega_1$  and for small angles and  $|\Delta \vec{k}| \ll k_2$ ,  $\psi \, d\psi \approx (k_1/k_2)^2 \phi \, d\phi$ . Ignoring the minus sign and using Eq. (3.4) in Eq. (3.3) gives

$$d\left(\frac{P_2}{A}\right)_0 = \frac{\hbar\omega_1^2 \omega_2^2 n_1^2}{2(2\pi)^2 c^2} \phi \, d\phi \, d\omega_1 \quad (3.5)$$

Since the signal and idler inputs are uncorrelated, Eq. (2.37) can be used to find the signal power at the output of the nonlinear crystal. Because the zero-point energy of the electromagnetic field

cannot be observed directly, the observable signal power is  $P_1(\ell) - P_{10}$ . Using the relation  $P_{10} = d(P_1/A)_0 = (\omega_1/\omega_2) d(P_2/A)_0$ , Eq. (2.37) gives the signal output as

$$d\left(\frac{P_1}{A}\right) = 2 \frac{\omega_1}{\omega_2} d\left(\frac{P_2}{A}\right)_0 \frac{g^2}{\gamma^2} \sinh^2 \gamma \ell \quad (3.6)$$

where from Eqs. (2.17) and (2.23)

$$g^2 = \Gamma^2 A_3^2 = \frac{d^2 \omega_1 \omega_2}{2 \epsilon_o^3 n_1 n_2 n_3 c^3} \left(\frac{P_3}{A}\right) \quad (3.7)$$

The results of Appendix II, Eq. (II.8), have been used to evaluate the overlap integral I and  $P_3$  is the total pump power.

The parametric gain is usually very small so  $g \ll \Delta k/2$  and  $\gamma \approx i\Delta k/2$ . Using this limit and combining Eqs. (3.5)-(3.7) gives the differential signal power at  $\omega_1$  within  $d\omega_1$  and contained in the angle  $\phi$   $d\phi$  as

$$dP_1 = K \ell^2 P_3 \operatorname{sinc}^2(\Delta k \ell / 2) \phi \, d\phi \, d\omega_1 \quad (3.8)$$

where  $\operatorname{sinc} x = \sin x/x$  and

$$K = \frac{n_1 d^2 \pi \omega_1^4 \omega_2}{2 (2\pi)^2 \epsilon_o^3 c^5 n_2 n_3} \quad (3.9)$$

Notice that the area  $A$  does not appear in Eq. (3.8);  $dP_1$  depends only on the total pump power rather than the pump intensity. The fluorescence power is thus independent of the pump area (degree of focusing) and even the pump coherence [4].

Most of the interesting properties of parametric fluorescence are contained in the phase-matching term involving  $\Delta k$ . With the geometry of Fig. 3-2, the magnitude of the phase-mismatch for small angles is given by

$$\Delta k = k_3 - k_1 - k_2 + \frac{k_1 k_3 \phi^2}{2(k_3 - k_1)} \quad (3.10)$$

Although Eq. (3.10) could be used directly in Eq. (3.8), a useful approximation is found by expanding  $k_1$  and  $k_2$  in Taylor series about the collinear phase-matched frequencies. Retaining terms up to second-order in frequency gives

$$\Delta k = -b_0 \omega - b_1 \omega^2 + G \phi^2 \quad (3.11)$$

where

$$G = \frac{k_{10} k_3}{2k_{20}} \quad (3.12)$$

$$b_0 = \left. \frac{\partial k_1}{\partial \omega_1} \right|_{\omega_{10}} - \left. \frac{\partial k_2}{\partial \omega_2} \right|_{\omega_{20}} \quad (3.13)$$

$$b_1 = \frac{1}{2} \left[ \left. \frac{\partial^2 k_1}{\partial \omega_1^2} \right|_{\omega_{10}} + \left. \frac{\partial^2 k_2}{\partial \omega_2^2} \right|_{\omega_{20}} \right] \quad (3.14)$$

The frequency in Eq. (3.11) is defined as the deviation from the collinear frequencies ( $\omega \equiv \omega_1 - \omega_{10}$ ) and the collinear frequencies are assumed to be exactly phase-matched ( $k_3 = k_{10} + k_{20}$ ).

Examination of Eq. (3.11) gives several qualitative results. The fluorescence power is emitted in a cone about the pump direction with each direction  $\phi$  defining a different phase-matched frequency. For  $b_0 > 0$ , higher frequencies ( $\omega_1 > \omega_{10}$ ) will phase match at larger  $\phi$ . For  $b_0 < 0$ , lower frequencies ( $\omega_1 < \omega_{10}$ ) will phase-match off the collinear axis and there is a maximum angle at which phase-matched frequencies can be found. Physically, this maximum angle is the one at which  $\omega_1 = \omega_2 = \omega_3/2$  (degeneracy) since  $\omega_3/2$  is the lowest possible signal frequency. This will be the case as long as the following

equation has a solution:

$$\cos\phi_m = \frac{n_3(\omega_3)}{n_1(\omega_3/2)} \quad (3.15)$$

Equation (3.15) is plotted as a function of crystal temperature in Fig. 3-3 for a  $1.064\mu$  pump wavelength in  $\text{LiNbO}_3$  ( $b_o < 0$ ) and for two different phase-matching angles,  $\theta_m$ .\*

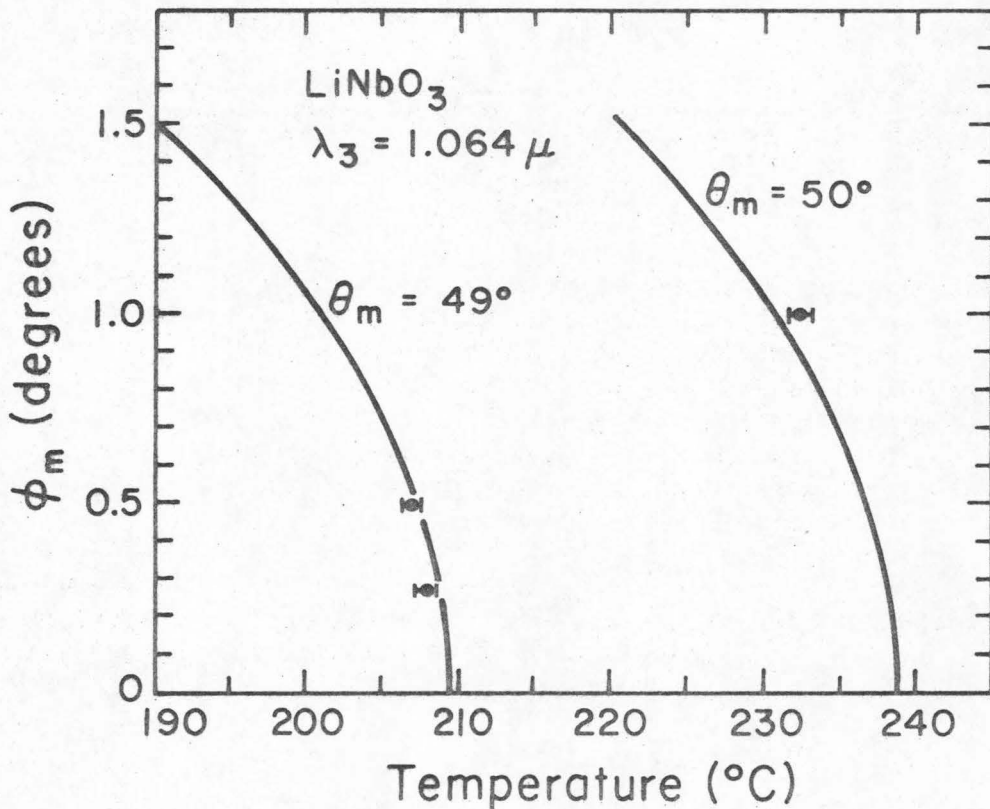


Figure 3-3. Maximum angle  $\phi_m$  at which the degenerate wavelength  $\lambda_1 = 2\lambda_3$  is found as a function of temperature and for two values of the phase-matching angle,  $\theta_m$ . The crystal is  $\text{LiNbO}_3$  and the pump wavelength is  $1.064\mu$ . The theoretical curves are found from the index data of Ref. 17. The experimental points correspond to the temperatures at which the total fluorescence power peaks for a detector acceptance angle  $\theta = \phi_m$ .

\*The angle between the pump direction  $\vec{k}_3$  and the crystal optic axis is called the phase-matching angle (see Appendix I).

The three experimental points were obtained from measurements of total fluorescence power using a procedure to be described in the next section.

### C. Fluorescence Power

The total fluorescence power within a given detector acceptance angle is found by integrating Eq. (3.8) over all frequencies and angles. The result is

$$P_1 = \ell^2 P_3 \int_{-\infty}^{\infty} \int_0^{\theta} K \operatorname{sinc}^2(\Delta k \ell / 2) \phi \, d\phi d\omega. \quad (3.16)$$

If the frequencies within the angle  $\theta$  are far from degeneracy,\* then  $b_1 \omega \ll b_0$ . Equation (3.11) can then be used in Eq. (3.16) to find [3]

$$P_1 = \frac{K \ell P_3}{|b_0|} \pi \theta^2. \quad (3.17)$$

In evaluating the integral in Eq. (3.16),  $K$  has been assumed constant over the small range of frequencies which contribute to the integral. This will be a valid approximation as long as  $\theta$  is not too large. From Eq. (3.16) it is apparent that the total signal fluorescence power varies linearly with crystal length and pump power [6] and will increase as degeneracy is approached ( $b_0 = 0$  at degeneracy).

It is interesting to investigate the increase of the fluorescence power as the collinear phase-matched frequencies are tuned toward degeneracy. Tuning is accomplished by changing the refractive indices

---

\* Degeneracy occurs when  $\omega_1 = \omega_2 = \omega_3/2$ .

at each frequency by varying the phase-matching angle or the crystal temperature. The frequencies which satisfy  $\Delta k = 0$  are thus changed. Clearly the signal power will not increase without bound as the degenerate condition is approached, but rather will reach some maximum and then begin to decrease. The maximum total power will occur near, but not exactly at, collinear degeneracy. Figure 3-4 shows several theoretical power versus temperature curves for a  $1.064\mu$  pump in  $\text{LiNbO}_3$ . The ordinate axis in the figure is the total signal plus idler power per unit pump power. The curves in Fig. 3-4 were computed by numerical integration using Eqs. (3.11) and (3.16) and the refractive index data of Ref. 17.

In one report on total emitted fluorescence [18] the authors implied that the peak power occurred at collinear degeneracy. As shown in Fig. 3-4, the peak is a function of the maximum detector acceptance angle, and the collinear wavelength at the peak of the power can differ considerably from degeneracy.

To get a qualitative picture of how the total fluorescence power peaks, consider Fig. 3-5 where Eq. (3.11) is used to plot  $\phi^2$  versus  $\omega$  for  $\Delta k = 0$ . Only the solid portion of the curves in Fig. 3-5 has physical meaning. The double-valued behavior of  $\omega(\phi^2)$  as found from Eq. (3.11) results from truncating the Taylor series expansions of  $k_j(\omega)$ . For the case of  $b_1 < 0$  (Fig. 3-5a), there is a maximum angle (Eq. (3.15)) for which phase-matched frequencies can be found. The phase-matched frequencies are emitted in a cone about the collinear axis with half-angle  $\phi_m$ . As collinear degeneracy is approached (by

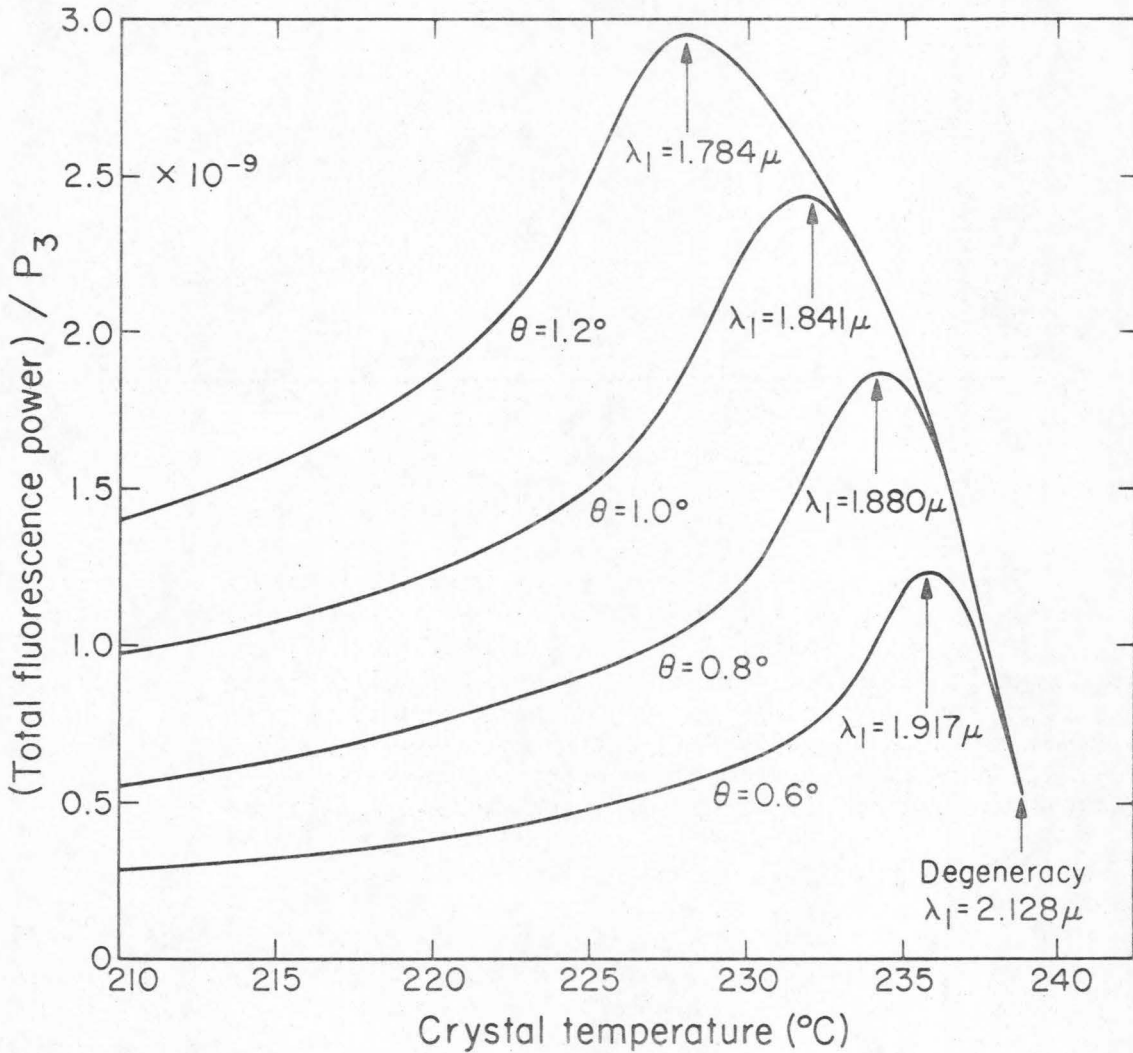


Figure 3-4. Theoretical total fluorescence power as a function of temperature in  $\text{LiNbO}_3$  for  $\lambda_3 = 1.064 \mu$  and a phase-matching angle  $\theta_m = 50^{\circ}$ . The ordinate axis is the signal + idler fluorescence power per unit pump power in watts. Each curve corresponds to a different detector acceptance angle measured internal to the nonlinear crystal. The vertical arrows indicate the collinear signal wavelength at the temperature giving maximum power.

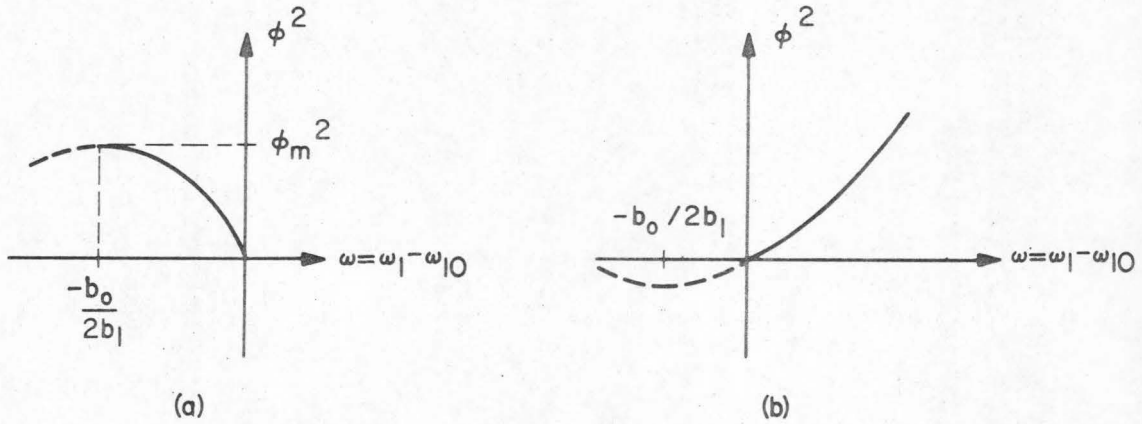


Figure 3-5. Qualitative plot of  $\phi^2$  as defined by Fig. 3-2 and Eq. (3.11) as a function of frequency. The curves are drawn for  $\Delta k = 0$  and (a)  $b_0, b_1 < 0$ ;  $b_0, b_1 > 0$ . Only the solid portion of the curves has physical meaning (see text).

increasing the crystal temperature, for example),  $\phi_m$  decreases and eventually becomes smaller than the acceptance angle  $\theta$ . From this point, the total phase-matched bandwidth within  $\theta$  decreases. Since the power per unit bandwidth is approximately constant (see Section D below), the total measured power thus begins to decrease. The curves in Fig. 3-4 illustrate this behavior since the peak of the curves occur at lower temperatures (farther from collinear degeneracy) for larger values of  $\theta$ .

The case of  $b_1 > 0$  is illustrated in Fig. 3-5b. The degenerate frequency does not phase-match at any angle if there is a non-degenerate phase-matched collinear frequency. For this case in  $\text{LiNbO}_3$ , collinear degeneracy can be approached by decreasing the crystal temperature.

As the temperature is lowered below the degenerate temperature, there are no frequencies which phase-match collinearly. The "cone" of fluorescence then develops a dark center and the degenerate frequency is found at some  $\phi_{\min} > 0$ . As before, the total bandwidth and the total fluorescence power in a given  $\theta$  then decrease.

An experimental arrangement for measuring the total emitted fluorescence power is shown in Fig. 3-6. The pump is a  $1.064\mu$  tungsten-pumped Nd:YAG laser, Q-switched by a rotating mirror. Two  $\text{LiNbO}_3$  nonlinear crystals purchased from different manufacturers were used; one was cut for a phase-matching angle of  $50^\circ$  and for the other,  $\theta_m = 49^\circ$ . The crystal used was held in a temperature-controlled oven

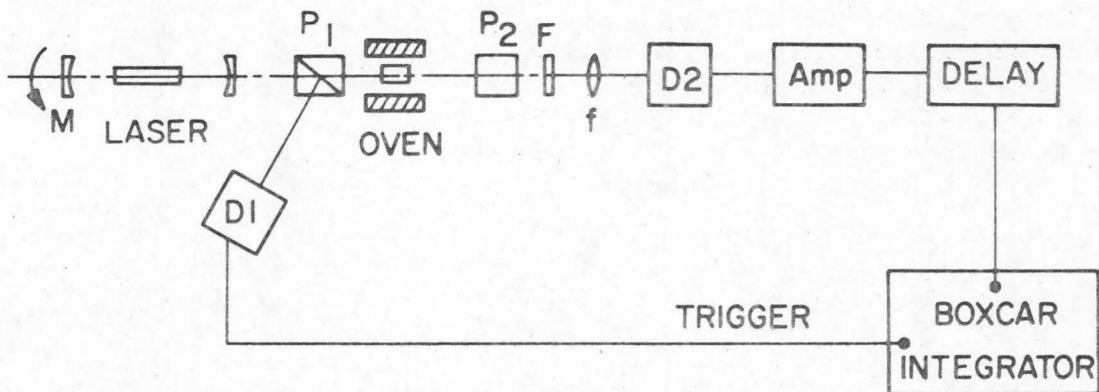


Figure 3-6. Schematic of experimental arrangement for measuring total emitted fluorescence power. Pump laser:  $1.064\mu$  repetitively Q-switched Nd:YAG. M: rotating mirror Q-switch (400 Hz). P1,P2: crossed polarizers. F:  $1.06\mu$  reject,  $1.3\mu$  to  $3.0\mu$  pass filters. D1,D2: high-speed detectors. F: short focal length lens. The  $\text{LiNbO}_3$  crystal is held in the temperature-controlled oven.

so that its temperature could be continuously varied. The temperature stability of the oven was better than  $0.1^{\circ}\text{C}$  over the length of the nonlinear crystal and the oven calibration accuracy was  $\pm 0.2^{\circ}\text{C}$ .

The results of the experimental fluorescence measurements are shown in Figs. 3-7 and 3-8 along with theoretical curves calculated using the index data of Hobden and Warner [17]. The solid curves were computed using Eqs. (3.11) and (3.16) and the dashed curves found from the approximate expression, Eq. (3.17). The experimental points and the solid curves are each normalized to their respective maximum; the dashed curve is normalized to the maximum of the solid curve in each case. Note that far from the maximum the two curves are nearly identical. The theoretical peak power in Fig. 3-7 corresponds to  $5.8 \times 10^{-6}$  watts of in-crystal total fluorescence power for the experimental 2 KW peak pump power.

Since the indices of refraction in  $\text{LiNbO}_3$  are known to vary with composition [19-21], the theoretical curves must be corrected to account for the difference between the crystal compositions used here and that in Ref. 17. Both crystals used in these experiments were grown from a congruent melt [21]; the crystal used by Hobden and Warner [17] had a stoichiometric composition. The Sellmeir equations given by Hobden and Warner show that the strongest temperature variation of the indices occurs in the extraordinary index  $n_e$  and is nearly independent of wavelength (the Sellmeir equation constants vary slowly with temperature so  $d(\text{dn}/dT)/d\lambda \approx 0$ ). In addition, Bergman, et al [20] have shown that only  $n_e$  is affected by crystal composition. One possible conclusion of these observations is that only the wavelength-independent

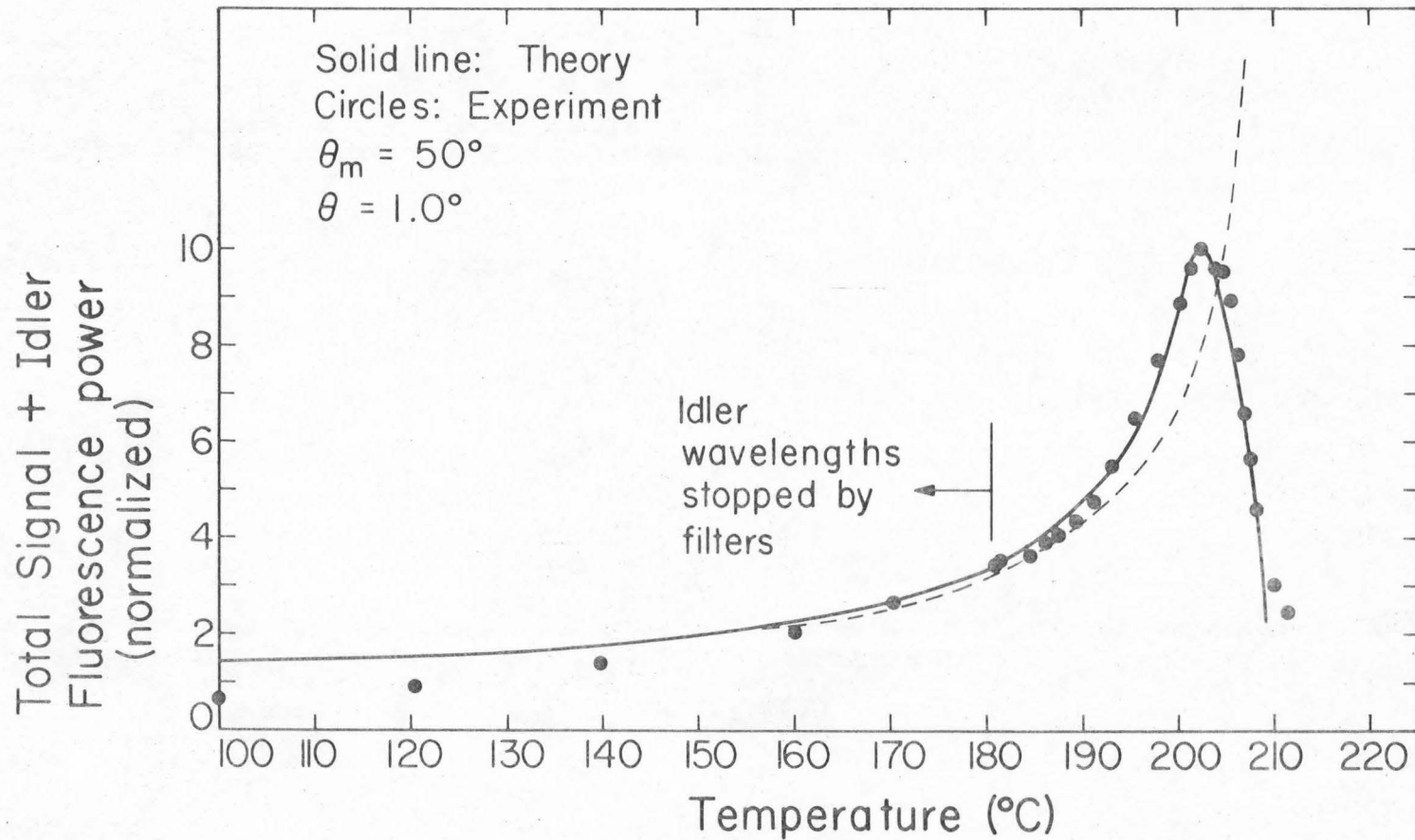


Figure 3-7. Total parametric fluorescence power in  $\text{LiNbO}_3$  for  $\lambda_3 = 1.064\mu$ ,  $\theta_m = 50^\circ$ , and  $\theta = 1.0^\circ$ . Solid curve: exact theory (Eq. (3.16)); dashed curve: approximate theory (Eq. (3.17)). The theoretical curves have been shifted by  $-29.5^\circ\text{C}$  to align the theoretical and experimental peaks. For temperatures below that indicated, only the signal power is included in the theoretical curve because of the reduced transmission of the filters used in the experiment.

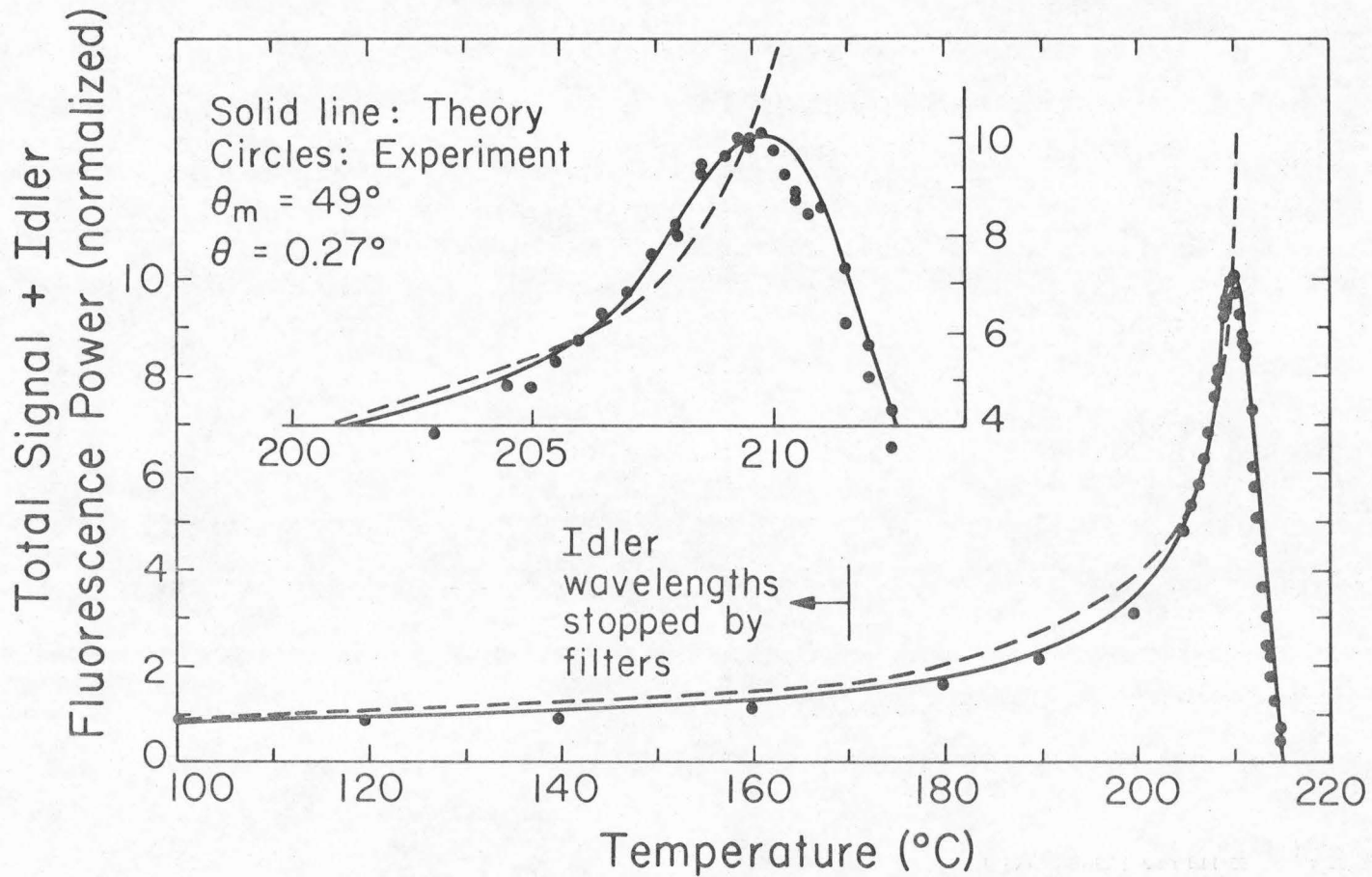


Figure 3-8. Total parametric fluorescence power in  $\text{LiNbO}_3$  for  $\lambda_3 = 1.064\mu$ ,  $\theta_m = 49^\circ$ , and  $\theta = 0.27^\circ$ . Solid curve: exact theory (Eq. (3.16)); dashed curve: approximate theory (Eq. (3.17)). The theoretical curves have been shifted by  $+1.9^\circ\text{C}$  to align the theoretical and experimental peaks. For temperatures below that indicated, only the signal power is included in the theoretical curve because of the reduced transmission of the filters used in the experiment.

temperature variation of the extraordinary index is affected by crystal composition.

In the type of phase-matching used here (ordinary signal and idler, extraordinary pump), only the index of refraction seen by the pump field will be affected by different crystal compositions. The result for congruent crystals will be to increase  $n_e(\lambda_3)$  [20] and decrease the phase-matching temperature for a given parametric process [19-21] from those for a stoichiometric crystal. To first order, the shape of the phase-matched wavelength versus temperature curve will not be affected by crystal composition, but its location relative to the temperature axis will change.

The theoretical curves in Figs. 3-7 and 3-8 have thus been shifted along the temperature axis to align the theoretical and experimental peaks. The two different crystals had significantly different phase-matching characteristics as indicated by the different temperature shift. In Fig. 3-7 the theoretical curve is shifted by  $-29.5^\circ\text{C}$  ( $T_{\text{peak}}(\text{expt.}) - T_{\text{peak}}(\text{theory})$ ). In Fig. 3-8, however, the shift is  $+1.9^\circ\text{C}$ . The close agreement of the theoretical curves and the experimental points over a wide temperature range and for two different crystals and phase-matching angles gives support to the assumption that the shape of the wavelength versus temperature curve is nearly unchanged by variations in crystal composition; only the temperature at which certain frequencies phase-match is altered.

D. Bandwidth

The exact spectral bandwidth of the fluorescence incident on a detector is found by integrating Eq. (3.8) over the detector acceptance angle  $\theta$ . The result is

$$\frac{dP_1(\theta, \omega)}{d\omega_1} = \frac{K\ell P_3}{G} \left[ S\left(\frac{G\ell\theta^2}{2} - \beta\right) + S(\beta) \right] \quad (3.18)$$

where  $\beta = (b_0\omega + b_1\omega^2)\ell/2$  and

$$S(x) = \int_0^x \text{sinc}^2 u du = \frac{-\sin^2 x}{x} + \int_0^x \frac{\sin u}{u} du \quad (3.19)$$

The fluorescence bandwidth can now be defined as the full-width at half-maximum of the power per unit frequency,  $dP_1/d\omega_1$ . An approximation to this exact bandwidth can be found by defining the bandwidth as the full-width at half-maximum of the  $\text{sinc}^2(\Delta k\ell/2)$  curve. Equation (3.11) then gives

$$\Delta\omega_1 = \frac{1}{2|b_1|} \left| \left( b_0^2 + 4b_1G\theta^2 + \frac{3.54\pi b_1}{\ell} \right)^{\frac{1}{2}} - \left( b_0^2 - \frac{3.54\pi b_1}{\ell} \right)^{\frac{1}{2}} \right| \quad (3.20)$$

For small enough values of  $\theta$  and for frequencies far from collinear degeneracy so that  $b_1\omega \ll b_0$ , the approximate bandwidth reduces to

$$\Delta\omega_1 = \frac{1.77\pi}{\ell|b_0|} + \frac{G\theta^2}{|b_0|} \quad (3.21)$$

Notice that as  $\theta \rightarrow 0$ , the bandwidth approaches a minimum value. This is true because even in the collinear direction there are output frequencies corresponding to  $|\Delta k\ell/2| \lesssim \pi$ . Equation (3.21) also requires that for  $\theta^2 \gtrsim 1.77\pi/G\ell$ , the bandwidth will vary as the square of

the acceptance angle.

Equations (3.17) and (3.21) can be combined to give an interesting result. Dividing Eq. (3.17) by (3.21) gives the power per unit bandwidth as

$$\frac{P_1}{\Delta\omega_1} = \frac{\pi K \ell P_3}{G} \left( \frac{\theta^2}{\frac{1.77\pi}{G\ell} + \theta^2} \right) \quad (3.22)$$

For large angles such that  $\theta^2 \gg 1.77\pi/G\ell$ , Eq. (3.22) shows that the power per unit bandwidth becomes constant, independent of  $\theta$  and for small angles will vary as  $\theta^2$ . This behavior is also present in Eq. (3.18), of course, but is not readily apparent. The maximum power per unit bandwidth can be found from Eq. (3.18), however. The result is

$$\left( \frac{dP_1}{d\omega_1} \right)_{\max} = \frac{2K\ell P_3}{G} S(G\ell\theta^2/4) \quad (3.24)$$

#### E. Experimental Measurements

Measurements of narrow bandwidth parametric fluorescence have previously been made only in the visible or near-visible spectral regions where photomultipliers can be used as detectors. This limitation has occurred because the fluorescence power is very small ( $10^{-11}$  watts/( $P_3$ -cm $^{-1}$ ) in the visible) and because available detectors are relatively insensitive for wavelengths longer than  $1\mu$ . An experimental arrangement which overcomes those difficulties is shown in Fig. 3-9. The laser is the same one used in the previous total power measurements, but here it is operated cw. The nonlinear crystal is anti-reflection

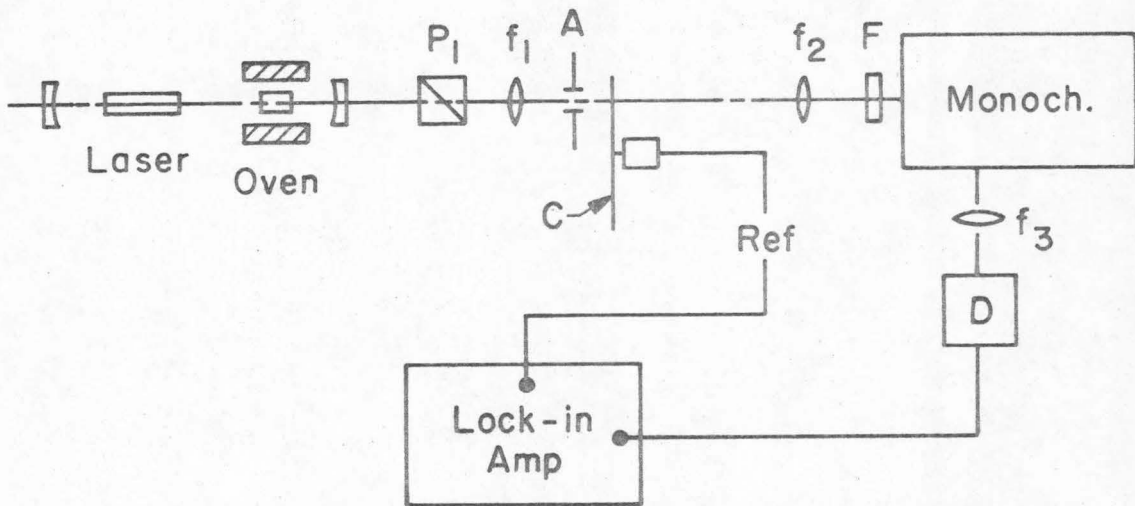


Figure 3-9. Schematic of experimental arrangement for measuring IR narrow-bandwidth parametric fluorescence. Pump laser: cw Nd:YAG.  $P_1$ : polarizer.  $f_1, f_2$ : collecting and matching telescope. A: limiting aperture. C: chopper. F: visible and pump filters.  $f_3$ : short focal length lens. D: PbS photoconductive detector.

coated and placed inside the laser cavity to take advantage of the large optical powers available inside the cavity.

There were two main reasons for operating the laser cw instead of Q-switched. First, the PbS photoconductive detector, lock-in combination provides approximately four times the signal-to-noise as the best available high-speed detector amplifier combination used with a boxcar integrator. Second, the high power densities inside the laser during Q-switched operation quickly damage the coatings on the nonlinear crystal. The one drawback of cw operation is that the high laser power ( $\approx 40$  watts in the experiment) heated the crystal and thus shifted the tuning curve of the observed fluorescence from that expected from the oven temperature readings.

The results of several monochromator scans are shown in Fig. 3-10 along with theoretical curves computed by integrating Eq. (3.18) over the  $20\text{\AA}$  bandwidth of the monochromator at each center wavelength. Because there was no way to accurately calibrate the detection system at  $1.62\mu$ , the experimental data are normalized to the peak of the theoretical curve for each value of  $\theta$ . The vertical line at  $\lambda = 1.6278\mu$  corresponds to the theoretical collinear phase-matched wavelength. Note that the peak of the fluorescence versus wavelength curve is farther from the collinear wavelength for larger angles.

The theoretical curves are computed using the data of Ref. 17 and a crystal temperature of  $173.5^\circ\text{C}$ . In the experiment, however, the crystal oven was set at  $170.2^\circ\text{C}$  for all measurements. The crystal used corresponds to the fluorescence data of Fig. 3-8 so that the expected theoretical temperature was  $170.2 - 1.9 = 168.3^\circ\text{C}$ . The shift of the crystal temperature due to heating by the laser is thus approximately  $5.2^\circ\text{C}$ . As can be seen from Fig. 3-10, the agreement between experiment and theory is good even though the theory was derived from a plane-wave analysis and the experiment used a finite (but weakly diverging) beam.

One of the qualitative features of the theoretical analysis is also evident from Fig. 3-10. The peak power reaches a maximum for  $\theta \approx 0.7^\circ$  and is nearly constant for larger angles. For a 40 watt pump (the approximate  $1.06\mu$  power inside the laser), this peak corresponds to an in-crystal fluorescence power of  $6.0 \times 10^{-10}$  watts. The approximate transmission of the optical system at  $1.6\mu$  is 10% so that the expected detector voltage signal is  $42 \mu\text{v}$ . This is to be compared

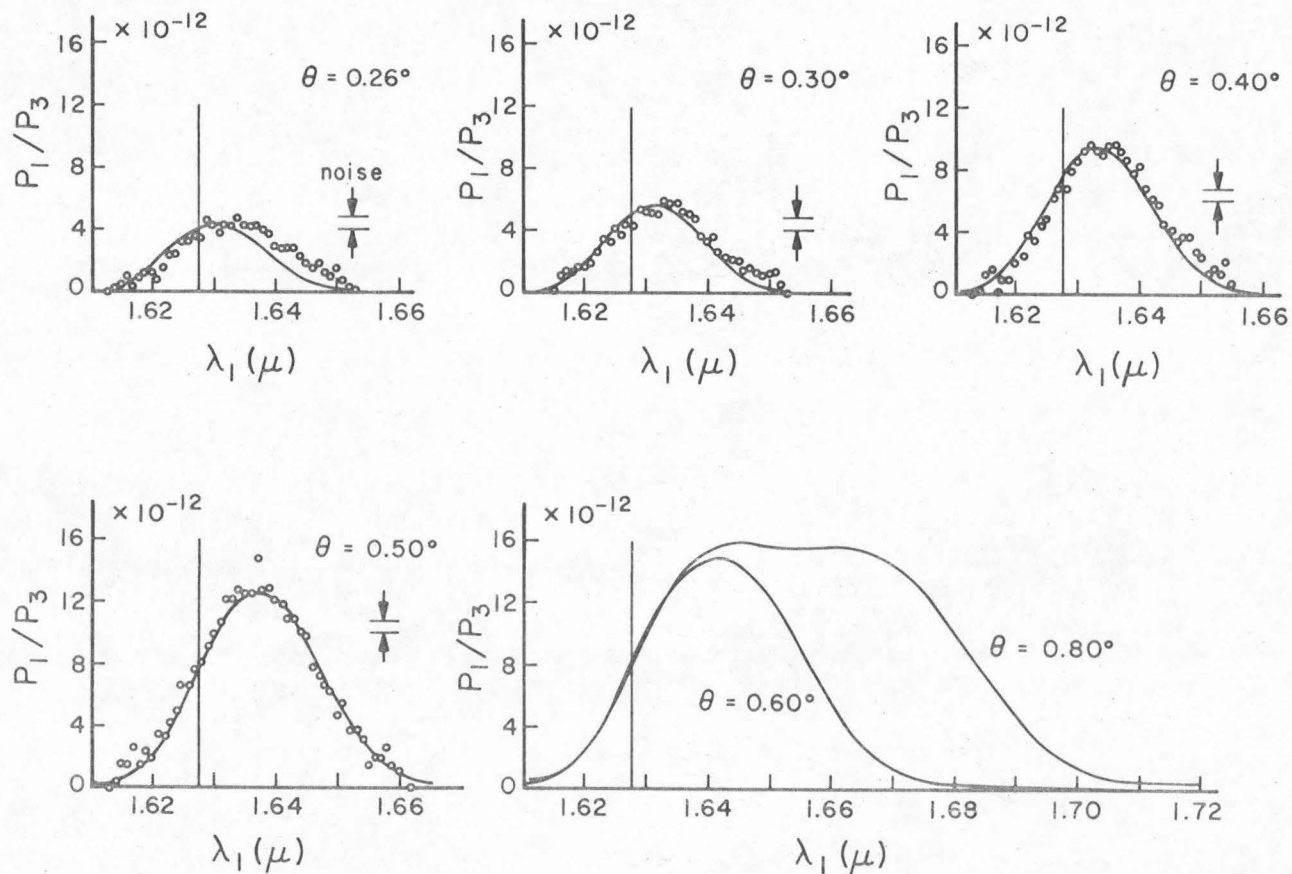


Figure 3-10. Signal fluorescence power as a function of wavelength for various detector acceptance angles. The solid curves are theoretical with the temperature chosen to align the peak of the  $\theta = 0.4^\circ$  curve with the experimental peak (see text). The experimental data are normalized to the peak of each theoretical curve. The monochromator bandwidth is  $20\text{\AA}$  and the experimental uncertainty is indicated in each figure. The vertical line at  $\lambda_1 = 1.6278\mu$  is the collinear signal wavelength.

to the observed value of 25  $\mu\text{v}$ . The discrepancy can be attributed in part to the nonuniform heating of the crystal by the laser pump beam. Since the laser has some transverse profile (roughly Gaussian), the amount of heating will vary across the beam so that different parts of the crystal are at different temperatures. A temperature profile will cause nonuniform phase-matching so the entire pump power will not be effective in generating fluorescence at a particular frequency.

By integrating the area under the power versus wavelength curves, the total emitted signal power in a given solid angle can be found. The results are shown in Fig. 3-11. The solid theoretical curve was computed using Eq. (3.16) and a numerical integration and the dashed line is found from Eq. (3.17). The experimental points are normalized to the theoretical value at  $\theta^2 = 0.16$ .

The fluorescence bandwidth and peak power can be found from measurements such as those shown in Fig. 3-10. The results are shown in Figs. 3-12 and 3-13 as a function of the square of the acceptance angle. The bandwidth values are taken directly from the experimental data, but the peak power data are normalized to the theoretical value at  $\theta^2 = 0.28$ . The agreement with theory is seen to be good within the experimental error. The figures exhibit again the qualitative predictions of the theory: for small  $\theta$ , a minimum bandwidth and a peak power varying as  $\theta^2$ ; for large angles, there is a maximum peak power and the bandwidth varies as  $\theta^2$ . The solid theoretical lines in the figures are computed using Eq. (3.18); the dashed line in Fig. 3-12 is found from Eq. (3.21) and that in Fig. 3-13 from Eq. (3.22).

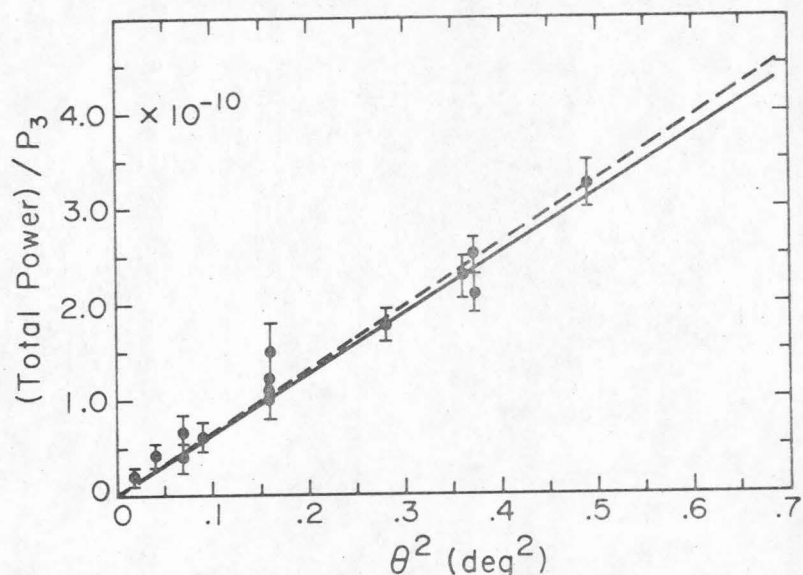


Figure 3-11. Total signal power versus detector acceptance angle. The solid line is the theoretical in-crystal fluorescence power per unit pump power calculated using Eq. (3.17). The dashed line is found using the approximate expression, Eq. (3.15). The experimental data are normalized to the solid theoretical curve at  $\theta^2 = 0.16 \text{ deg}^2$ .

The tuning curve of the  $1.064\mu$  -pumped fluorescence is shown in Fig. 3-14. To compare the experimental data with theory, two corrections must be made. First, the tuning data were taken with an acceptance angle of  $\theta = 0.4^\circ$ . The peak of the monochromator scans will thus be shifted from the actual collinear wavelengths by an amount which depends on the temperature. The experimental wavelengths are corrected for this shift using the data of Ref. 17. Second, the heating of the crystal must be taken into account and related to the crystal oven temperature settings. To do this, the theoretical curve is shifted by  $+1.9^\circ\text{C}$  from the results found using Ref. 17 (result of total power measurement, Fig. 3-8) and the oven readings are increased by  $5.2^\circ\text{C}$ . With these corrections the theoretical tuning curve agrees nicely with the experimental data.

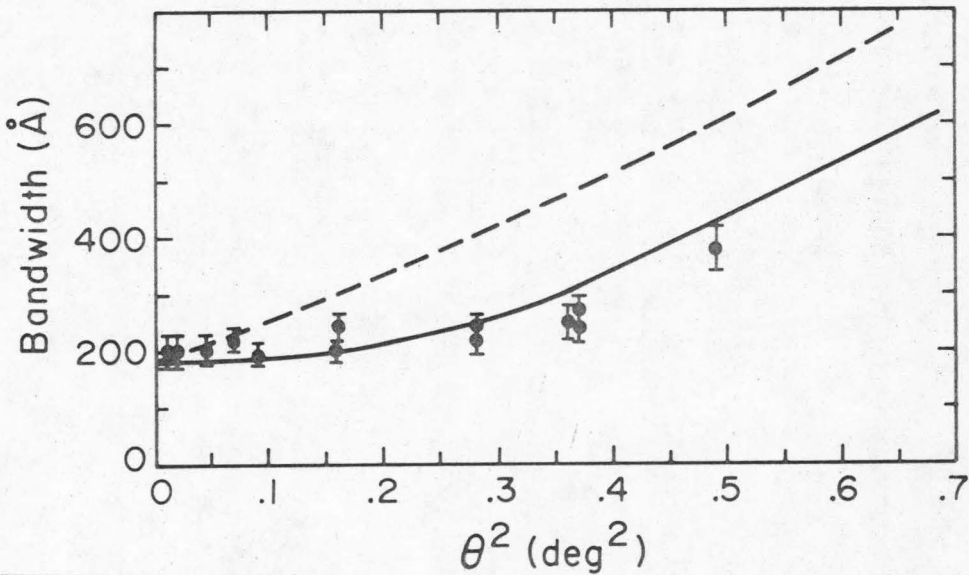


Figure 3-12. Signal fluorescence bandwidth as a function of detector acceptance angle. The solid line is the exact theoretical bandwidth; the dashed curve is found from Eq. (3.21).

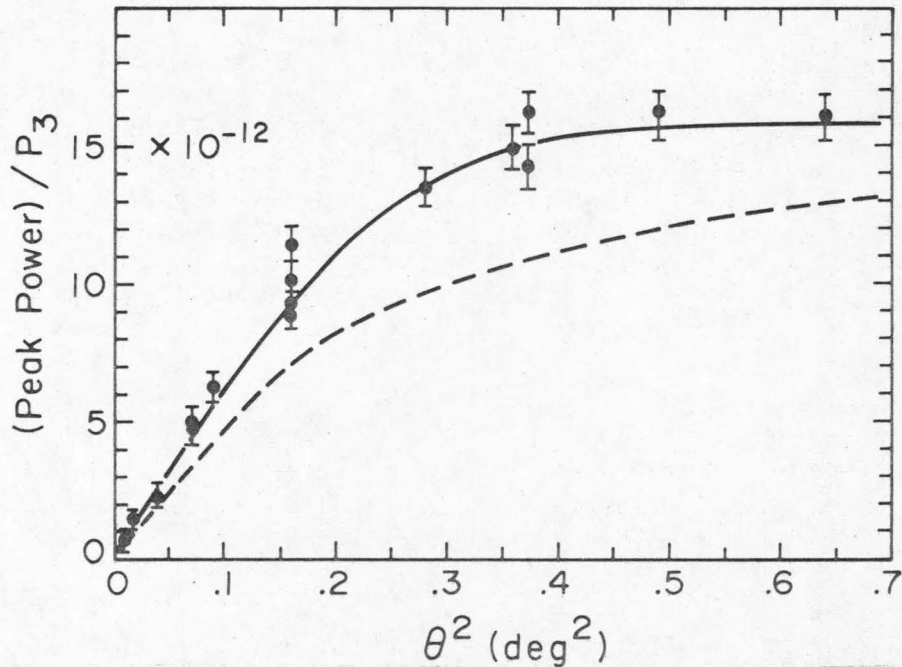


Figure 3-13. Peak fluorescence power in a 20Å bandwidth as a function of detector acceptance angle. The ordinate axis is the theoretical in-crystal fluorescence power per unit pump power. The experimental data are normalized to the theoretical curve at  $\theta^2 = 0.28 \text{ deg}^2$ . Solid curve: exact theory (Eq. 3.18)). Dashed curve: approximate theory (Eq. 3.22)).

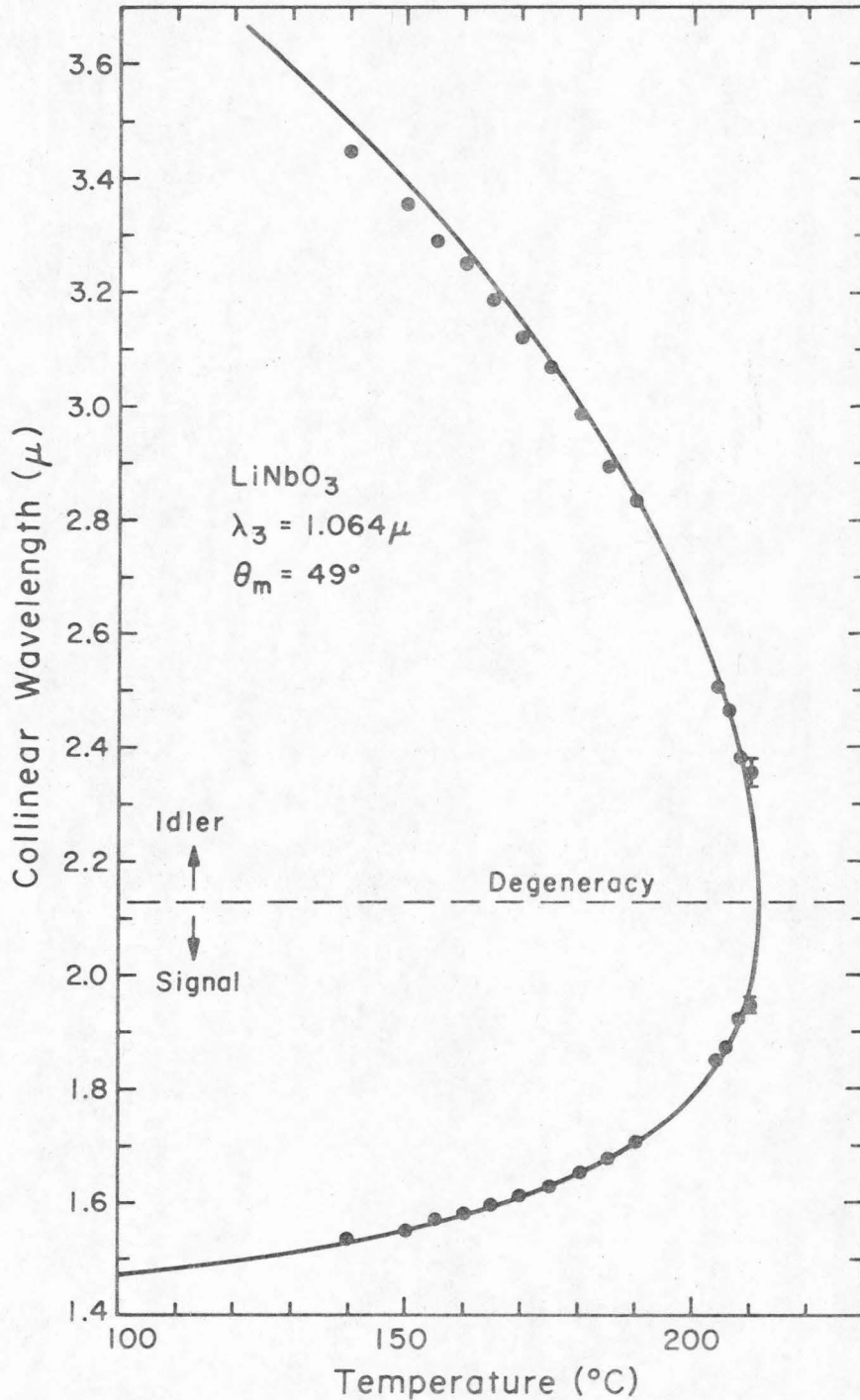


Figure 3-14. Temperature tuning curve for 1.064 $\mu$ -pumped parametric fluorescence in LiNbO<sub>3</sub>. The solid theoretical curve has been shifted by +1.9°C and the experimental data points are corrected for finite detector acceptance angle and crystal heating (see text).

Finally, the theoretical minimum bandwidth calculated from Eq. (3.20) with  $\theta = 0$  is shown in Fig. 3-15 along with several experimental points. The experimental values were found by measuring the bandwidth with  $\theta = 0.4^\circ$  and correcting the results by a temperature dependent factor to give the bandwidth for  $\theta = 0$ . The data have also been corrected for crystal heating and the theoretical curve shifted by  $+ 1.9^\circ\text{C}$  as explained above. The bandwidth is nearly linear with temperature (and signal wavelength) far from degeneracy and rapidly increases as collinear degeneracy is approached.

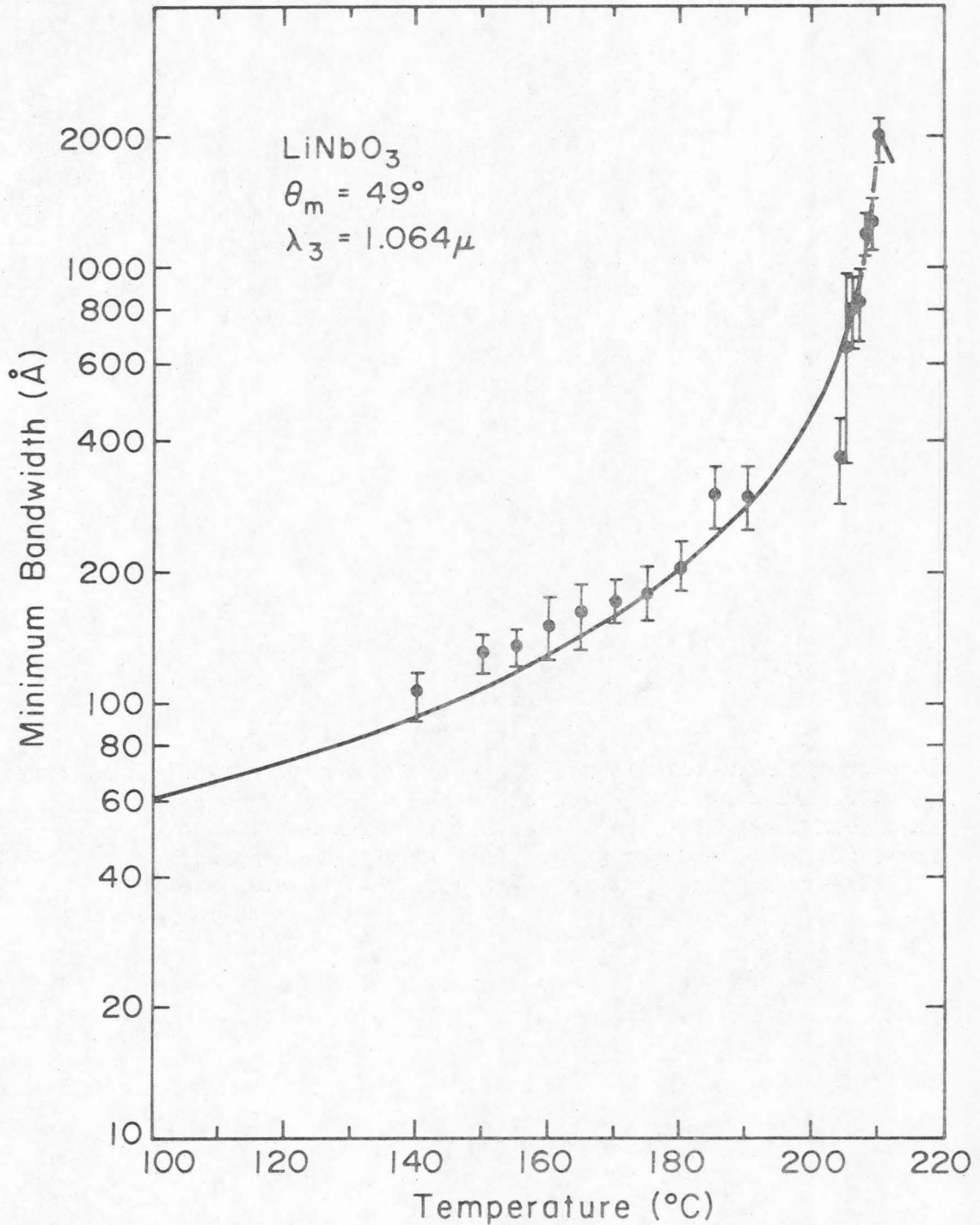


Figure 3-15. Minimum bandwidth (collinear bandwidth) as a function of temperature in LiNbO<sub>3</sub>. The pump wavelength is 1.064 $\mu$  and the phase-matching angle is 49°. The data have been corrected for finite detector acceptance angle and crystal heating and the theoretical curve is shifted by +1.9°C (see text).

Chapter 3

References

1. W. H. Louisell, A. Yariv, and A. E. Siegman, "Quantum Fluctuations and Noise in Parametric Processes, I," Phys. Rev., Vol. 124, pp. 1646-1654 (1961).
2. T. G. Giallorenzi and C. L. Tang, "Quantum Theory of Spontaneous Parametric Scattering of Intense Light," Phys. Rev., Vol. 166, pp. 225-233 (1968).
3. R. L. Byer and S. E. Harris, "Power and Bandwidth of Spontaneous Parametric Emission," Phys. Rev., Vol. 168, pp. 1064-1068 (1968).
4. D. A. Kleinman, "Theory of Optical Parametric Noise," Phys. Rev., Vol. 174, pp. 1027-1041 (1968).
5. S. E. Harris, M. K. Oshman, and R. L. Byer, "Observation of Tunable Optical Parametric Fluorescence," Phys. Rev. Lett., Vol. 18, pp. 732-734 (1967).
6. D. Magde and H. Mahr, "Study in Ammonium Dihydrogen Phosphate of Spontaneous Parametric Interaction Tunable from 4400 to 16000Å," Phys. Rev. Lett., Vol. 18, pp. 905-907 (1967).
7. S. A. Akhmanov, V. V. Fadeev, R. V. Khokhlov, and O. N. Chuneav, "Quantum Noise in Parametric Light Amplifiers," JETP Lett., Vol. 4, pp. 575-578 (1967) (translation, pp. 85-87).
8. D. Magde, R. Scarlet, and H. Mahr, "Noncollinear Parametric Scattering of Visible Light," Appl. Phys. Lett., Vol. 11, pp. 381-383 (1967).

9. R. G. Smith, J. G. Skinner, J. E. Geusic, and W. G. Nilsen, "Observations of Noncollinear Phase Matching in Optical Parametric Noise Emission," *Appl. Phys. Lett.*, Vol. 12, pp. 97-100 (1968).
10. T. G. Giallorenzi and C. L. Tang, "CW Parametric Scattering in ADP with Strong Absorption in the Idler Band," *Appl. Phys. Lett.*, Vol. 12, pp. 376-378 (1968).
11. M. W. Dowley, "Parametric Fluorescence in ADP and KDP Excited by a 2573Å CW Pump," unpublished.
12. J. S. Kruger and T. J. Gleason, "Parametric Fluorescence in  $Ba_2Na Nb_5O_{15}$  for 10 CW Pump Wavelengths," *J. Appl. Phys.*, Vol. 41, pp. 3903-3904 (1970).
13. C. Laurence and F. Tittel, "Prediction of the Tuning Characteristics of an Optical Parametric Oscillator Using Parametric Fluorescence," *Opto-Elect.*, Vol. 3 pp. 1-4 (1971).
14. A. Hordvik, H. R. Schlossberg, and C. M. Stickley, "Spontaneous Parametric Scattering of Light in Proustite," *Appl. Phys. Lett.*, Vol. 18, pp. 448-450 (1971).
15. J. E. Pearson, U. Ganiel, and A. Yariv, "Parametric Oscillator Tuning Curve from Observations of Total Parametric Fluorescence," *IEEE J. Quant. Electron.* QE-8, pp. 383-385 (1972).
16. R. L. Byer, "Parametric Fluorescence and Optical Parametric Oscillation," Ph.D. Thesis (Available as M.L. Report No. 1711), Stanford University, 1968.
17. M. V. Hobden and J. Warner, "The Temperature Dependence of the Refractive Indices of Pure Lithium Niobate," *Phys. Lett.*, Vol. 22, pp. 243-244 (1966).

18. E. O. Ammann and J. M. Yarborough, "Optical Parametric Oscillation in Proustite," Appl. Phys. Lett., Vol. 17, pp. 233-235 (1970).
19. J. E. Midwinter, "Lithium Niobate: Effects of Composition on the Refractive Indices and Optical Second-Harmonic Generation," J. Appl. Phys., Vol. 39, pp. 3033-3038 (1968).
20. J. G. Bergman, A. Ashkin, A. A. Ballman, J. M. Dziedzic, H. J. Levinstein, and R. G. Smith, "Curie Temperature, Birefringence, and Phase-matching Temperature Variations in  $\text{LiNbO}_3$  as a Function of Melt Stoichiometry," Appl. Phys. Lett. 12, pp. 92-94 (1968).
21. R. L. Byer, J. F. Young, and R. S. Feigelson, "Growth of High-Quality  $\text{LiNbO}_3$  Crystals from the Congruent Melt," J. Appl. Phys., Vol. 41, pp. 2320-2325 (1970).

CHAPTER 4

PARAMETRIC OSCILLATOR: THEORY

A. Introduction

This chapter discusses theoretically some of the important parameters of parametric oscillators. The most general case of a pulsed parametric oscillator where all the fields have both time and space dependence has not yet been treated in detail. The complexity of solving simultaneously the six nonlinear, coupled, partial differential equations describing the oscillator is immense. All published treatments to date simplify the problem usually by neglecting either the time or space dependence of all the fields and frequently by assuming one or two fields to be constant in both time and space.

This treatment makes no attempt to solve the general problem. In each case, however, as much generality as possible is retained. The threshold behavior of a parametric oscillator is studied by examining a steady-state parametric amplifier placed inside a Fabry-Perot resonator. Returning to the time-dependent interaction equations, the rise time of an oscillator is discussed in detail. Finally, a few comments are made on the bandwidth and frequency stability of the oscillator output and on the limitations on pump bandwidth.

B. Fabry-Perot Analysis of a Parametric Oscillator

The steady-state behavior of a parametric oscillator is the simplest case to discuss. Consider a generalized Fabry-Perot resonator

filled with a nonlinear medium as shown in Fig. 4-1. There is one

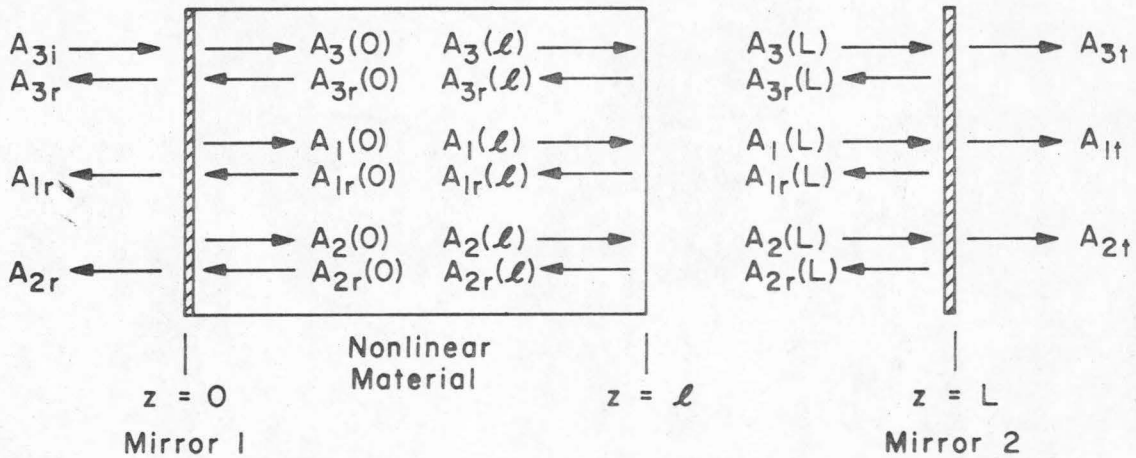


Figure 4-1. Generalized Fabry-Perot resonator partially filled with a nonlinear medium of index  $n_j$  at  $\omega_j$ . The only input field is the pump at  $\omega_3$ . The values of the signal ( $\omega_1$ ), idler ( $\omega_2$ ), and pump fields are indicated at each point in the resonator.

incident field (the pump) at  $\omega_3$ , but reflected and transmitted fields exist at all three frequencies  $\omega_1$ ,  $\omega_2$ , and  $\omega_3$ . Thus there are 18 field quantities inside the resonator. The normalized field amplitudes as defined in Chapter 2 will be used throughout the following discussion.

For the purpose of the present discussion, it is convenient to neglect pump depletion so that the nonlinear interaction has negligible effect on the field at  $\omega_3$ . With this assumption, the pump fields at the input and output of the nonlinear crystal are equal so that

$$A_3(L) = A_{3L} = A_3(0) = A_{30} e^{i\phi_{30}} \quad (4.1)$$

where  $A_{30}$  is a real quantity. This assumption excludes the case of strong interaction and efficient energy conversion from pump to signal

and idler, but is adequate for threshold calculations. Siegman[1] and Bjorkholm [2] have treated the problem of doubly resonant oscillators with strong pump depletion and Kreuzer [3] has analyzed the same problem for the singly-resonant oscillator. Armstrong, et al [4] have found the general solution to the three coupled amplitude equations (Chapter 2, Eqs. (2.2a,b,c)) for the parametric amplifier. The following analysis could be extended to the general case of a depleted-pump by using the results of Ref. 4 in place of Eqs. (4.2) below.

The analysis begins with the steady-state amplifier solutions found in Chap. 2 for the fields at the output of the nonlinear crystal (Eqs. (2.27) and (2.28)):

$$\begin{aligned}
 \text{(a)} \quad A_1(\ell) &= (\alpha A_{10} + \beta^* A_{20}) e^{i(\phi_{10} - k_1 \ell)} \\
 \text{(b)} \quad A_2^*(\ell) &= (\alpha^* A_{20} + \beta A_{10}) e^{-i(\phi_{20} - k_2 \ell)} .
 \end{aligned} \tag{4.2}$$

All the quantities appearing in Eq. (4.2) are as defined in Chap. 2 and the plane-wave phase  $\exp(-ik_j \ell)$  has been put back into the expressions for  $A_j(\ell)$ . For collinear propagation the phase mismatch  $\Delta k$  is given by

$$\begin{aligned}
 \Delta k &= k_3 - k_1 - k_2 = \frac{1}{c} (n_3 \omega_3 - n_1 \omega_1 - n_2 \omega_2) \\
 &= n_3 k_{30} - n_1 k_{10} - n_2 k_{20}
 \end{aligned} \tag{4.3}$$

where  $k_{j0} = \omega_j/c$  is the wave vector in vacuum ( $n = 1$ ) and  $n_j$  is the index of refraction at  $\omega_j$ .

The equations for the field amplitudes at any point in the cavity can be expressed in matrix form by defining the following quantities:

$$\begin{aligned}
 \text{(a)} \quad \tilde{C}_1 &= \begin{pmatrix} \alpha e^{i\phi_{10}} & \beta^* e^{i\phi_{10}} \\ \beta e^{-i\phi_{20}} & \alpha^* e^{-i\phi_{20}} \end{pmatrix} \\
 \text{(b)} \quad \tilde{C}_2 &= \begin{pmatrix} e^{-ik_{10}L'_1} & 0 \\ 0 & e^{ik_{20}L'_2} \end{pmatrix} \\
 \text{(c)} \quad \tilde{A}_L &= \begin{pmatrix} A_1(\ell) \\ A_2^*(\ell) \end{pmatrix} \\
 \text{(d)} \quad \tilde{A}_0 &= \begin{pmatrix} A_{10} \\ A_{20}^* \end{pmatrix} \tag{4.4}
 \end{aligned}$$

where  $L'_j$  is the optical length of the cavity\* at  $\omega_j$  and  $k_{j0} = \omega_j/c$ . With these definitions the fields at mirror 2 can be written as

$$\tilde{A}_L = \tilde{C}_2 \tilde{C}_1 \tilde{A}_0 \tag{4.5}$$

Note that because all losses in the nonlinear crystal have been neglected,  $|\det(\tilde{C}_1)| = |(|\alpha|^2 - |\beta|^2) e^{i(\phi_{10} - \phi_{20})}| = 1$ .

The quantities  $A_{1rL}$  and  $A_{2rL}^*$  are related to  $A_{1L}$  and  $A_{2L}^*$  by the reflectance of mirror 2. It is convenient to assume that both mirror 1 and mirror 2 have zero reflectance at  $\omega_3$ , since this is the usual case (ideally) in practice. The complex field reflection

---

\*

The optical length at  $\omega_j$  is  $L'_j = (n_j - 1)\ell + L$ .

coefficients of mirror  $i$  ( $i = 1, 2$ ) at  $\omega_j$  is given by

$$R_{ij} \equiv r_{ij} e^{i\psi_{ij}} \quad \text{for } j=1, 2 \quad . \quad (4.6)$$

Thus  $r_{12}$  is the reflection amplitude of mirror 1 at  $\omega_2$  and  $\psi_{12}$  is the corresponding phase change upon reflection. Using Eq. (4.6), the matrix describing the reflection at mirror 2 is

$$\tilde{R}_2 = \begin{pmatrix} R_{21} & 0 \\ 0 & R_{22}^* \end{pmatrix} \quad (4.7)$$

Similarly, the effect of mirror 1 is described by  $\tilde{R}_1$  :

$$\tilde{R}_1 = \begin{pmatrix} R_{11} & 0 \\ 0 & R_{12}^* \end{pmatrix} \quad . \quad (4.8)$$

The description of the backward-traveling waves (relative to the input pump direction) depends on whether a backward-traveling pump wave is generated by the backward-traveling phase-matched signal and idler waves. Unless special precautions are taken (using a ring-resonator [5], for example), a backward-traveling pump wave will always be generated when the idler reflectance is non-zero and will reduce the efficiency of the oscillator [2].

As long as the nondepleted-pump approximation is valid, however, there is negligible loss to the fields at  $\omega_1$  and  $\omega_2$  due to backward-wave pump generation. This conclusion remains true as long

as  $A_1(\ell)$  and  $A_2(\ell)$  remain much less than  $A_3$  as is the case near threshold. Within this approximation, a complete round trip in the resonator is represented by

$$\tilde{A}_0 = \tilde{R}_1 \tilde{C}_2 \tilde{R}_2 \tilde{C}_2 \tilde{C}_1 \tilde{A}_0 \quad . \quad (4.9)$$

The self-consistency condition that the resultant field after one round-trip must equal the assumed input field is implicit in Eq. (4.9).

The requirement for nontrivial solutions for  $\tilde{A}_0$  is

$$\det(\tilde{R}_1 \tilde{C}_2 \tilde{R}_2 \tilde{C}_2 \tilde{C}_1 - \tilde{I}) = 0 \quad (4.10)$$

where  $\tilde{I}$  is the identity matrix. Since  $|\alpha|^2 - |\beta|^2 = 1$ , Eq. (4.10) implies that

$$1 + R_{11} R_{21} R_{12}^* R_{22}^* - (\alpha^* R_{12}^* R_{22}^* e^{2ik_{20} L_2'} + \alpha R_{11} R_{21} e^{-2ik_{10} L_1'}) = 0 \quad . \quad (4.11)$$

### C. Oscillation Threshold

The threshold amplitude and phase conditions for oscillation are found from Eq. (4.11) by equating the real and imaginary parts of the equation to zero. Because of the way in which Eq. (4.11) was derived, it also contains the usual Fabry-Perot resonance conditions on frequency and round-trip phase change. There are thus two separate factors which determine the oscillation threshold. The first requirement is that the signal (and idler, if both have feedback) be near a resonant frequency of the passive Fabry-Perot cavity. The frequencies do not have to lie exactly on a resonance, but there will be an increase

in threshold depending on how far off-resonance the particular frequency occurs [6]. The amount of the increase for a given deviation from resonance depends on the loss and the mirror reflectivity at the frequency of interest [7].

The second requirement is that the phase-mismatch  $\Delta k$  be small enough so that the parametric gain can overcome the losses of the cavity. Clearly this condition is not independent of the Fabry-Perot condition; changing  $\omega_1$  and  $\omega_2$  to make  $\Delta k = 0$  may increase the Fabry-Perot losses because arbitrary  $\omega_1$  and  $\omega_2$  will not lie on cavity resonances. This difficulty was first pointed out by Giordmaine and Miller [6]. For high reflectivities at both  $\omega_1$  and  $\omega_2$ , the Fabry-Perot condition is by far the most stringent requirement [6].

At this point it is convenient to define the total phase change at  $\omega_1$  during one cavity round trip as  $\psi_1 = -2k_{10}L'_1 + \psi_{11} + \psi_{21}$ . This is the phase change for the wave at  $\omega_1$  in the absence of any nonlinear interaction. Similarly, the round trip phase change at  $\omega_2$  is  $\psi_2 = -2k_{20}L'_2 + \psi_{12} + \psi_{22}$ . New real amplitude reflection coefficients are defined by

$$\begin{aligned} R_1 &= r_{11} r_{21} \\ R_2 &= r_{12} r_{22} \end{aligned} \quad (4.12)$$

For equal reflectances at both mirrors,  $R_1$  and  $R_2$  are the intensity reflection coefficients of the mirrors at  $\omega_1$  and  $\omega_2$ , respectively.

These definitions allow the real part of Eq. (4.11) to be written as

$$|\alpha| = \frac{1 + R_1 R_2 \cos(\psi_1 - \psi_2)}{R_1 \cos(\psi_1 + \phi) + R_2 \cos(\psi_2 + \phi)} \quad (4.13)$$

and the imaginary part gives

$$|\alpha| = \frac{R_1 R_2 \sin(\psi_1 - \psi_2)}{R_1 \sin(\psi_1 + \phi) - R_2 \sin(\psi_2 + \phi)} \quad (4.14)$$

The quantity  $\phi$  is the phase of the complex number  $\alpha$  and is given by

$$\begin{aligned} \phi &= -\frac{\Delta k \ell}{2} + \tan^{-1} \left( \frac{\Delta k \sinh \gamma \ell}{2\gamma \cosh \gamma \ell} \right) \\ &= -\frac{\Delta k \ell}{2} + \Delta\phi_m - \frac{\pi}{2} \end{aligned} \quad (4.15)$$

where the last relation follows from Eq. (2.34). Note that the initial value of the relative phase  $\Delta\phi$  does not appear in the oscillation conditions (4.13) and (4.14). The threshold for oscillation is thus independent of  $\Delta\phi$  even though the parametric gain is maximum for the particular value given by Eq. (2.34).

Combining Eqs. (4.13) and (4.14) gives a relationship between the phases  $\psi_1$  and  $\psi_2$  at threshold:

$$C = \frac{\sin(\psi_1 + \phi)}{\sin(\psi_2 + \phi)} = \frac{R_2(1 - R_1^2)}{R_1(1 - R_2^2)} \quad (4.16)$$

Note from Eq. (4.16) that for  $R_1 \neq R_2$ , the signal and idler phases will not differ by a multiple of  $2\pi$  even though the round trip phase change for each must be nearly  $2\pi \times (\text{integer})$  so that  $\omega_1$  and  $\omega_2$

are near a Fabry-Perot resonance. Note also that the phase change resulting from imperfect phase-matching ( $\Delta k \neq 0$ ) in the nonlinear interaction is included in the oscillating phase condition (Eq. (4.16)) as well as in the threshold amplitude conditions (Eq. (4.13)).

Using Eqs. (4.13), (4.14), and (4.16), the threshold conditions are summarized in Eqs. (4.17):

$$\left(1 + \frac{g^2}{\gamma^2} \sinh^2 \gamma \ell\right)^{\frac{1}{2}} = \begin{cases} B[C \cos(\psi_2 + \phi) - (1 - C^2 \sin^2(\psi_2 + \phi))^{1/2}], & R_1 \neq R_2 \quad (a) \\ \frac{1 + R^2}{2R \cos(\psi_2 + \phi)}, \quad \psi_1 = \psi_2 + 2m\pi, \quad R_1 = R_2 = R & (b) \\ \frac{1}{R_1}, \quad \psi_1 + \phi = 2m\pi, \quad R_2 = 0 & (c) \end{cases} \quad (4.17)$$

where  $B = R_1(1 - R_2^2)/R_2^2 - R_1^2$  and  $C$  is given by Eq. (4.16). A similar result has been given by Falk [8]. It is also straightforward to show that

$$\tan(\psi_2 + \phi) = \frac{\sin(\psi_0 + 2\Delta k \ell + 2\phi)}{C + \cos(\psi_0 + 2\Delta k \ell + 2\phi)} \quad (4.18)$$

where

$$\begin{aligned} \psi_0 &= -2k_{30}L'_3 + \psi_{12} + \psi_{22} + \psi_{21} + \psi_{11} \\ &= \psi_1 + \psi_2 - 2\Delta k \ell \end{aligned} \quad (4.19)$$

The quantity  $\psi_0$  is the sum of the signal and idler phase changes for one cavity round trip when  $\Delta k = 0$ . Equation (4.19) follows directly from the definitions of  $\psi_1$ ,  $\psi_2$ , and  $\Delta k$  and can be used with Eq.

(4.18) to eliminate  $(\psi_2 + \phi)$  from Eqs. (4.17). The usefulness of the quantity  $\psi_0$  is that it depends only on the mirror phase changes (nearly constant with frequency when the amplitude reflection is constant) and on the properties of the passive cavity at  $\omega_3$ .

Although Eqs. (4.17) and (4.18) are explicitly functions of  $\Delta k$ , they should really be considered as functions of  $\omega_1$  since  $\Delta k = \Delta k(\omega_1)$  (see Eq. (3.11)). Viewed in this manner, the equations give the pump threshold power ( $P_{3T} \propto (g\ell)^2$ ) and the oscillation frequency  $\omega_1$ ; the idler frequency  $\omega_2$  is determined once  $\omega_1$  is known, since  $\omega_2 = \omega_3 - \omega_1$  and  $\omega_3$  is considered fixed. A number of special cases will now be considered.

#### Doubly-Resonant Oscillator (DRO) with $R_1 = R_2 = R$

This case is the most common one encountered experimentally with the DRO. Equations (4.17b) and (4.18) give the threshold condition as

$$\frac{g^2}{\gamma^2} \sinh^2 \gamma \ell = \kappa_{\min} + (\kappa_{\min} + 1) \tan^2 \left( \frac{\psi_0}{2} + \Delta k \ell + \phi \right) \quad (4.20)$$

where

$$\kappa_{\min} = \frac{(1 - R^2)^2}{4R^2} \quad (4.21)$$

and for  $C = 1$ , Eq. (4.18) gives

$$\tan(\psi_2 + \phi) = \tan(\psi_0/2 + \Delta k \ell + \phi) \quad (4.22)$$

Examination of Eq. (4.16) shows that  $\psi_1 = \psi_2 + 2m\pi$  in this case, so whenever  $\psi_1$  is on a passive-cavity resonance,  $\psi_2$  also coincides

with a resonant frequency; any deviation from exact resonance will occur equally in both frequencies. There are two limiting cases of interest: (1)  $\Delta k = 0$ , but  $\psi_1$  and  $\psi_2$  may not coincide with a passive-cavity resonance ( $\psi_0 = \psi_1 + \psi_2 \neq 2m\pi$ ); and (2)  $\psi_1 + \psi_2 = 2m\pi$  ( $\omega_1$  and  $\omega_2$  exactly resonant), but  $\Delta k \neq 0$ .

For all reasonable values of  $R$  ( $R \gtrsim .90$ ), Eq. (4.21) gives  $\kappa_{\min} \ll 1$  so Eq. (4.20) can be written as

$$\frac{g^2}{\gamma^2} \sinh^2 \gamma \ell = \kappa_{\min} \left[ 1 + \frac{\tan^2(\psi_0/2 + \Delta k \ell + \phi)}{\kappa_{\min}} \right] . \quad (4.23)$$

This relation shows that variations in  $\psi_0$  or  $\Delta k \ell$  will have less effect on oscillator threshold for larger values of  $\kappa_{\min}$  (larger minimum threshold)\*. The minimum threshold condition occurs when  $\psi_0 = 2m\pi$  and  $\Delta k = 0$ . Equation (4.23) gives for this case

$$(gl)_{\min}^2 = \kappa_{\min} \quad (4.24)$$

where  $\sinh^2 gl \approx (gl)^2$ .

The threshold for the first limiting case when  $\Delta k = 0$  and  $\psi_0 \neq 2m\pi$  is found from

$$\frac{\sinh^2 gl}{\kappa_{\min}} = 1 + \frac{\tan^2(\psi_0/2)}{\kappa_{\min}} . \quad (4.25)$$

As long as  $\Delta k = 0$ , the oscillator threshold is determined completely by the properties of the passive Fabry-Perot resonator. The threshold

---

\* A similar conclusion is given in Ref. 9 where an entirely different approach to the problem is used.

can thus be expected to vary as the reciprocal of the transmission of the Fabry-Perot etalon when viewed from the outside. From Ref. 7, the inverse transmission of a Fabry-Perot is given by

$$\frac{1}{T} = 1 + \frac{4R}{(1-R)^2} \sin^2(\delta/2) \quad (4.26)$$

where  $\delta$  is the round trip phase change in the resonator. The similarity between Eqs. (4.25) and (4.26) is obvious. The frequency deviation corresponding to a given  $\psi_0$  is

$$\omega_c \equiv \omega_1 - \omega_{10} = \frac{c\psi_0}{2L_1} \quad (4.27)$$

where  $\omega_1$  is the actual signal frequency and  $\omega_{10}$  is the signal frequency when  $\psi_0 = 0$  (modulo  $2\pi$ ) and  $\Delta k = 0$ .

The second limiting case occurs when  $\Delta k \neq 0$  but  $\omega_1$  and  $\omega_2$  both lie exactly on a passive cavity resonance ( $\psi_1 + \psi_2 = 2m\pi$ ). Since in this case  $\psi_0 = 2m\pi - 2\Delta k\ell$ , the threshold is found from

$$\frac{g^2}{\gamma^2} \sinh^2 \gamma\ell = \kappa_{\min} + \tan^2 \phi \quad (4.28)$$

with  $\phi$  given by Eq. (4.15). For small gain ( $g\ell \ll 1$ ) and large  $\Delta k$  ( $\Delta k/2 \gg g$ ),  $\phi \approx 0$  and the threshold is given by

$$(g\ell)^2 = \frac{\kappa_{\min}}{\text{sinc}^2(\Delta k\ell/2)} \quad (4.29)$$

This result was first given by Giordmaine and Miller [6] and can also be derived from the results of Smith [10]. Note that in this approximation  $(g\ell)^2/\kappa_{\min}$  is independent of  $\kappa_{\min}$ ; changes in mirror

reflectivity have no effect on the threshold gain profile. Equation (3.11) gives the frequency deviation corresponding to a given  $\Delta k$  as

$$\delta\omega_k \equiv \omega_{1k} - \omega_{10} = \frac{(\Delta k \ell / 2)}{(\ell b_0 / 2)} \quad (4.30)$$

where  $\omega_{1k}$  is the actual signal frequency and  $\omega_{10}$  is the same as previously defined.

The ratio  $(g\ell)^2 / \kappa_{\min}$  represents the increase in threshold when the oscillator deviates from the optimum conditions  $\Delta k = 0$  and  $\psi_1 + \psi_2 = 2m\pi$ . This ratio is plotted in Fig. 4-2 as a function of  $\psi_0/2$  or  $\Delta k \ell / 2$  for the two limiting cases using Eqs. (4.25) and (4.29). The curves corresponding to variations in  $\psi_0$  are labeled according to the value of  $R$  used in calculating  $\kappa_{\min}$ . To convert the ordinate axis in Fig. 4-2 to frequency units, the following values are chosen:

$$\begin{aligned} L_1' &= 1.2 \text{ cm} \\ \ell &= 0.56 \text{ cm} \\ |b_0| &= 7.3 \times 10^{-13} \text{ sec/cm} \end{aligned} \quad (4.31)$$

These numbers correspond to the experimental conditions in Chap. 3 and Chap. 5 with  $\lambda_3 = 1.064\mu$  and  $\lambda_1 = 1.62\mu$  in  $\text{LiNbO}_3$ . With these numbers, Eqs. (4.27) and (4.30) give

$$\begin{aligned} \delta\nu_c &= \frac{\delta\omega_c}{2\pi c} = 0.133(\psi_0/2) \text{ cm}^{-1} \\ \delta\nu_k &= \frac{\delta\omega_k}{2\pi c} = 26(\Delta k \ell / 2) \text{ cm}^{-1} \end{aligned} \quad (4.32)$$

A given change in  $\Delta k \ell$  thus corresponds to a much larger change in frequency than a similar change in  $\psi_0$  and a very large frequency

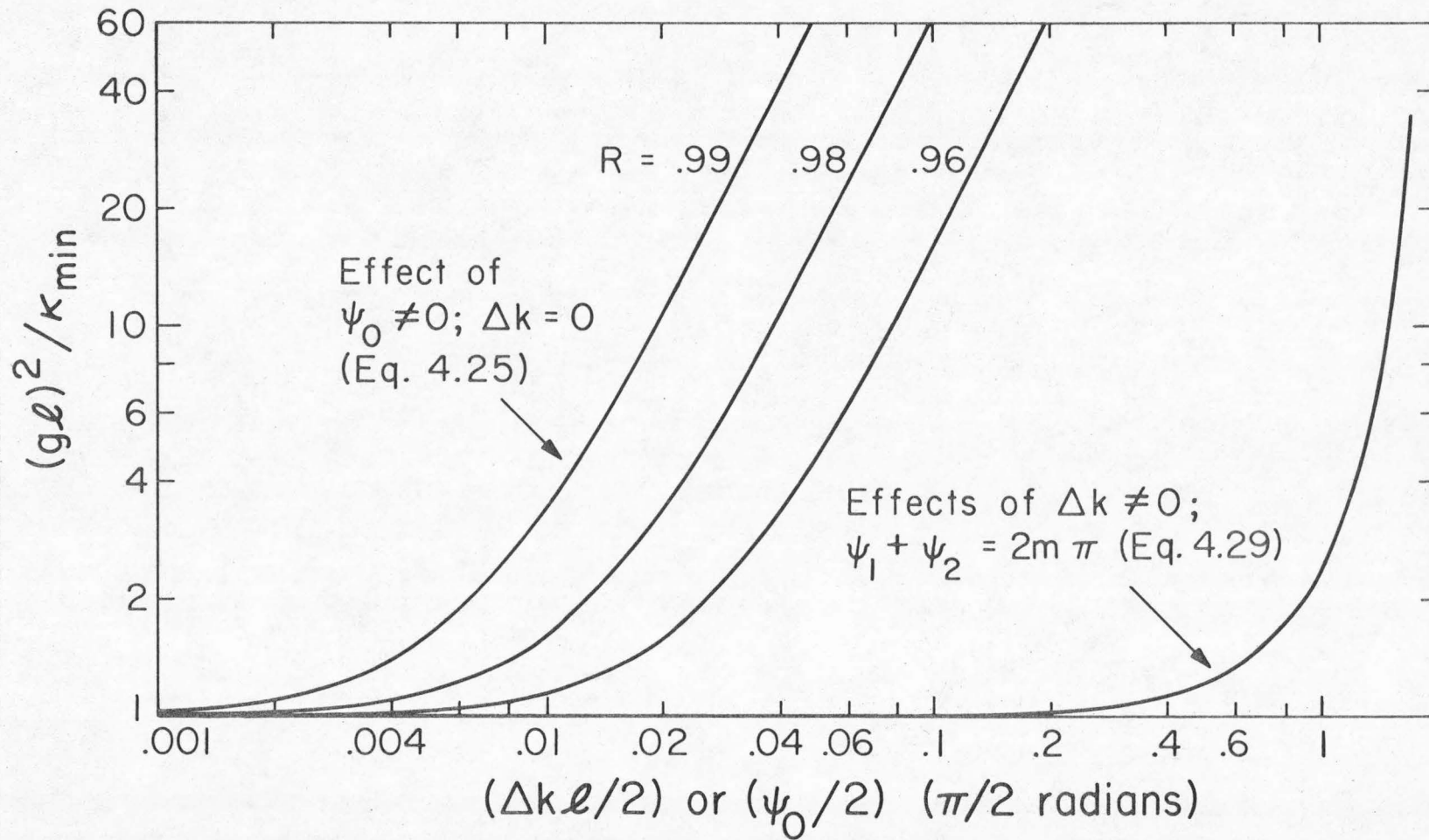


Figure 4-2. Increase in parametric oscillator threshold resulting from a change in the phase-mismatch  $\Delta k$  or the roundtrip phase  $\psi_0$ . The minimum threshold  $\kappa_{\min}$  occurs when  $\Delta k = 0$  and  $\psi_0 = 0$ .

shift is required before the threshold is affected by  $\Delta k \neq 0$ . Thus, as expected for high-Q cavities, deviation from the exact resonance condition produces a much larger increase in threshold than does a finite value of  $\Delta k$ . The actual operating frequencies will therefore be very near the passive-cavity resonant frequencies, and given a value for  $\psi_0$ , the oscillation frequencies at threshold are found from  $\Delta k \ell = -\psi_0/2$ . Note that if  $\psi_0$  varies randomly from  $-\pi$  to  $\pi$ , the oscillating frequencies will vary with an rms value corresponding to  $|\Delta k \ell| = \pi/4$  and a maximum value given by  $|\Delta k \ell| = \pi/2$  [8].

### Singly Resonant Oscillator

This case is by far the simplest to consider since now there are no constraints on the nonresonant field (taken here to be the idler at  $\omega_2$ ). When  $R_2 = 0$ , the phase condition, Eq. (4.16), gives the oscillating frequency for minimum threshold as

$$\psi_1 + \phi = 2m\pi \quad (4.33)$$

where  $m$  is an integer. Note that the oscillating frequency is shifted from the cold-cavity resonance ( $\psi_1 = 2m\pi$ ) when  $\Delta k \neq 0$  (see Eq. (4.15) for  $\phi(\Delta k)$ ). The amount of the shift when  $g\ell \ll 1$  and  $\Delta k/2 \gg g$  is very small since  $\phi \approx 0$  in this case. For all practical purposes, therefore, the oscillation frequencies of the singly-resonant oscillator are the passive-cavity resonant frequencies.

When  $\Delta k = 0$ , the oscillation threshold is given by Eq. (4.17c)

as

$$\sinh^2 g\ell = \frac{1 - R_1^2}{R_1^2} \quad (4.34)$$

or for  $R_1 \approx 1$ ,

$$(g\ell)_{\min}^2 = \frac{1 - R_1^2}{R_1^2} \approx \frac{2(1 - R_1)}{R_1^2} \quad (4.35)$$

When  $\Delta k \neq 0$ , the threshold is found from the more general expression

$$\frac{g^2}{\gamma^2} \sinh^2 \gamma \ell = \frac{1 - R_1^2}{R_1^2} \approx \frac{2(1 - R_1)}{R_1^2} \quad (4.36)$$

It is interesting to compare the threshold of a singly resonant oscillator (SRO) to that of an ideal doubly resonant oscillator (DRO) when  $\psi_0 = 2m\pi$  and  $\Delta k = 0$ . Recalling that  $P_{3T} \propto g^2$ , the result when  $g\ell \ll 1$  is

$$\frac{(P_{3T})_{\text{SRO}}}{(P_{3T})_{\text{DRO}}} = \frac{(R_1 + R_2)^2}{R_1^2(1 - R_2^2)} \quad (4.37)$$

and

$$\frac{(P_{3T})_{\text{SRO}}}{(P_{3T})_{\text{DRO}}} \approx \frac{2}{1 - R_2} \quad \text{for } R_1 \approx R_2 \approx 1 \quad (4.38)$$

The reflectance in Eq. (4.37) is that of the DRO; for the SRO,  $R_2 = 0$ . The approximate result, Eq. (4.38), has previously been given by Byer [11] and by Harris [12]. It can also be derived directly from Eqs. (2.21a) and (2.21b) using  $\alpha_j = 1/(1 - R_j)$ . The approximate result becomes exact when  $R_1 = R_2 = R$ . This conclusion follows directly from Eqs. (4.21) and (4.35).

D. Rise Time of Pulsed Parametric Oscillators

In a pulsed parametric oscillator driven by a Q-switched laser, the pump power will exceed oscillator threshold only for a limited time. Starting at threshold, the oscillator fields must build up from noise (parametric fluorescence). It is essential that the rise time of the power in the oscillator fields be less than the duration of the pumping pulse; otherwise oscillation levels will be very low and little power will be transferred from the pump to the oscillator fields.

Previous calculations of the rise time of parametric oscillators [11,13] have assumed a constant pump power and have neglected spatial variations of the oscillator signal and idler fields. Such results are not strictly applicable for pulsed oscillators and are inadequate to describe the rise time of a singly-resonant oscillator where the nonresonant field has a strong spatial variation. In this section the rise time of a pulsed doubly resonant oscillator (DRO) is calculated. A similar analysis which includes results for a singly-resonant oscillator is presented in Ref. 14. The results are used to derive relationships that must be obeyed by the various oscillator parameters to insure efficient power conversion. Numerical results using a Gaussian time envelope for the pump pulse are presented and significant differences are found between these results and rise time values computed using a square pump pulse and a steady-state analysis [11,12].

The theoretical analysis begins with the general interaction equations for the signal and idler fields found in Chap. 2 (Eqs.

(2.21)). Since the pump field will not be strongly depleted until the signal and idler fields build up to values comparable to the pump, pump depletion is neglected for calculating rise time. The pump, however, does have a "slowly-varying" time envelope which is characteristic of a Q-switched laser pulse. The pulsed nature of the pump is accounted for by writing it as

$$A_3(z,t) = A_{3p} f(t) \quad (4.39)$$

where  $A_{3p}$  is the peak value of the pump field at  $\omega_3$  and  $f(t)$  is a normalized Gaussian function. Note that the pump envelope is assumed independent of  $z$ . Defining  $t = 0$  as the time when the oscillator first reaches threshold, a pumping ratio  $N$  can be defined by

$$N = \frac{P_{3p}}{P_{3T}} = \frac{A_{3p}^2}{A_{3T}^2} = \frac{1}{f^2(0)} \quad (4.40)$$

The threshold for oscillation is  $P_{3T}$  and  $N$  is the factor by which the pump peak power exceeds threshold. The quantity  $P_{3T}$  as used here is the usual cw threshold\* (gain = loss) and may differ considerably from the experimentally observed threshold (minimum peak pump power for oscillation to occur).

The Gaussian time dependence of the pump field is written in the form

$$f(t) = \exp[-(t - \tau_T)^2 / b^2] \quad (4.41)$$

---

\* See Ref. 15 and Section C of this chapter.

where

$$b^2 = \frac{\tau_p^2}{2 \ln(2)}$$

and  $\tau_p$  is defined as the full-width at half-maximum of the pump pulse intensity. The quantity  $\tau_T$  is the time between the oscillator threshold level ( $t = 0$ ) and the peak of the pump pulse so that

$$\tau_T^2 = \frac{b^2 \ln(N)}{2} = \frac{\tau_p^2 \ln(N)}{4 \ln(2)} \quad (4.42)$$

with  $N$  being defined by Eq. (4.40). The relationships between the various quantities are illustrated in Fig. 4-3a.

The simplest case to consider is the DRO with equal losses at  $\omega_1$  and  $\omega_2$ . This is the usual case experimentally and will be the only one treated here. Setting  $\partial/\partial z = 0$  in Eqs. (2.21a) and (2.21b), integrating each over the cavity length, and solving the resulting time-dependent equations with initial conditions  $A_1(0) = A_{10}$  and  $A_2(0) = A_{20}$  gives

$$A_1(t) = \frac{1}{2} [(A_{10} + A_{20}) e^{ts_+(t)} + (A_{10} - A_{20}) e^{-ts_-(t)}] \quad (4.43)$$

where  $\beta = c\alpha/L'$  with  $\alpha$  the single-pass power loss at  $\omega_1$  and  $\omega_2$  and

$$ts_{\pm}(t) = \beta [\pm N^{1/2} g(t) - t] \quad (4.44)$$

The relative phase is time-independent when the initial condition is chosen as  $\Delta\phi = \Delta k\ell/2 + \frac{\pi}{2}$  to maximize the interaction, and the function  $g(t)$  is defined by

$$g(t) = \int_0^t f(t) dt = \frac{b\sqrt{\pi}}{2} \left[ \operatorname{erf}\left(\frac{t-\tau_T}{b}\right) + \operatorname{erf}\left(\frac{\tau_T}{b}\right) \right] \quad (4.45)$$

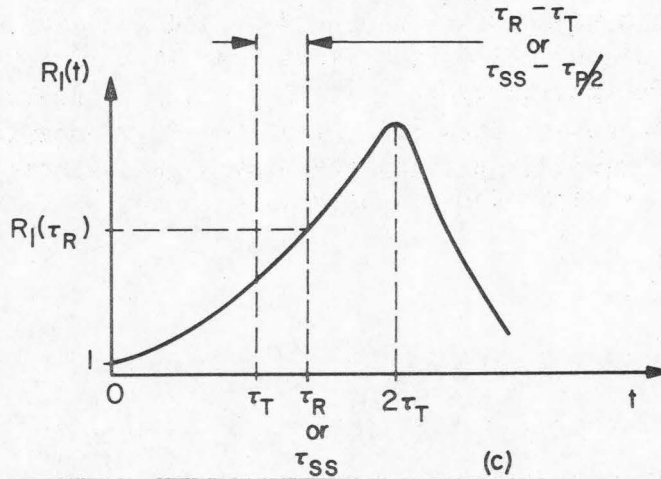
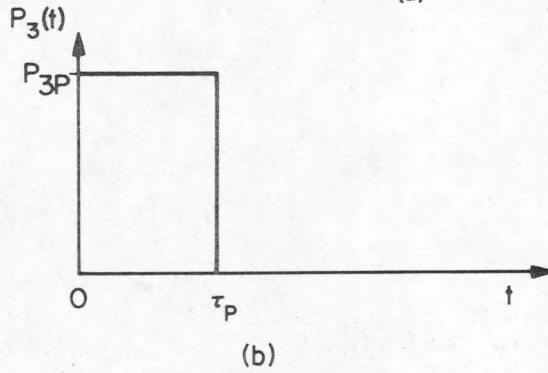
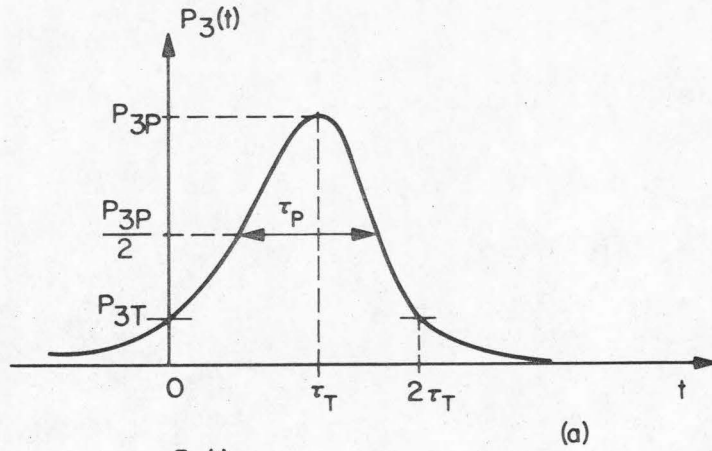


Figure 4-3. (a) Gaussian pump pulse defining the quantities  $\tau_T$ ,  $P_{3T}$ , and  $P_{3p}$ . Note  $t = 0$  is defined by the oscillator threshold level. (b) Square-pulse approximation to the Gaussian used with steady-state equations. (c) Qualitative plot of  $R_1(t) = P_1(t)/P_{10}$  showing the relationship between  $\tau_R$  and  $\tau_T$ . Note that in the undepleted pump approximation used here, the signal power continues to grow until the pump falls below threshold ( $t = 2\tau_T$ ).

The integral in (4.45) has been evaluated for  $f(t)$  as defined by Eqs. (4.41) and (4.42), and

$$\operatorname{erf}(x) = \frac{2}{\sqrt{\pi}} \int_0^x e^{-u^2} du \quad .$$

The initial values of the resonant fields are found from the parametric fluorescence power inside the resonator at threshold and within the bandwidth of the oscillator [11,16]. Since these values are many orders of magnitude below the oscillator operation level, only the rapidly growing part of Eq. (4.43) will contribute to the field at  $\omega_1$ . When the second term of (4.43) is neglected, the power output at  $\omega_1$  can be written as

$$P_1(t) = \frac{1}{4} (1 + \gamma)^2 P_1(0) e^{2ts(t)} = P_{10} e^{2ts(t)} \quad (4.46)$$

where from Eq. (4.43) and Ref. 16,

$$\gamma = \frac{A_{20}}{A_{10}} = \left[ \frac{\omega_1 P_2(0)}{\omega_2 P_1(0)} \right]^{1/2} = \frac{\omega_2 n_2}{\omega_1 n_1}$$

and

$$P_{10} = \frac{(1 + \gamma)^2}{4} P_1(0) \quad .$$

$P_{10}$  is the initial input to the signal oscillator mode.

The rise time of a parametric oscillator can be defined in a number of ways. A convenient operational approach is to define the rise time  $\tau_R$  as the time required for the signal output power  $P_{1e}$  to reach a predetermined value starting from the moment the pump reaches threshold. Assuming the only loss is due to output coupling, this definition of  $\tau_R$  can be written as

$$P_{1e}(\tau_R) \equiv \alpha P_1(\tau_R) = \text{constant} . \quad (4.47)$$

Since the initial internal signal power  $P_1(0) \equiv P_{10}$  is due to spontaneous parametric fluorescence driven by the threshold pump power,  $P_{10} \propto P_{3T}/\alpha$ . For the DRO, however,  $P_{3T} \propto \alpha^2$ , (see Eq. (4.29) with  $\alpha = 1/(1-R)$ ). Consequently, the constant appearing in Eq. (4.47) can be replaced by  $rP_{10}/\alpha$  where  $r$  is some constant. The risetime  $\tau_R$  is thus defined by the following equation:

$$R_1(\tau_R) \equiv \frac{P_1(\tau_R)}{P_{10}} = \frac{r}{\alpha^2} . \quad (4.48)$$

Combining Eqs. (4.48), (4.44), and (4.46) gives

$$\tau_{R^s}(\tau_R) = \frac{c\alpha}{L^{\dagger}} (N^{1/2} g(\tau_R) - \tau_R) = \frac{\ln(r/\alpha^2)}{2} . \quad (4.49)$$

Note that the ratio  $r/\alpha^2$  enters as the argument of a logarithm, so that the risetime is not strongly dependent on the value chosen for  $r$ .

Although in the sense defined here the oscillator is not "on" until Eq. (4.49) is satisfied, the oscillator is always "on" in the sense of the pump being above the cw threshold for all times in the range  $t = 0$  to  $t = 2\tau_T$ . The signal and idler fields experience a net round trip gain and thus grow in amplitude during this time period. The value of  $r$  chosen for calculating rise time is arbitrary, but fortunately, because of the "explosive" nature of the signal buildup,  $\tau_R$  is not a strong function of the ratio  $r/\alpha^2$ . A change of two orders of magnitude in  $r$  results in a change of  $\tau_R$  by only about 10%.

For experimental comparisons, a useful parameter is the quantity  $P_{3P}/(P_{3T}/\alpha^2) = N\alpha^2$  since the peak pump power is usually fixed and knowledge of the crystal parameters allows computation of the quantity  $P_{3T}/\alpha^2$ . Fixing  $N\alpha^2$  is equivalent to fixing the peak pump power and allows the effect of different cavity losses on rise time to be predicted. For most of the numerical results presented here, therefore, a normalized pump ratio  $N_o$  has been used instead of  $N$  as defined by Eq. (4.40) and is defined as the pumping ratio multiplied by the resonant loss in percent:

$$N_o = N(100\alpha)^2 \quad . \quad (4.50)$$

As noted previously, earlier calculations [11,13] of the doubly-resonant parametric oscillator rise time have assumed a constant pump power. This result can be found by setting  $f(t) = 1$  so  $g(t) = t$ ; Eq. (4.49) then gives

$$\tau_{ss} = \frac{L' \ln(r_{ss}/\alpha^2)}{2c\alpha(N^{1/2} - 1)} \quad . \quad (4.51)$$

The quantity  $r_{ss}/\alpha^2$  is the ratio of the external cavity steady-state power to the initial internal power and  $\tau_{ss}$  is the time required to reach steady-state. This result has previously been derived by Kreuzer [13] and by Byer [11] using a slightly different definition of rise time. One possible way of using Eq. (4.51) to predict the rise time of a pulsed oscillator is to assume the pump pulse is a square pulse of width  $\tau_p$  as shown in Fig. 4.3b. The magnitude of the square pulse is taken to be the same as the peak of the Gaussian pulse

defining  $\tau_p$ . For the sake of comparison, the predictions obtained using this quasi-steady-state approach are also shown as light curves in Figs. 4-4 and 4-5.

Results for the DRO for two values of  $\tau_p$  are shown in Figs. 4-4 to 4-6. Figure 4-4 shows the effect of losses on DRO risetime and Fig. 4-5 gives the ratio  $\tau_R/\tau_p$  (or  $\tau_{ss}/\tau_p$ ) as a function of cavity length for different pump ratios. The ordinate axis in Fig. 4-6 is the time between the peak of the pump pulse and the moment the oscillator turns "on" (see Fig. 4-3) divided by  $\tau_p$ . This is the time most convenient to measure experimentally and so is the most useful comparison to experiment. It is also the time relative to the peak of the pump pulse that pump depletion and gain saturation begin, and thus is a measure of the degree of quasi-steady-state operation.

A value of  $r = 10^8$  has been used in all calculations. For an initial internal power  $P_{10} = 10^{-10}$  watts, this choice of  $r$  corresponds to an external power of  $10^{-2}$  watts and for  $\alpha_1 = 1\%$  an internal power of 1 watt. Risetime values have also been computed using values of  $r = 10^6$ ,  $10^{10}$ , and  $10^{12}$ . A change of two orders of magnitude in  $r$  changes  $\tau_R$  by roughly 10%. The value of  $r$  makes a significant difference in the calculated value of  $\tau_R$  only when the parameters  $\tau_p$ ,  $L'$ ,  $\alpha$ , and  $N_0$  are such that the "on" condition can barely be achieved.

It is apparent from the figures that the risetime can be longer than the pump pulse width  $\tau_p$ . The important quantity, however, is  $\tau_R$  compared to  $\tau_T$  (see Fig. 4-3c). If  $\tau_R > 2\tau_T$ , the oscillator will not turn "on" in the practical sense that the output

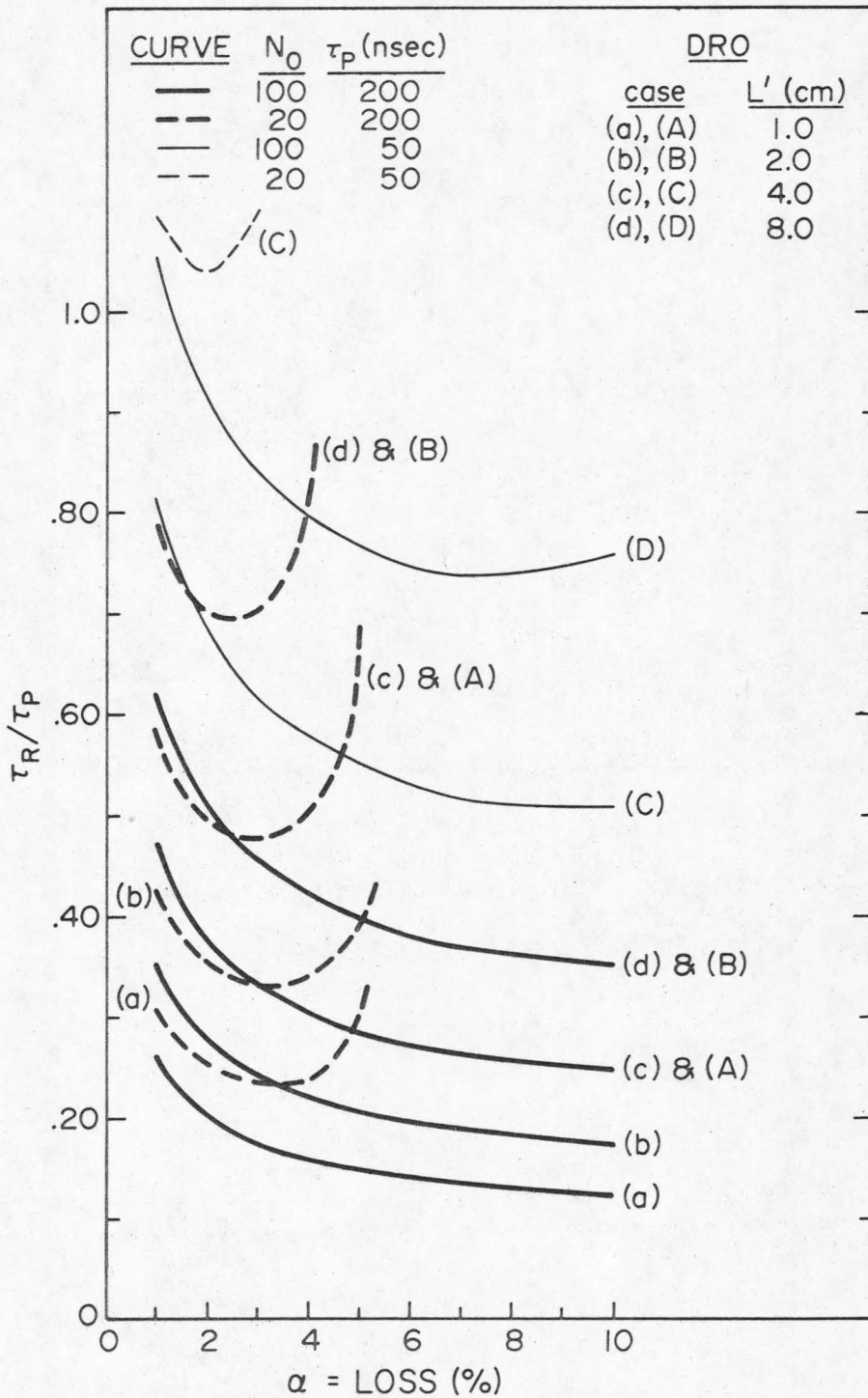


Figure 4-4. DRO absolute risetime divided by pump pulse width versus resonant loss for various values of cavity optical length and normalized pumping ratio.  $\tau_p = 200$  nsec (heavy lines) or 50 nsec (light lines), and  $r = 10^8$ .

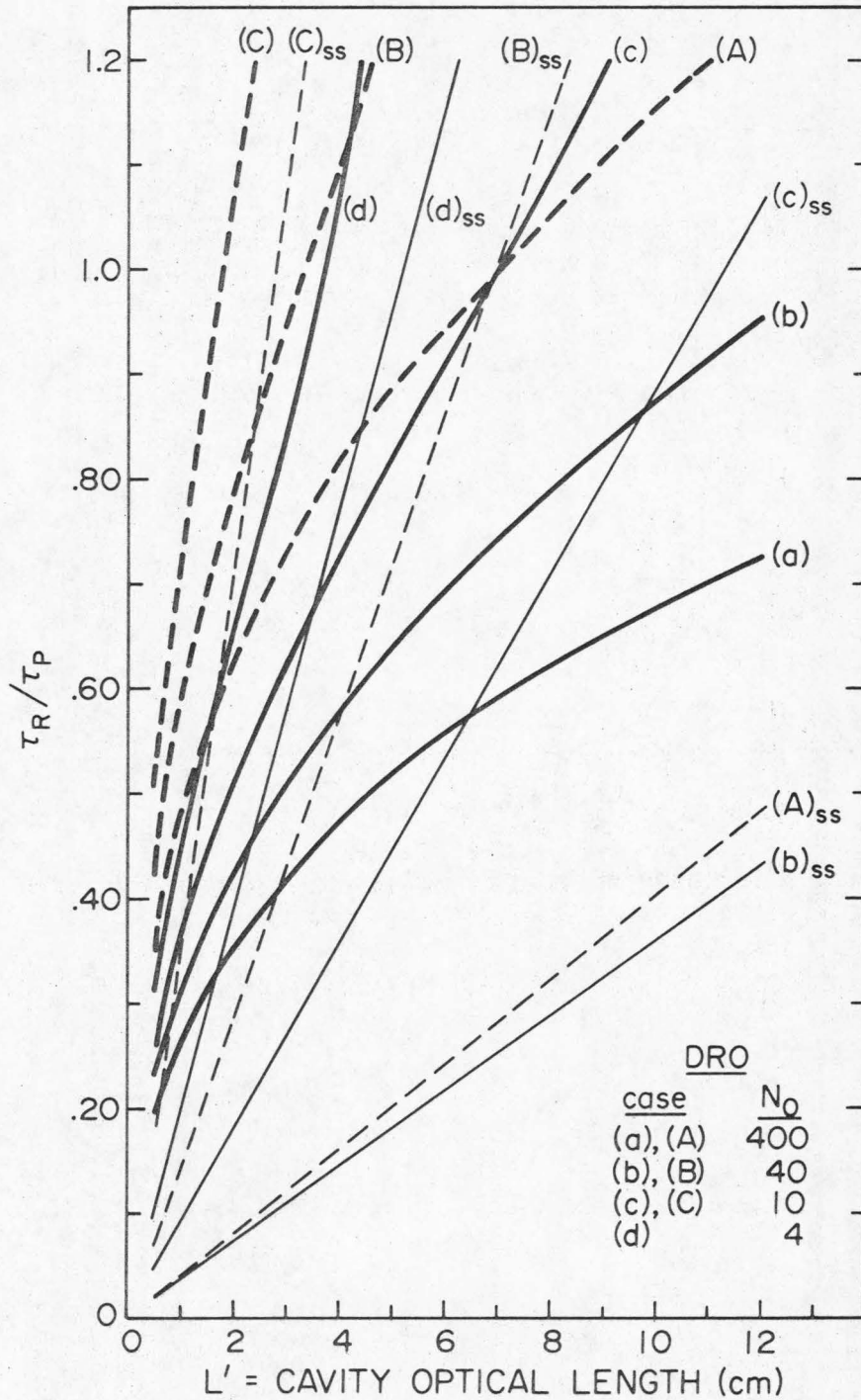


Figure 4-5. DRO absolute risetime divided by pump pulse width as a function of cavity optical length for various normalized pump ratios.  $\tau_p = 200$  nsec (solid lines) or 50 nsec (broken lines),  $\alpha = 1\%$ ,  $r = 10^8$ . The light lines are results using the steady-state formula, Eq. (4.51).

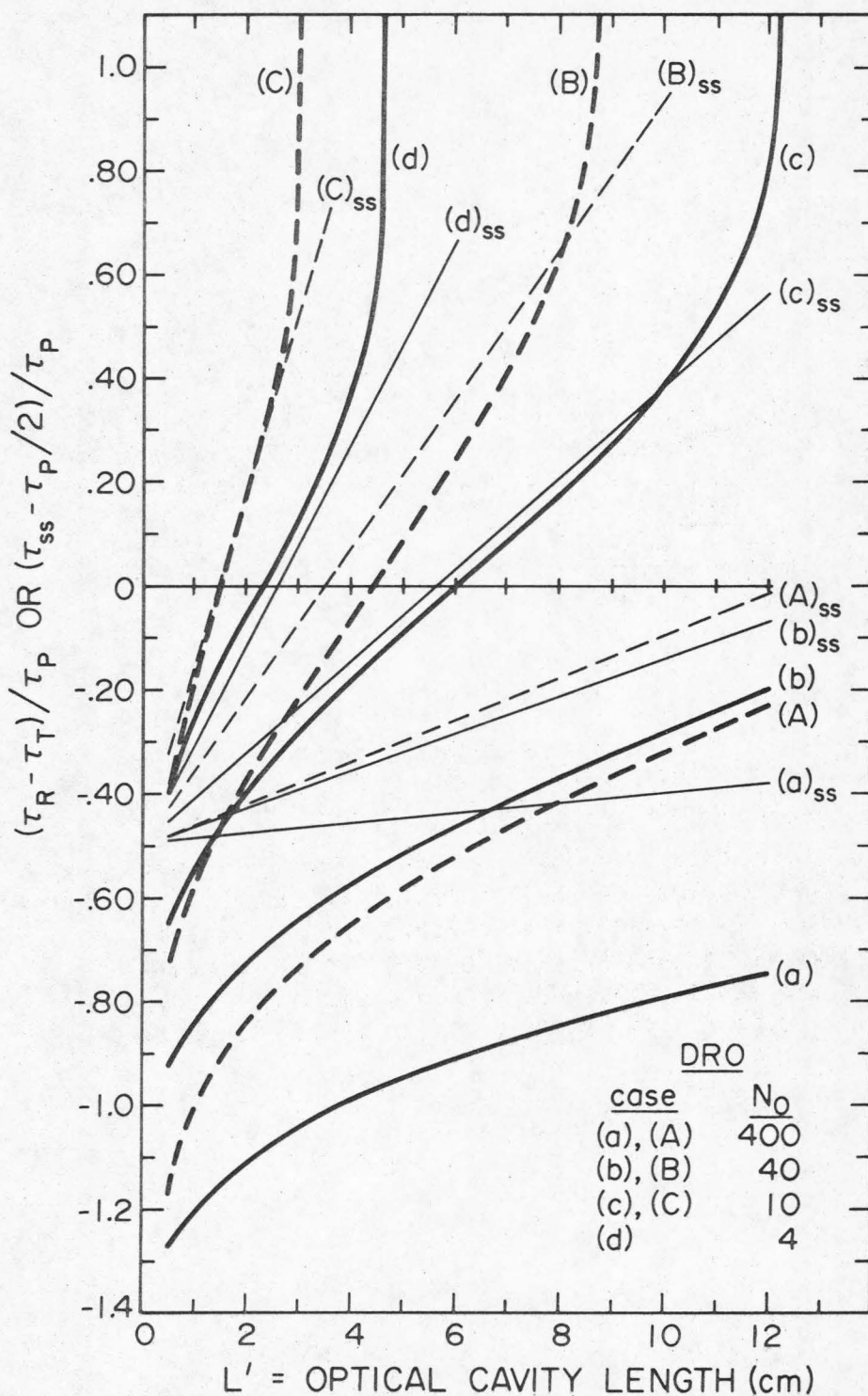


Figure 4-6. DRO risetime relative to peak of Gaussian pump pulse divided by  $\tau_p$  plotted as a function of cavity optical length.  $\tau_p = 200$  nsec (solid lines) or 50 nsec (broken lines),  $\alpha = 1\%$ ,  $r = 10^8$ . The light lines are results using the steady-state formula, Eq. (4.51).

power will never reach the preselected level. Inspection of Eq. (4.49) shows that the maximum value of  $\tau_R s(\tau_R)$  occurs for  $\tau_R = 2\tau_T$  at which point the pump power again crosses the threshold level (see Fig. 4-3a). Use of this value for  $\tau_R$  in (4.49) will define a minimum allowable pump ratio  $N_{\min}$  given  $\alpha$  and  $L'$  or conversely, a maximum cavity optical length  $L'_{\max}$  given  $N$  and  $\alpha$ . These extrema are given by the solutions to the following equations:

$$e^{x^2} \operatorname{erf}(x) - \frac{2}{\sqrt{\pi}} x = \frac{L' \ln(r/\alpha^2)}{2cb \alpha \sqrt{\pi}} \quad (4.52)$$

where

$$x^2 = \frac{\ln(N_{\min})}{2}$$

and

$$L'_{\max} = \frac{2c \alpha b \sqrt{\pi}}{\ln(r/\alpha^2)} [N^{1/2} \operatorname{erf}(y) - \frac{2}{\sqrt{\pi}} y] \quad (4.53)$$

with  $y^2 = \ln(N)/2$ .

The corresponding quantities using the steady-state approximation of a square pulse and Eq. (4.51) are

$$(N_{\min})_{ss} = \left( \frac{L' \ln(r/\alpha^2)}{2c \alpha \tau_p} + 1 \right)^2 \quad (4.54)$$

$$(L'_{\max})_{ss} = \frac{2c \alpha \tau_p (N^{1/2} - 1)}{\ln(r/\alpha^2)} \quad (4.55)$$

Predictions of Eqs. (4.52) - (4.55) are shown in Figs. 4-7 and 4-8 for two values of  $\tau_p$ . Note that the normalized pump ratio  $N_o$  defined by Eq. (4.50) is used in Fig. 4-12. From the curves in Figs. 4-5 to 4-8 it can be seen that the results of the steady-state approximation

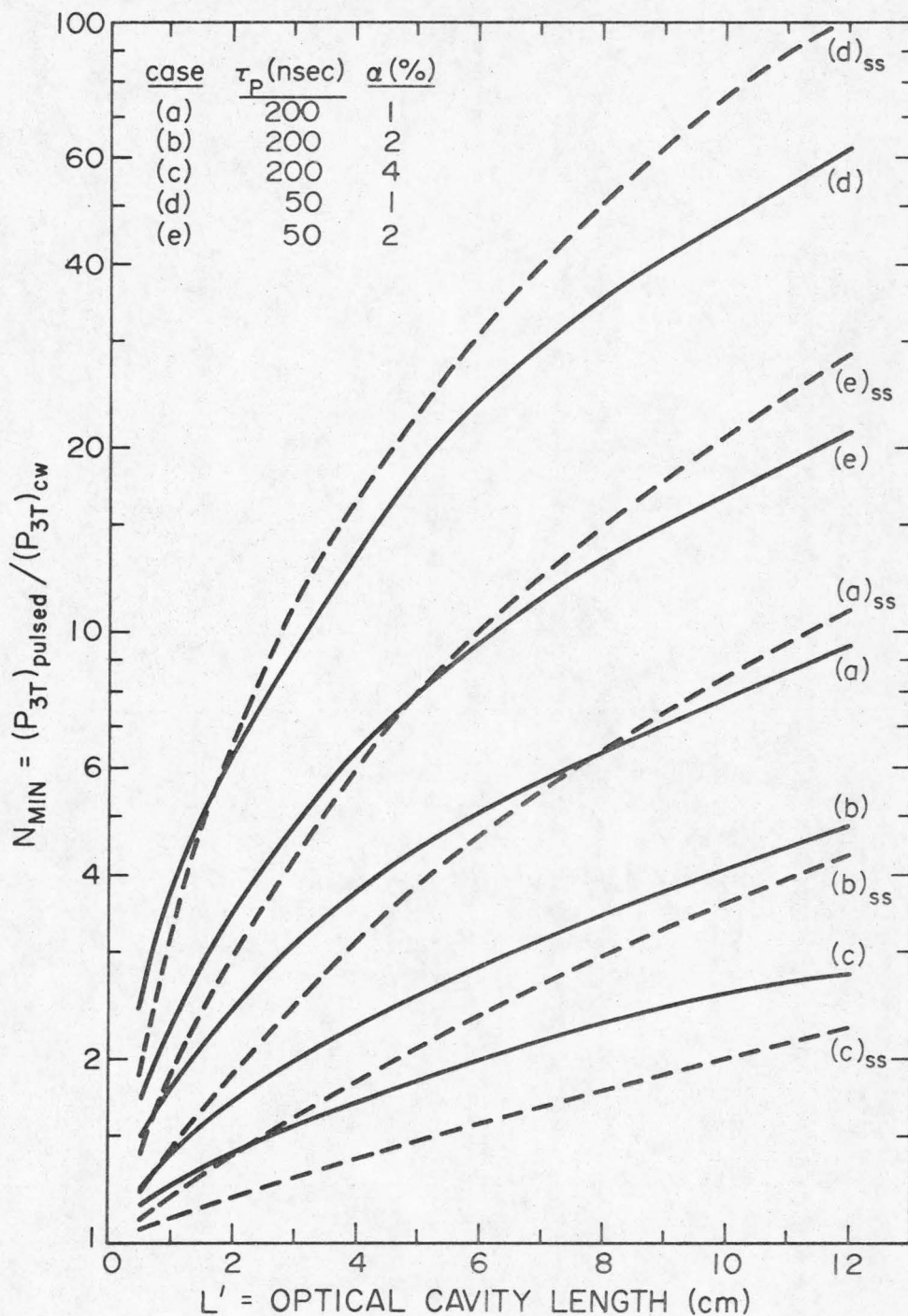


Figure 4-7. Minimum pump ratio for a DRO to reach the condition  $r = 10^8$ . Various cases of  $\alpha$  and  $\tau_p$  are shown versus cavity optical length. The dashed lines are results of the steady-state formula, Eq. (4.54). The value  $N_{min} = 1$  at  $L' = 0$  corresponds to cw threshold (see text).

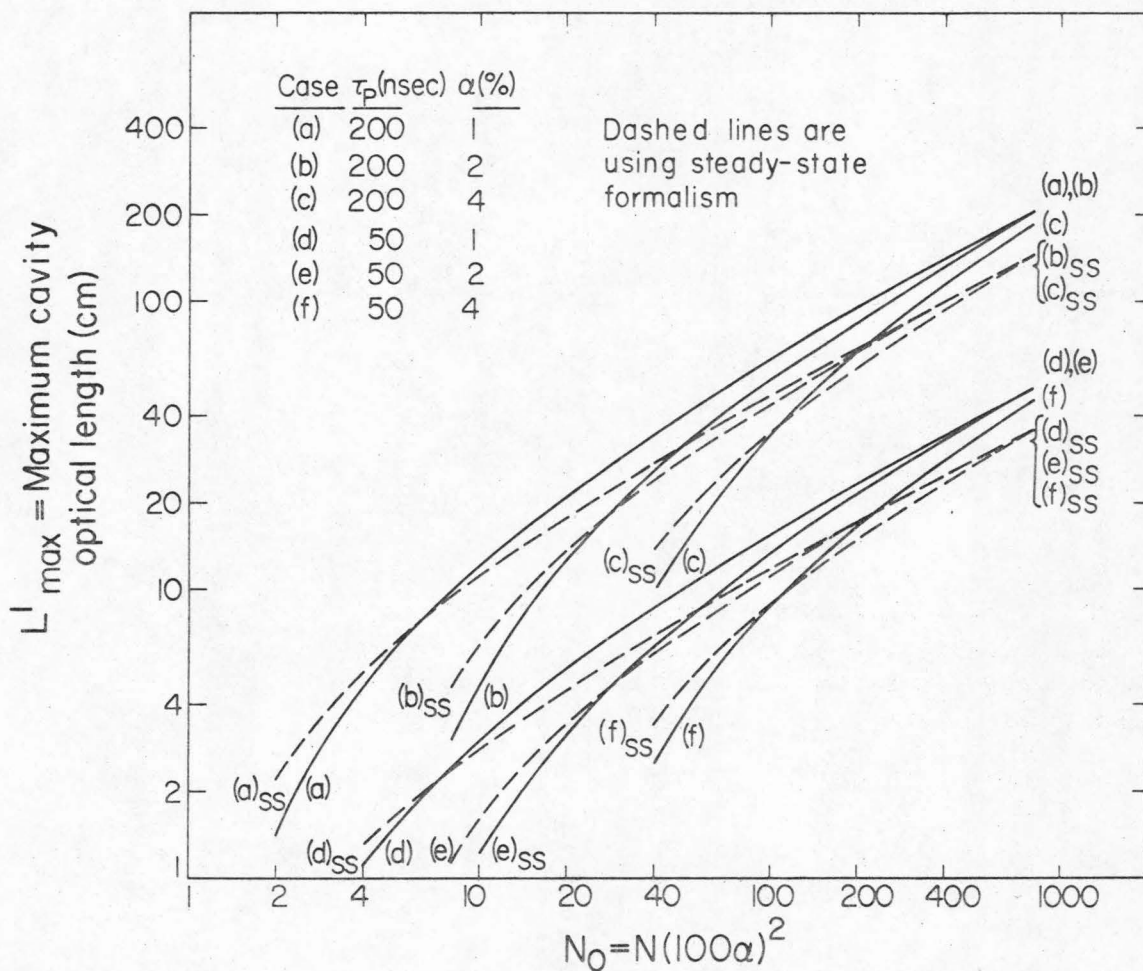


Figure 4-8. Maximum cavity optical length for a DRO to reach the condition  $r = 10^8$ . Various cases of  $\alpha$  and  $\tau_p$  are shown versus cavity optical length. The dashed lines are results of a steady-state formula, Eq. (4.55).

are generally unreliable but might be used for a rough estimate.

The quantity  $N_{\min}$  as defined by Eq. (4.52) and plotted in Fig. 4-7 is the factor by which the pulsed threshold is increased due to the finite oscillator rise time. Once the cw threshold has been calculated (using the results of Ref. 15, for example) and a cavity length chosen, the actual pulsed threshold is found by multiplying the cw result by  $N_{\min}$  to obtain the threshold peak pump power. The pulsed oscillator threshold is thus defined by the minimum peak pump power for which the oscillator will turn on rather than the pump power which gives a net gain at the signal and idler frequencies. Note that if rise time were not an important consideration (i.e., cw case),  $N_{\min} = 1$ . If the peak pump power is fixed ( $N_0$  is given), the maximum allowable cavity length can be found from Fig. 4-8. Note that for  $L' = L'_{\max}$  or  $N = N_{\min}$  the oscillator is driven at the "pulsed threshold" level.

It should be noted that the minimum pump values shown in Fig. 4-7 would apply for a perfectly adjusted oscillator pumped by a single-frequency pump. In a practical situation, a safety margin of about an order of magnitude in the pumping ratio would insure ease of cavity alignment and stable, reproducible operation, as well as insuring significant energy conversion from the pump to the signal and idler fields.

Several experimental parametric oscillator results have been published and have included oscilloscope traces of the pump and signal output pulses. From these data, values of  $(\tau_R - \tau_T)$  can be found and compared to theoretical predictions. From the experimental photographs

the time ( $\tau_R - \tau_T$ ) is defined by the onset of pump depletion or by the leading edge of the oscillator pulse if no depletion is evident. Table 4-1 summarizes the results of a number of authors. The theoretical values for the singly-resonant oscillator (SRO) cases have been calculated using the results of Ref. 14.

The values of  $N$  shown in Table 4-1 are quite approximate. Where enough information was supplied, the measured peak pump power and the theoretical cw threshold were used to find  $N$ . Otherwise  $N$  was computed using the measured threshold power. Considering the approximate nature of the experimental data, the agreement with theory is considered reasonable.

Table 4-1

N* (approx)	$\alpha^{**}$ (%)	$\tau_p$ (nsec)	L' (cm)	$\tau_R - \tau_T$ measured (nsec)	$\tau_R - \tau_T$ calc. (nsec)	Ref.
3	15(SRO)	16	2.7	0	-1	17
20-40	6(SRO)	22	13.5	-4 to -8	-6 to -11	18
1.5	16(SRO)	25	7.1	-5 to 0	-15	20
4	14(SRO)	12	2.7	0	-2	21
20	15(DRO)	22	2.7	-12	-15	17
10-20	1.25(DRO)	180	5.4	0 to -25	-21 to -64	19
16	17(DRO)	15	2.7	-6	-9	21

Table 4-1. Relative rise time values found in the literature compared to calculated values for same values of  $\alpha$ ,  $\tau_p$ , L', and N. A value of  $r = 10^8$  is used for the calculated values.

\* Care must be taken in defining measured threshold for pulsed oscillators. The results discussed in Ref. 21 have been used where possible in selecting the value of N used here.

\*\* In cases of the DRO where  $\alpha_1 \neq \alpha_2$ , a value of  $\alpha = \sqrt{\alpha_1 \alpha_2}$  is assumed.

### E. Oscillator Bandwidth and Stability

There are a number of factors which act simultaneously to determine the bandwidth and frequency stability of an optical parametric oscillator (OPO). First, the parametric gain linewidth will determine the range of frequencies which are above threshold for a given input pump power. The degree of pump depletion (gain saturation) will then determine which frequencies see sufficient gain to oscillate. Second, the oscillator bandwidth will be directly related to the pump linewidth since  $\omega_3 = \omega_1 + \omega_2$ . Finally, the long-term average oscillator bandwidth and stability will be affected by the frequency stability of the pump laser and by the mechanical and thermal stability of the oscillator resonator.

Although all of these factors act together to determine the observed bandwidth of an OPO, it is useful to consider each one separately to get an estimate of their relative magnitudes. Consider first the effect of the parametric gain linewidth when the pump is single-frequency and the OPO resonator is perfectly stable. The oscillator unsaturated gain linewidth can be found by analyzing the gain of a parametric amplifier [10], by looking at the minimum bandwidth of parametric fluorescence (see Chap. 3 and Ref. 11), or by looking at the oscillator threshold as a function of frequency as in Section C of this chapter. In the appropriate limit, each of these views shows the linewidth varying as  $\text{sinc}^2(\Delta k\ell/2)$ . In the case of non-steady-state operation where the oscillator gain does not saturate (no pump depletion), the OPO bandwidth would be determined by the width of the  $\text{sinc}^2(\Delta k\ell/2)$

curve and how far above the minimum threshold the OPO is pumped.

If the oscillator could reach a steady-state condition, however, the resonant mode with the highest gain would deplete pump and clamp the gain at the threshold level of this mode. All adjacent modes would thus be below threshold and the oscillator would behave like a homogeneously saturated laser with a single longitudinal mode output. Kreuzer [3] has analyzed this situation for the singly-resonant oscillator and has found that single-mode operation is possible only for pumping levels such that  $P_3/P_{3T} \leq 4.6$  although two mode operation should be possible for  $P_3/P_{3T} \leq 11$ .

The key assumption in the above statements is that steady-state operation occurs. The single frequency operation and homogeneous-saturation behavior will occur only if the OPO can reach a steady-state condition; the pump is then depleted sufficiently to allow only one mode to remain above threshold. In pulsed lasers, this condition can rarely be achieved unless the pumping level is near the threshold of the lowest threshold mode. At strong pumping levels, many oscillator modes will be above threshold and many frequencies will be able to oscillate before pump depletion sets in. The number of modes above threshold can be estimated using Eq. (4.30) and the longitudinal mode spacing  $\Delta\omega_c = \pi c/L_1'$ . The result is

$$\left. \begin{array}{l} \text{Number of} \\ \text{modes above} \\ \text{threshold} \end{array} \right\} = n \approx \frac{2|\Delta k l / 2|}{c|b_o|l} L_1' \quad (4.56)$$

where  $\Delta k l / 2$  is measured in units of  $\pi/2$ . The value of  $|\Delta k l / 2|$  can be found from Fig. 4-2 once a value of  $N = (g l)^2 / \kappa_{\min} = P_{3P} / P_{3T}$  is

chosen. As a numerical example, choose  $N = 5$  and use the numbers given in (4.31). The result is  $n \approx 250$  or  $\Delta\nu_1 \approx 210 \text{ cm}^{-1}$  for the 1.2 cm OPO cavity optical length. This type of broadening can be eliminated by using mode-selecting etalons [22] inside the OPO resonator. Kreuzer [23] has demonstrated the usefulness of this technique for a pulsed SRO.

Consider next the effects of pump bandwidth on the OPO spectral output when all other conditions are ideal. Defining  $\omega_{j0}$  as a set of frequencies giving  $\Delta k = 0$ , expanding each wave vector  $k_j$  about the appropriate frequency, and using Eq. (4.3) gives

$$\Delta\omega_3 k_3' = \Delta\omega_1 k_1' + \Delta\omega_2 k_2' \quad (4.57)$$

where

$$k_j' = \left. \frac{\partial k_j}{\partial \omega_j} \right|_{\omega_{j0}}, \quad j = 1, 2, 3 \quad (4.58)$$

Since  $\omega_3 = \omega_1 + \omega_2$ ,  $\Delta\omega_3 = \Delta\omega_1 + \Delta\omega_2$  and the change in  $\omega_1$  for a given  $\Delta\omega_3$  is

$$\Delta\omega_1 = \frac{b_{32}}{b_0} \Delta\omega_3 \quad (4.59)$$

where

$$b_0 = k_1' - k_2' \quad (4.60)$$

and

$$b_{32} = k_3' - k_2'$$

Similarly, the effect on the idler frequency is given by

$$\Delta\omega_2 = \frac{-b_{31}}{b_0} \Delta\omega_3 \quad (4.61)$$

where  $b_{31} = k'_3 - k'_1$ . Eqs. (4.59) and (4.61) both apply to a doubly resonant oscillator.

Although it has not been formally proven, in an SRO the resonant signal field should be nearly single-frequency with the nonresonant idler picking up the pump bandwidth. In this case Eq. (4.61) gives the nonresonant idler bandwidth. A restriction on the usable pump bandwidth in an SRO can be found from Eq. (4.59) or Eq. (4.61) by setting  $b_o \Delta\omega_1$  or  $b_o \Delta\omega_2$  equal to  $\pi/l$ . Solving for  $\Delta\omega_3$  then gives the maximum pump linewidth which can be effective in driving the oscillator. Eq. (4.59) gives this bandwidth for a resonant-signal SRO and Eq. (4.59) gives the result for a resonant-idler SRO. The allowable bandwidths for each case are shown in Fig. 4-9 as a function of signal wavelength for several pump wavelengths in  $\text{LiNbO}_3$ . The index data of Ref. 24 have been used and the crystal length is 1 cm. For wide-bandwidth pumps, it is clear from Fig. 4-9 that resonating the idler instead of the signal may make a considerable difference in oscillator threshold because more of the total pump power can drive the oscillator. This restriction has been graphically demonstrated for a  $0.473\mu$  pump in  $\text{LiNbO}_3$  [25].

For a numerical example of the effect of pump bandwidth in a DRO, take  $\Delta\nu_3 = \Delta\omega_3/2\pi c \approx .01 \text{ cm}^{-1}$  (2 longitudinal modes in a 50 cm laser cavity). In  $\text{LiNbO}_3$ ,  $|b_{32}| \approx 1.1 \times 10^{-12}$ ,  $|b_{31}| \approx 3.7 \times 10^{-13}$ , and  $|b_o| \approx 7.3 \times 10^{-13}$  for a  $1.064\mu$  pump and  $\lambda_1 \approx 1.62\mu$ . Equation (4.59) then gives  $\Delta\nu_1 = .015 \text{ cm}^{-1}$  or only 1/30 of the OPO mode spacing (using  $L'_1 = 1.2 \text{ cm}$ ). Equation (4.61) gives  $\Delta\nu_2 = .0051 \text{ cm}^{-1}$  or 1/80 the longitudinal mode spacing.

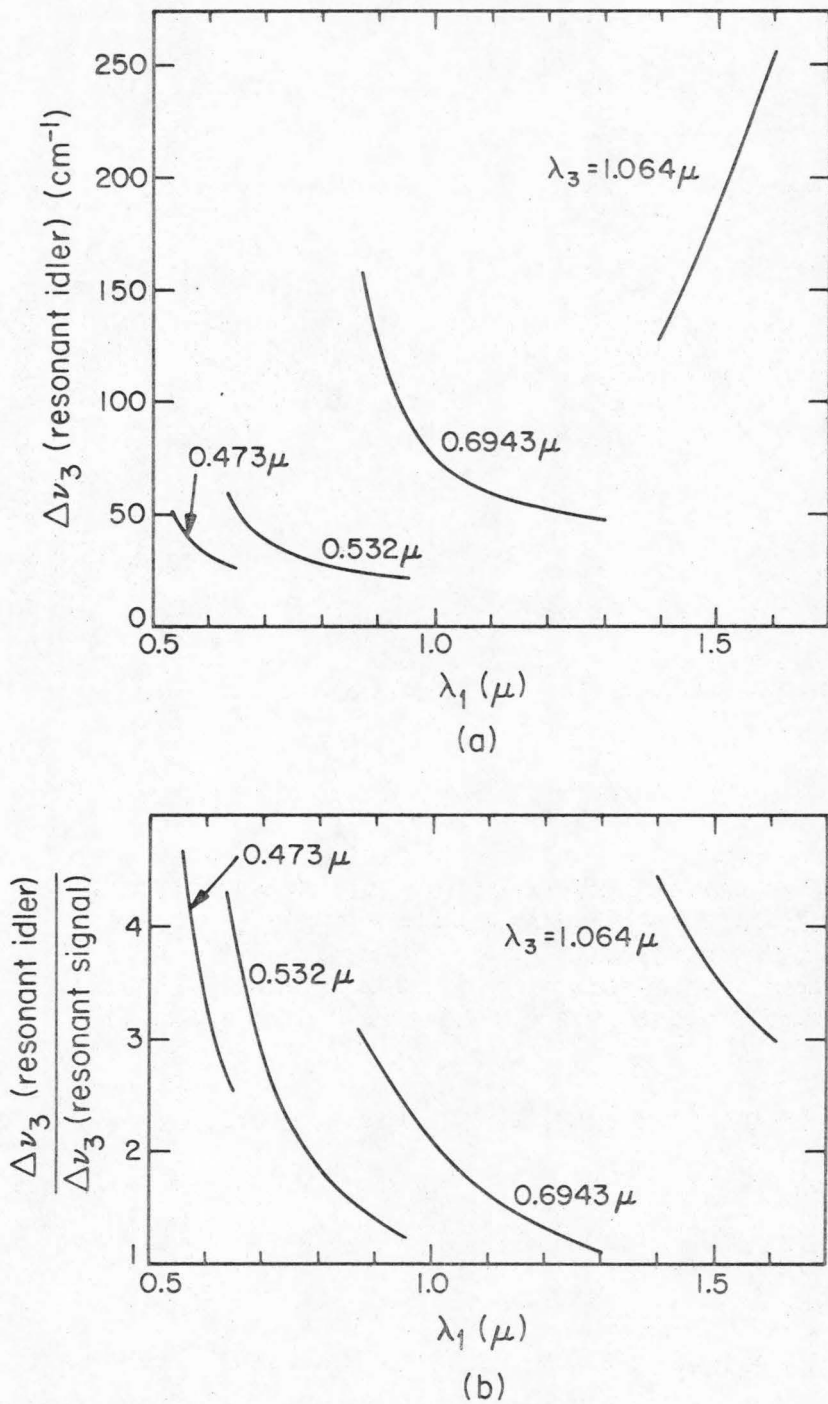


Figure 4-9. Pump linewidth requirements versus signal wavelength ( $\lambda_1$ ) for parametric oscillators using different pump wavelengths ( $\lambda_3$ ). (a) Maximum allowable pump linewidth for a resonant-idler OPO. (b) Ratio of allowable pump linewidth for a resonant-idler OPO to that for a resonant signal OPO.

Although the factors discussed above can give sizable contributions to the bandwidth of a parametric oscillator, the largest contribution usually results from mechanical and thermal instabilities. If the cavity optical length changes by one-half of an optical wavelength, the high-Q modes of the resonator shift by  $1/2$  of their spacing. Since both  $\omega_1$  and  $\omega_2$  must lie very near a cavity resonance<sup>\*</sup>, arbitrary shifts in the cavity optical length (or roundtrip phase-change) can cause large excursions in operating frequency. This "mode-hopping" was first noted by Giordmaine and Miller [6] and has been used to explain much of the frequency instability observed in doubly resonant oscillators [17,19,26,27]. By using an analysis similar to Section C of this chapter, Falk [8] has shown that unless the idler reflectivity is below about 5%, the resonant-signal SRO will have nearly the same frequency instability as the DRO. Falk's analysis is limited to the non-depleted pump case near oscillator threshold, but qualitatively explains why some singly-resonant oscillators do not exhibit a much smaller bandwidth than similar doubly-resonant oscillators [26].

As pointed out in Section C, if the roundtrip phase change at a resonant frequency varies randomly from  $-\pi$  to  $\pi$ , then the average value of  $|\Delta k l / 2|$  which gives minimum threshold will be  $\pi/8$  for the DRO and the SRO when  $R_2 \geq 5\%$  [8]. The average number of modes above threshold is found from (4.31) and Eq. (4.56) to be  $n \approx 49$  or  $\Delta \nu_1 \approx 41 \text{ cm}^{-1}$  for  $L_1' = 1.2 \text{ cm}$ . Gain saturation will probably reduce this number, but cavity instabilities will usually produce the main contribution to OPO bandwidth.

---

<sup>\*</sup> See Section C of this chapter, Eq. (4.28) ff.

The roundtrip phase change at  $\omega_1$  due to a change in cavity optical length is given by

$$\Delta \phi = \frac{2\pi}{\lambda_1} \Delta L' . \quad (4.62)$$

Assuming the crystal length  $\ell$  and index of refraction  $n$  change only with temperature,  $\Delta L'$  is given by

$$\Delta L' = n \left[ \frac{1}{n} \frac{dn}{dT} + \frac{1}{\ell} \frac{d\ell}{dT} \right] \Delta T + \Delta L_a + \frac{d(L-\ell)}{dT} \Delta T . \quad (4.63)$$

The variations of the total cavity length,  $\Delta L_a$ , are assumed to be due to vibrations (microphonics). The phase change  $\Delta\phi$  will thus vary from  $-\pi$  to  $\pi$  if  $\Delta L_a$  changes by one wavelength or if  $\Delta T$  is large enough to produce a similar change. The two effects can act together, of course, or one may be used to offset changes in the other, thus acting to stabilize the OPO.

When all of the sources of OPO bandwidth act together, a number of interesting effects can occur. First, since the gain linewidth is very broad compared to the spacing of the cavity resonances, many modes will have nearly the same threshold. The non-steady state behavior of the OPO coupled with any small instabilities will result in a "cluster" of modes oscillating. The number of modes in the cluster will depend on all of the factors previously discussed. If the pump is strong enough or if the instabilities are large enough, or both, then a number of "clusters" may oscillate, perhaps even simultaneously [13,26].

If the pump is multi-frequency, then the individual modes in each cluster can be "smeared out" so that a near-continuum of frequencies oscillates over a small range. For a strong, broad-band pump and large instabilities, even the individual cluster structure could be washed out and a large, nearly-continuous range of frequencies would oscillate.

It is difficult to estimate how much each of the above effects will contribute to the bandwidth of a particular OPO. The pump linewidth and temperature instabilities can be measured, but mechanical instabilities and the degree to which steady-state operation is achieved can be estimated only qualitatively. In Chap. 5, experimental studies of OPO bandwidth are compared to the possible contributions from each source of increased bandwidth. Each contribution can then be defined in more quantitative terms.

Chapter 4

References

1. A. E. Siegman, "Nonlinear Optical Effects: An Optical Power Limiter", *Appl. Opt.* 1, pp. 739-744 (1962).
2. J. E. Bjorkholm, "Analysis of the Doubly-Resonant Optical Parametric Oscillator Without Power-Dependent Reflections", *IEEE J. Quant. Electr.* QE 5, pp. 293-295 (1969).
3. L. B. Kreuzer, "Single and Multimode Oscillation of the Singly Resonant Optical Parametric Oscillator", *Proc. Joint Conf. Lasers and Opto-Electron.* (Univ. of Southampton, I.E.R.E., London), pp. 52-63 (1969).
4. J. A. Armstrong, N. Bloembergen, J. Ducuing, and P. S. Pershan, "Interactions Between Light Waves in a Nonlinear Dielectric", *Phys. Rev.* 127, pp. 1918-;939 (1962).
5. R. L. Byer, A. Kovrigin, and J. F. Young, "A cw Ring - Cavity Parametric Oscillator", *Appl. Phys. Lett.* 15, pp. 136-137 (1969).
6. J. A. Giordmaine and R. C. Miller, "Optical Parametric Oscillation in  $\text{LiNbO}_3$ ", in Physics of Quantum Electronics, P. O. Kelley, B. Lax, and P. E. Tannenwald, Eds. (McGraw-Hill Book Co., New York, 1966), pp. 31-42.
7. M. Born and E. Wolf, Principles of Optics, 3rd. Ed., Chap. 7, Pergamon Press, 1965).
8. J. Falk, "Instabilities in the Doubly Resonant Parametric Oscillator: A Theoretical Analysis", *IEEE J. Quant. Electron.* QE-7, pp. 230-235 (1971).
9. A. Yariv and J. E. Pearson, "Parametric Processes", in Progress in Quantum Electronics, Vol. 1 (Pergamon Press, 1969).
10. R. G. Smith, "Effects of Momentum Mismatch on Parametric Gain", *J. Appl. Phys.* 41, 4121-4124 (1970).

11. R. L. Byer, "Parametric Fluorescence and Optical Parametric Oscillation", Ph.D. Thesis (Available as Mil. Report No. 1711), Stanford University, 1968.
12. S. E. Harris, "Tunable Optical Parametric Oscillators", Proc. IEEE 57, pp. 2096-2113 (1969).
13. L. B. Kreuzer, "High-Efficiency Optical Parametric Oscillation and Power Limiting in  $\text{LiNbO}_3$ ", Appl. Phys. Lett. 13, pp. 57-59 (1968).
14. J. E. Pearson, U. Ganiel, and A. Yariv, "Risetime of Pulsed Parametric Oscillators", IEEE J. Quant. Electron. QE-8, pp.433-440(1972).
15. G. D. Boyd and D. A. Kleinman, "Parametric Interaction of Focused Light Beams", J. Appl. Phys. 39, pp. 3597-3639 (1968).
16. R. L. Byer and S. E. Harris, "Power and Bandwidth of Spontaneous Parametric Emission", Phys. Rev. 168, pp. 1064-1068 (1968).
17. J. E. Bjorkholm, "Efficient Optical Parametric Oscillation Using Doubly and Singly Resonant Cavities", Appl. Phys. Lett. 13, pp. 53-56 (1968).
18. J. Falk and J. E. Murray, "Single-Cavity Noncollinear Optical Parametric Oscillation", Appl. Phys. Lett. 14, pp. 245-247 (1969).
19. E. O. Ammann, M. K. Oshman, J. D. Foster, and J. M. Yarborough, "Repetitively Pumped Optical Parametric Oscillator at  $2.13\mu$ ", Appl. Phys. Lett. 15, pp. 131-133 (1969).
20. L. S. Goldberg, "Optical Parametric Oscillation in Lithium Iodate", Appl. Phys. Lett., 17, pp. 489-491 (1970).
21. J. E. Bjorkholm, "Some Effects of Spatially Nonuniform Pumping in Pulsed Optical Parametric Oscillators", IEEE J. Quant. Electron. QE-7, pp. 109-118 (1971).
22. D. A. Kleinman and P. P. Kisliuk, "Discrimination Against Unwanted Orders in the Fabry-Perot Resonator", Bell Syst. Tech. J. 41, pp. 453-462 (1962).
23. L. B. Kreuzer, "Single Mode Oscillation of a Pulsed Singly Resonant Optical Parametric Oscillator", Appl. Phys. Lett. 15, pp. 263-265 (1969).

24. M. V. Hobden and J. Warner, "The Temperature Dependence of the Refractive Indices of Pure Lithium Niobate", *Phys. Lett.*, Vol. 22, pp. 243-244 (1966).
25. J. F. Young, R. B. Miles, S. E. Harris, and R. W. Wallace, "Pump Linewidth Requirement for Optical Parametric Oscillators", *J. Appl. Phys.* 42, pp. 497-498 (1971).
26. J. E. Bjorkholm, "Some Spectral Properties of Doubly and Singly Resonant Pulsed Optical Parametric Oscillators", *Appl. Phys. Lett.* 13, pp. 399-401 (1968).
27. E. O. Ammann, J. M. Yarborough, M. K. Oshman, and P. C. Montgomery, "Efficient Internal Optical Parametric Oscillation", *Appl. Phys. Lett.* 16, pp. 309-312 (1970).

Chapter 5

1.06 $\mu$ -PUMPED OPTICAL PARAMETRIC OSCILLATION

A. Introduction

The first observation of optical parametric oscillation was made by Giordmaine and Miller [1] in 1965. Since that time, great strides have been made\* in improving the output power, efficiency, bandwidth, and tunability of the optical parametric oscillator (OPO). With a few exceptions [3-5], only visible and near ultraviolet sources have been used to pump parametric oscillators, with the ruby laser [6-13] and doubled Nd:YAG laser [14,15] being the most popular. The pulsed OPO has been the most common device, although cw oscillation has been reported using the laser outputs of doubled Nd:YAG (0.532 $\mu$ ) [14] and argon (0.5145 $\mu$ ) [16,17].

This chapter discusses observations of the properties and operating characteristics of a 1.06 $\mu$ -pumped, pulsed LiNbO<sub>3</sub> OPO, operated internal to the pump laser cavity. When possible, the theoretical results of previous chapters are compared to the experimental observations. After a discussion of the design principles used in constructing the oscillator, a technique is presented for predicting the OPO tuning curve using measurements of total fluorescence power. Actual measurements are then presented on two oscillators, one degenerate (tuning around  $\lambda_1 \approx \lambda_2 = 2.12\mu$ ), and one non-degenerate ( $\lambda_1 \approx 1.6\mu$  and

---

\* A review of progress up to mid-1969 and a comprehensive list of references has been given by Harris [2].

$\lambda_2 \approx 3.2\mu$ ). The threshold, output power, bandwidth, stability, and mode spectra are discussed for each oscillator. Evidence of efficient oscillator operation is presented and suggestions for future efforts to improve the performance of this type of oscillator conclude the chapter.

### B. Oscillator Design

The most common and versatile configuration for a parametric oscillator is the "external" oscillator shown in Fig. 5-1(a). The pump laser and the OPO each have separate optical cavities and a lens

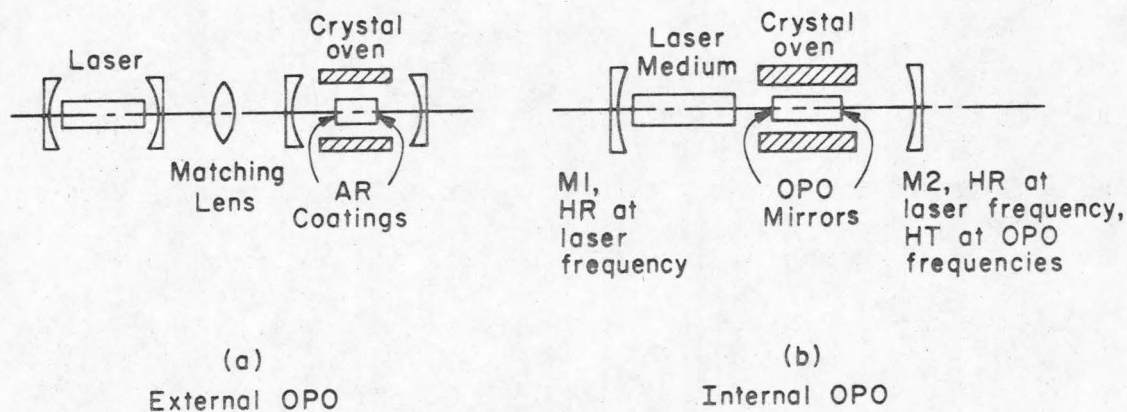


Figure 5-1. Schematic of optical parametric oscillator configurations

is used to mode-match [18-20] the pump into the OPO. This design is particularly convenient when the available pump power far exceeds the oscillator threshold and allows for the use of mode-selecting etalons [11,21] in the OPO to narrow its spectral output. The conversion efficiencies reported for an external OPO have been as high as 67% for

peak pulsed power and 46% for average power [15]. Theoretically, the conversion efficiency can approach 100% for both singly-resonant [22] and doubly-resonant [12,23] oscillators, but no one has yet observed this ideal situation.

An alternate design possibility is shown in Fig. 5-1(b). In the "internal" OPO configuration, the oscillator resonator is placed inside the pump laser cavity to take advantage of the high pump intensities inside the laser. The internal OPO is particularly useful for low-gain, high-threshold OPO systems because of the large available pump intensities and also because both the left- and right-travelling pump waves can drive the oscillator.

When the laser mirrors are both highly reflecting at the pump frequency and highly-transmitting at the OPO frequencies, the internal parametric oscillator acts as a nonlinear output coupler for the laser. Theoretically, it is possible to obtain 100% of the available laser power at the OPO frequencies (see Appendix III) in much the same way that internal second-harmonic generation has been used to achieve optimum laser output coupling [24-26]. E. O. Ammann [27] has recently reported observation of 100% average power conversion efficiency in an internal,  $1.06\mu$ -pumped  $\text{LiNbO}_3$  oscillator.

The simplest form of the internal OPO has the mirrors coated directly on the plane-parallel faces of the nonlinear crystal as shown in Fig. 5-1(b). The OPO cavity is thus automatically aligned and the need for AR coatings is eliminated. Internal OPO systems which use detached mirrors have been demonstrated [17,27,28], but the increased number of components inside the laser increases the insertion loss of

the OPO and decreases the efficiency of the device.

The internal oscillator configuration shown in Fig. 5-1(b) was chosen for the experiments reported here because of its simplicity and because of the low power of the available tungsten-pumped Nd:YAG laser\*. The laser used was the same as the one used for the fluorescence measurements of Chap. 3 and is Q-switched by a mirror rotating at 400 Hz. The stationary laser mirror is highly reflecting at  $1.06\mu$  and highly transmitting from  $1.4\mu$  to  $2.2\mu$  ( $T \gtrsim 90\%$ ). The two nonlinear crystals were cut from a single large  $\text{LiNbO}_3$  crystal with a phase-matching angle of  $50^\circ$  and the crystals were oriented so that the nonlinear coefficients  $d_{15}$  and  $d_{22}$  would add [29]. One of the crystals was also used in the fluorescence measurement shown in Fig. 3-7. The crystal faces were polished flat to  $\lambda/10$  and parallel to within 5 seconds of arc, and the OPO mirrors were coated directly onto those faces. A photograph of the laser and the crystal oven used for tuning the oscillator is shown in Fig. 5-2. A similar OPO system has been reported by Ammann, et al [4,27] and by Falk, et al [5].

### C. Prediction of OPO Tuning Characteristics

When an OPO is operated for the first time, it is very helpful to know in advance the phase-matching angle and crystal temperature which give the desired output frequencies. One variable is thus eliminated from the initial alignment procedure. The most accurate way to predict the tuning characteristics of an OPO is to measure the

---

\*The laser used in these experiments had polarized  $\text{TEM}_{00}$  outputs of 1.0 watt cw and 2.5 kw peak power when Q-switched.

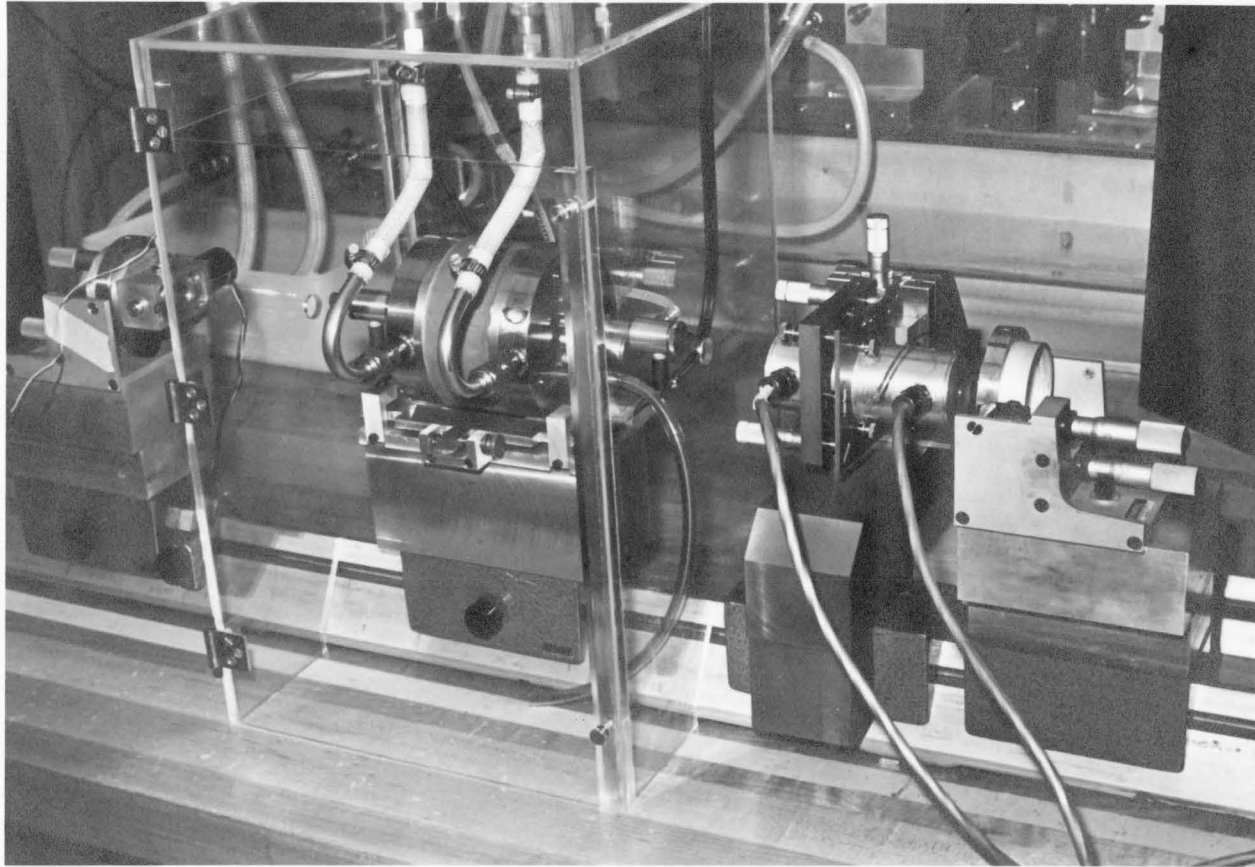


Figure 5-2. Photograph of experimental setup showing Nd:YAG laser and temperature-controlled oven containing parametric oscillator crystal.

collinear fluorescence frequencies as the tuning parameter is varied [30,31]. Unfortunately, such measurements can be time-consuming and are difficult in the infrared. If the indices of refraction are known for a particular crystal, the tuning curve of an OPO using that crystal can be calculated. As pointed out in Chap. 3, however, a problem arises when the refractive indices vary with crystal composition; the exact tuning curve of a particular crystal may not be described by the published values of the indices. The calculated curve can still be useful, however, if the shape of the tuning curve is unchanged by different crystal compositions. A measurement of the total parametric fluorescence power (see Chap. 3) can then be used to fix one point on the calculated

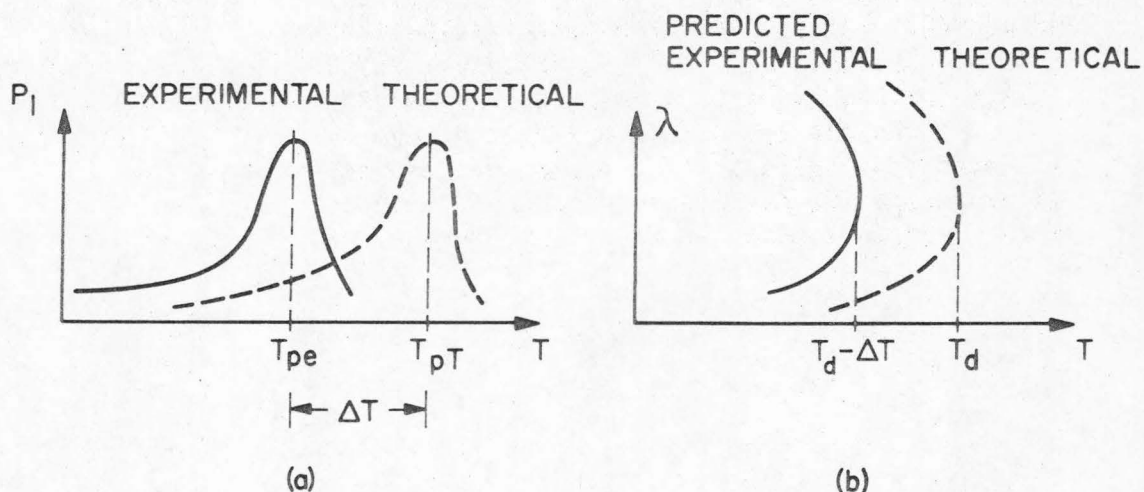


Figure 5-3. Procedure to obtain predicted parametric oscillator tuning curve from total fluorescence power measurement. (a) Experimental and theoretical plots of total fluorescence power versus temperature define the shift  $\Delta T$  between the peaks. (b) Theoretical phase-matched wavelength versus temperature curve is shifted by  $\Delta T$  to obtain the predicted oscillator tuning curve.

tuning curve; the entire tuning curve can thus be predicted [32]. The procedure is illustrated in Fig. 5-3 for the case of temperature tuning. The predicted oscillator tuning curve is shifted along the temperature axis by the amount  $\Delta T$ . The temperature shift  $\Delta T$  is that required to align the peaks of the experimental and theoretical fluorescence curves. The close agreement between theory and experiment in the fluorescence results of Figs. 3-7, 3-8, and 3-14 gives support to the assumption that the shape of the tuning curve is unaffected by composition differences between crystals.

#### D. Experimental Oscillator Tuning Characteristics

Because of pump power limitations, the oscillators reported here were all doubly-resonant. In a doubly-resonant oscillator (DRO) the mirrors must be highly transmitting at the  $1.06\mu$  pump wavelength while remaining highly reflecting at both the signal and idler wavelengths. As a result, the tuning range of the oscillator is limited by the availability of multilayer coatings which can satisfy this three-frequency requirement. At the present state of the art, this requirement can be met only for wavelengths centered about signal and idler wavelengths such that  $\lambda_2/\lambda_1 = 1, 2, \text{ or } 3$ .

For a  $1.06\mu$  pump, the choice of  $\lambda_2/\lambda_1 = 3$  gives  $\lambda_2 = 4.24\mu$ . The possibility of constructing an oscillator which tunes in this region is eliminated by examining the crystal transmission shown in Fig. 5-4 [33]. The absorption in  $\text{LiNbO}_3$  at  $4.24\mu$  is  $0.36 \text{ cm}^{-1}$  which is sufficient to suppress oscillation at this wavelength.

Both of the remaining mirror possibilities give idler wavelengths well within the crystal transparency range and oscillators

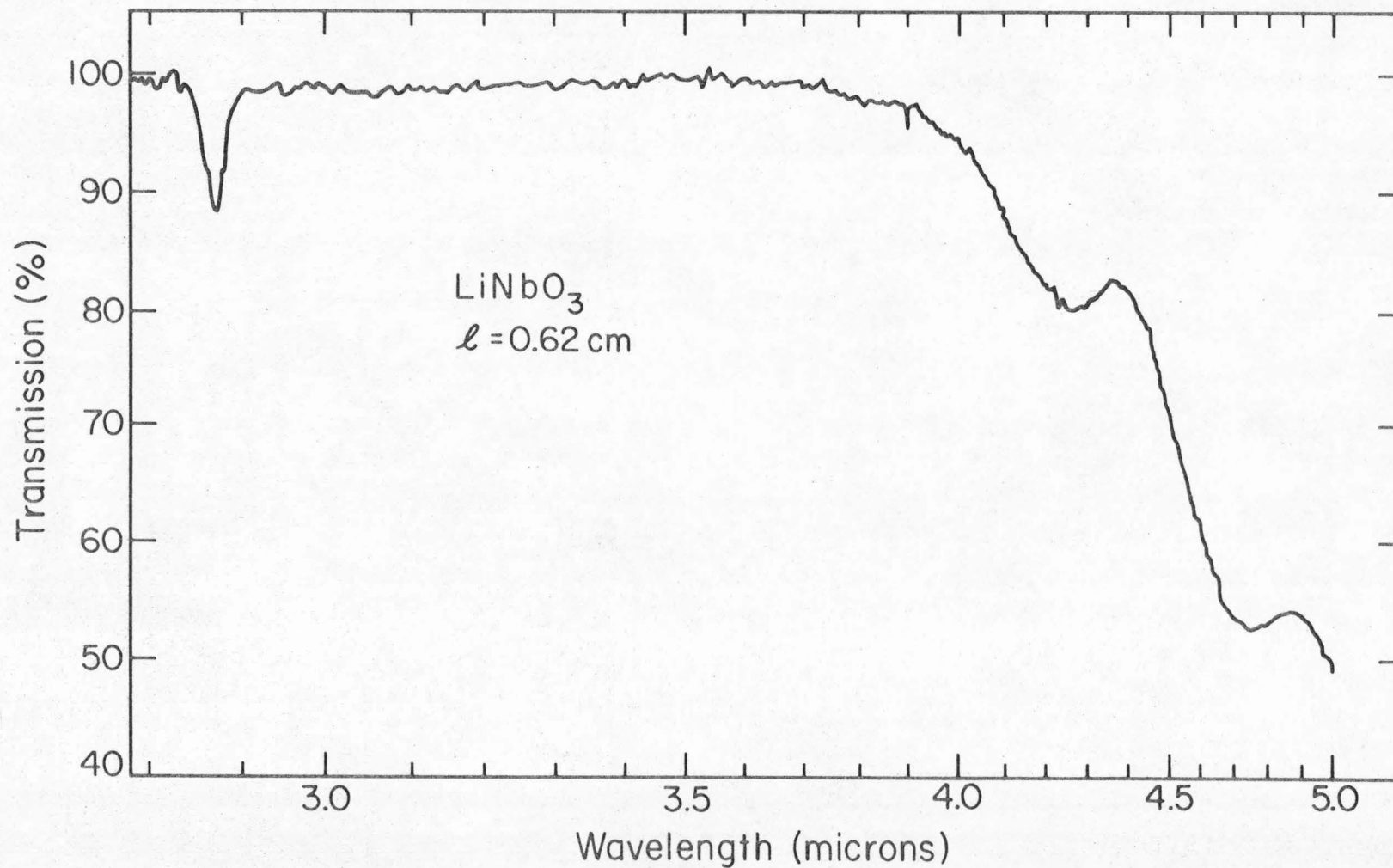


Figure 5-4. Long wavelength absorption edge in LiNbO<sub>3</sub>. The reflection loss at the surfaces has been accounted for so the maximum transmission is 100%.

have been constructed for both cases. The tuning curves for the two oscillators and two different sets of mirrors are shown in Figs. 5-5 and 5-6. Since at each temperature a range of oscillating wavelengths was observed, the data points in the figures indicate the center of the observed range. The solid theoretical curves were found using the technique of the previous section ( $\Delta T = -29.5^\circ\text{C}$ , see Fig. 3-7) and the index data of Ref. 34. The crystal temperatures are the oven readings plus  $0.3^\circ\text{C}$  to account for heating of the crystal by the pump laser. The agreement between the experimental tuning data and the predicted curves is reasonably good with the degenerate point predicted to within  $1.4^\circ\text{C}$ . The observed differences can be attributed to slight differences in crystal alignment and to small differences between the actual refractive indices and those of Ref. 34.

#### E. Oscillator Threshold

From the theory of Boyd and Kleinman [35], the threshold for the two internal  $1.06\mu$ -pumped doubly-resonant oscillators is calculated to be

$$P_{3T} \text{ (watts) } = \begin{cases} 1.02 \times 10^3 \alpha^2 / F(\ell/b) & ; \quad \lambda_1 \approx 2.1\mu \\ 1.3 \times 10^3 \alpha^2 / F(\ell/b) & ; \quad \lambda_1 \approx 1.6\mu \end{cases} \quad (5.1)$$

(one way)

where  $F(\ell/b)$  is a focusing function given in Fig. 12 of Ref. 35,  $\ell$  is the crystal length, and  $b$  is the pump confocal parameter\*. The fractional one-way power loss is  $\alpha$ , assumed equal at  $\omega_1$  and  $\omega_2$ .

---

\*The confocal parameter is  $b = 2\pi\omega_0^2/\lambda$ , where  $\omega_0$  is the minimum Gaussian beam radius.

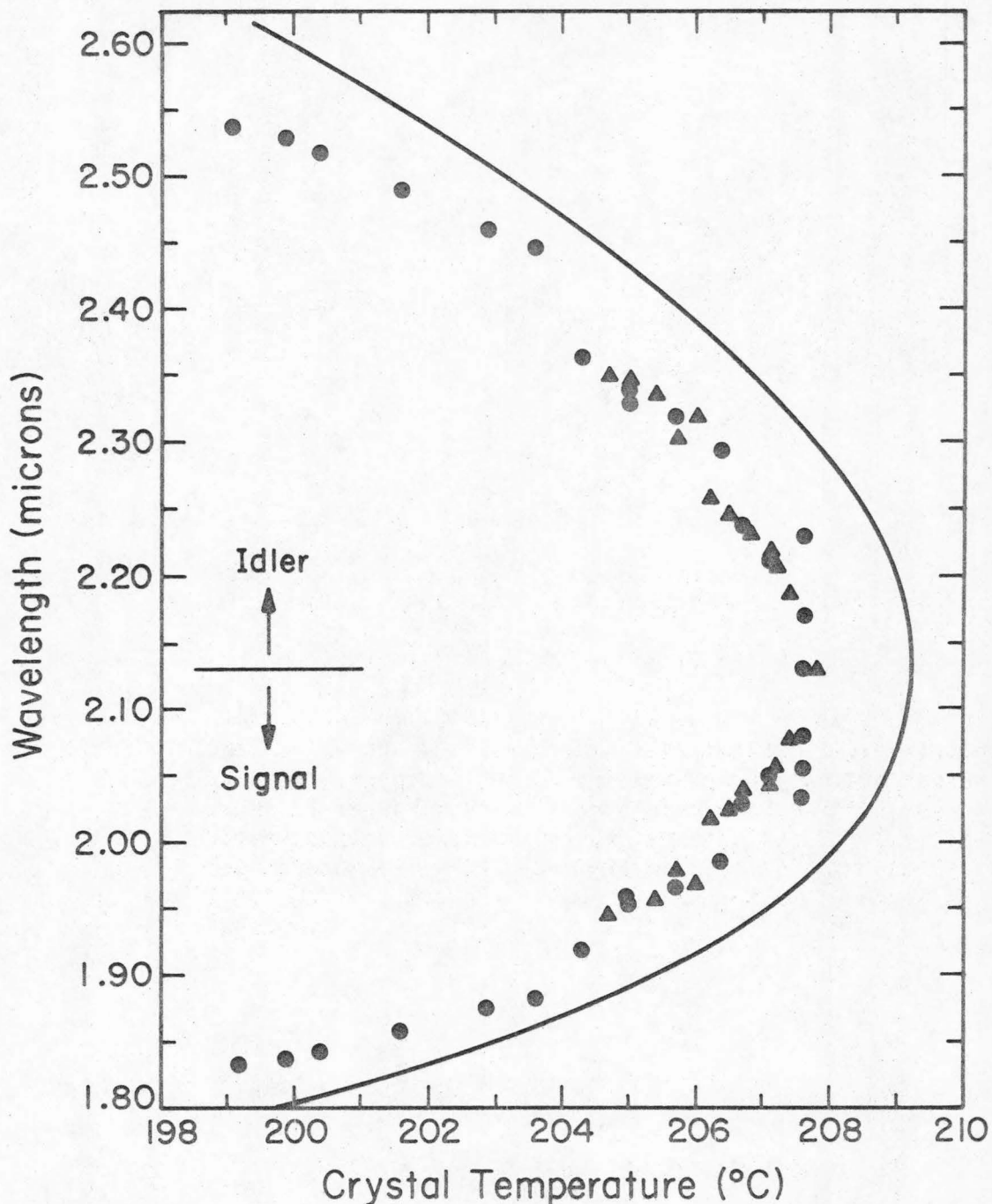


Figure 5-5. Tuning characteristics of two "degenerate" 1.064 $\mu$ -pumped parametric oscillators. The experimental points represent the center of the observed range of oscillating wavelengths. The two different symbols are for two different sets of mirror coatings. The solid curve is found from the data of Ref. 34 using the method discussed in the text.

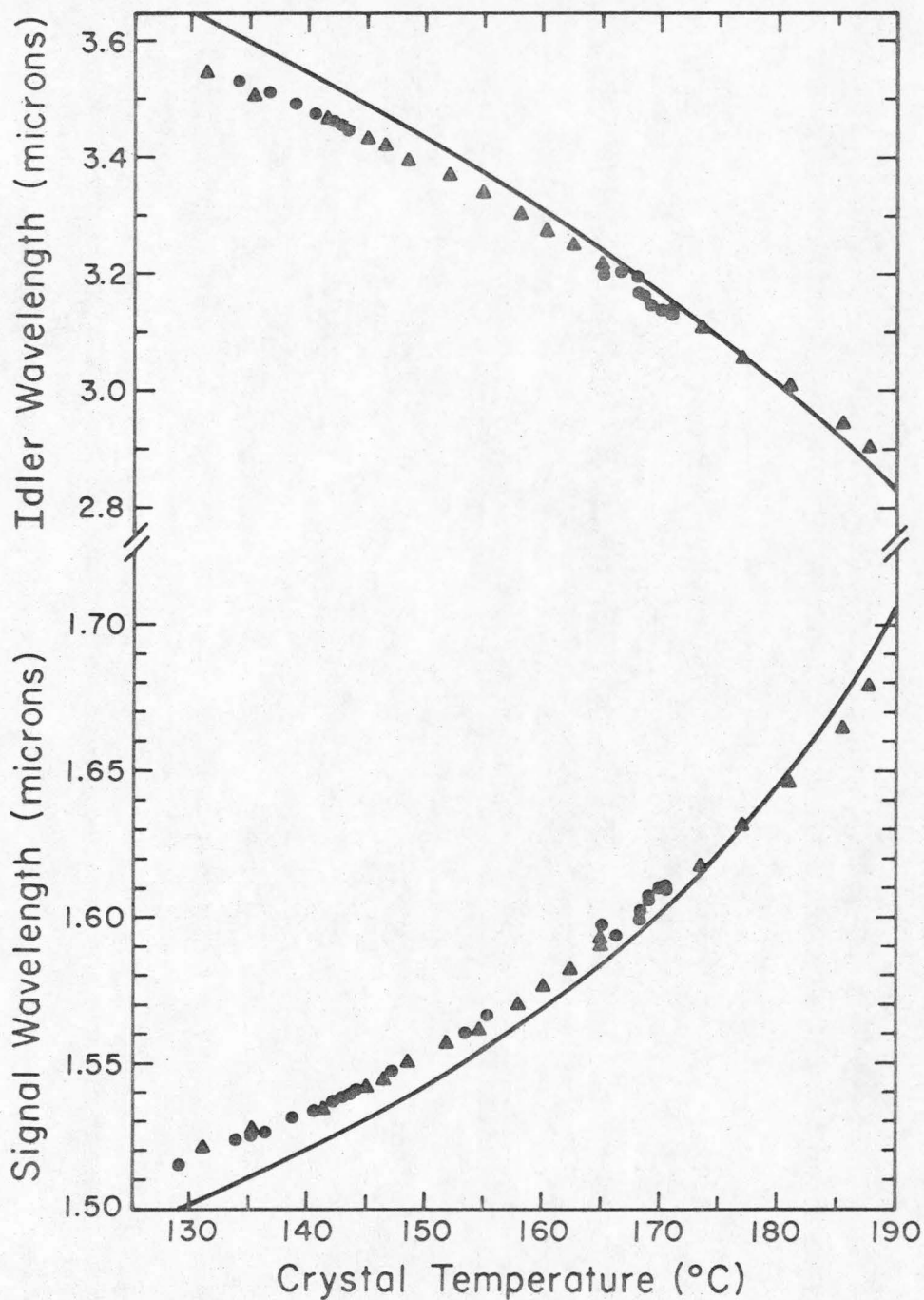


Figure 5-6. Tuning characteristics of two nondegenerate 1.064 $\mu$ -pumped parametric oscillators. The experimental points represent the center of the observed range of oscillating wavelengths. The idler wavelengths were not measured, but were calculated from the observed signal wavelengths. The two different symbols are for two different sets of mirror coatings. The solid curve is found from the data of Ref. 34 using the method discussed in the text.

Although the theory of Ref. 35 assumes that the pump, signal, and idler are Gaussian beams with equal confocal parameters, there is nothing in the flat-flat OPO configuration used here which will force this condition. For  $b \gg \ell$ , however, the pump is nearly collimated with near-planar wave fronts in the crystal, and the OPO transverse mode will be very similar to the  $TEM_{00}$  pump mode. In this case, Eq. (5.1) is expected to give a good estimate of the oscillator threshold.

The one-way power loss  $\alpha$  is difficult to measure when the mirrors are on the crystal surfaces. All of the OPO mirrors had reflectivities greater than 99.5% and the crystal absorption is negligible (see Fig. 5-4). The major source of loss appears to be the surface scattering of the OPO mirrors. This is particularly true since the mirrors damage when put inside the laser, although the amount of additional damage decreases rapidly after 5-10 minutes of operation. Examination of the crystal surfaces after many hours of operation leads to an estimate for  $\alpha$  of  $2.5\% \pm 0.5\%$ .

The laser confocal parameter was measured\* to be 68 cm outside the laser resonator. Correcting for the laser mirror [19] and the nonlinear crystal ( $b(\text{crystal}) = nb(\text{air})$ ) gives  $b \approx 200$  cm for use in Eq. (5.1). The crystal length for both oscillators was  $\ell = 0.56$  cm; the optical length is thus  $L' \approx 1.2$  cm ( $n = 2.19$ ). Since the OPO is pulsed, the predicted threshold must be corrected for the oscillator risetime. With  $L' = 1.2$  cm,  $\alpha = 2.5\%$  and a pulse width  $\tau_p = 130$  nsec, Eq. (4.52) gives  $N_{\min} \approx 1.3$ . Combining all these numbers with Eq. (5.1) gives the approximate expected threshold as

---

\* See Ref. 36 for a method of measuring  $b$ .

$$P_{3T} = \begin{cases} 240 \pm 90 \text{ watts ,} & \lambda_1 \approx 2\mu \\ 300 \pm 100 \text{ watts ,} & \lambda_1 \approx 1.6\mu \end{cases} \quad (5.2)$$

Measurement of the oscillator threshold was accomplished by replacing the stationary highly-reflecting laser mirror with one having a transmission of 1.60% at 1.06 $\mu$ . This change in laser mirror reflectivity had almost no effect on the OPO power, since the non-linear crystal presents a loss to the laser of 3%-6% and thus dominates the total loss at 1.06 $\mu$ . The power into the laser pump lamp was reduced until the OPO would just barely work. The average laser power in the appropriate polarization was then measured and the mirror transmission and pump duty cycle used to calculate the peak laser power inside the cavity. This procedure gave the threshold powers for both oscillators as

$$P_{3T} \approx \begin{cases} 700 \pm 100 \text{ watts, } \lambda_1 \approx 2\mu \\ 450 \pm 100 \text{ watts, } \lambda_1 \approx 1.6\mu \end{cases} \quad (5.3)$$

The agreement between Eqs. (5.2) and (5.3) is reasonable considering the approximate nature of  $\alpha$  and the uncertainties in the experimental measurement.

#### F. Output Power and Efficiency

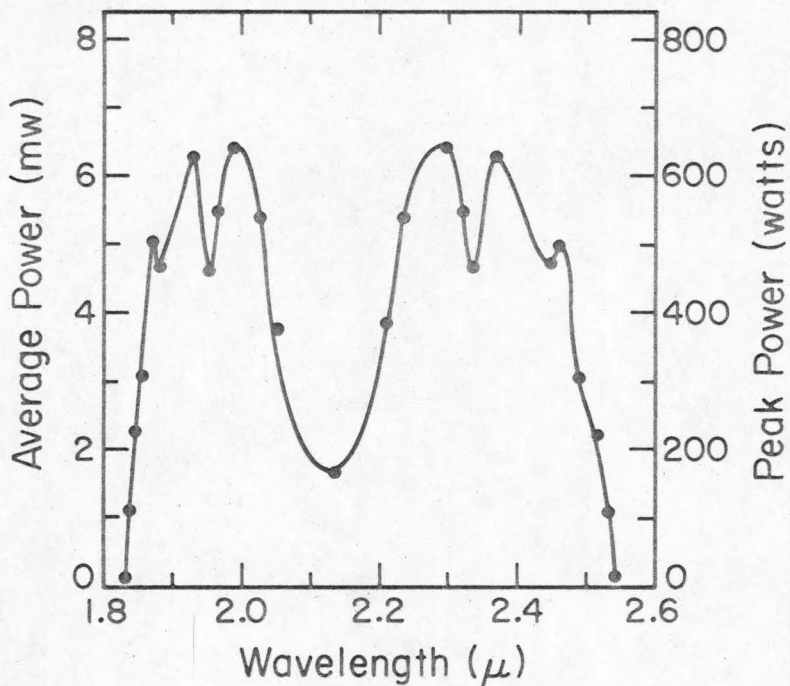
The output power of a parametric oscillator is strongly dependent on the transmission of its mirrors. With all of the mirror sets used, the oscillators appeared to be undercoupled. As a result, the pump was strongly depleted (see time behavior below), but the

oscillator outputs were modest and far below the theoretical 100% efficiency.

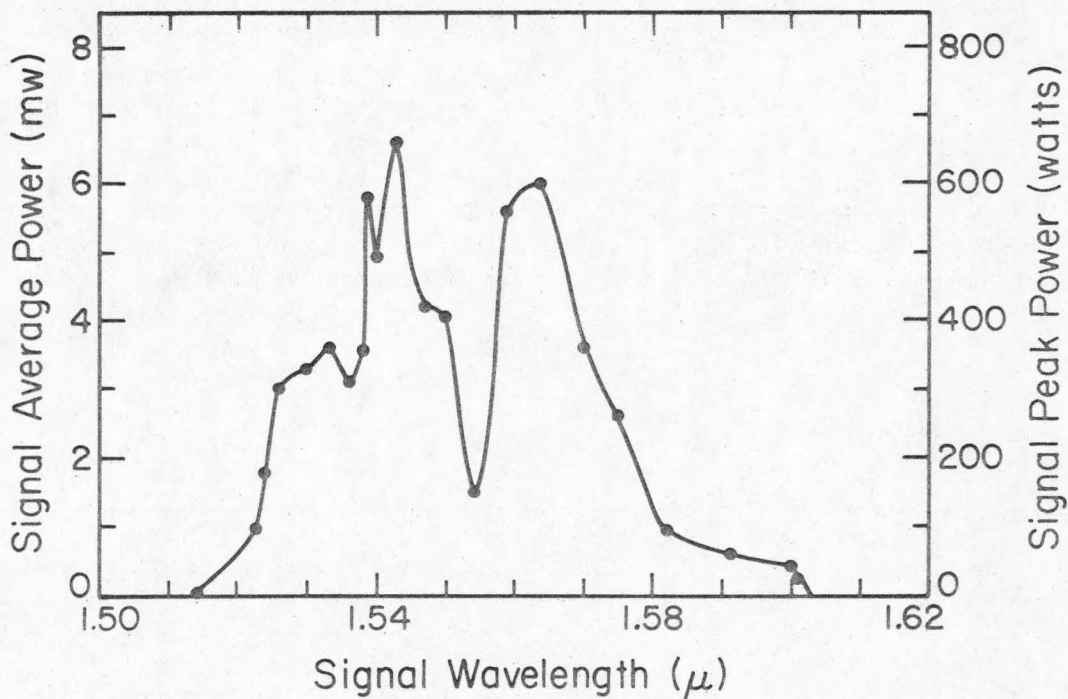
The total average and peak output power as a function of wavelength is shown in Fig. 5-7 for both oscillators. The output of the 2 $\mu$  oscillator at each wavelength shown in Fig. 5-7(a) is the total measured output power divided by 2 (approximately equal amounts of signal and idler power). The 1.6 $\mu$  oscillator power in Fig. 3.7(a) is principally the signal power because the filters used to remove the 1.06 $\mu$  power also block the idler power and because the laser output mirror transmission drops off beyond 2.5 $\mu$ . The idler power would be roughly 1/2 the indicated signal power. The peak power is found by dividing the average power by the duty factor ( $10^{-5}$  for 400 Hz and a 25 nsec pulse). This procedure is not accurate when the oscillator multipulses (see Section H below), but for all the powers shown in Fig. 5-7, roughly 90% of the power is in a single pulse.

The dip in the power of the 2.1 $\mu$  oscillator shown in Fig. 5-7(a) occurs as the oscillator is tuned toward degeneracy; at the minimum, the output wavelengths include the degenerate wavelength. The dip results from the rapid increase of the fluorescence bandwidth as the degenerate condition is approached (see Fig. 3-15). This causes an increase in the number of oscillator modes which compete for the unsaturated pump power. The result is an increase in oscillator threshold by a factor of 2-3 and a corresponding decrease in the oscillator output power.

The power dip shown in Fig. 5-7(b) is not understood, but is probably a result of non-optimum adjustment of the laser and oscillator when the data were taken. A decrease in the transmission of the



(a)



(b)

Figure 5-7. Power output of (a) the degenerate 2.1 $\mu$  oscillator, and (b) the nondegenerate 1.6 $\mu$  oscillator as a function of wavelength.

oscillator Fabry-Perot resonator at  $1.06\mu$  as the crystal temperature was varied would also cause such a dip.

With the OPO in the laser but below any oscillation temperature, the maximum polarized laser output power ( $T = 3.6\%$  mirror) was  $\approx 60$  mw average and 1200 watts peak (400 Hz, 130 nsec pulse). In terms of this available  $1.06\mu$  power, both oscillators had a maximum average power conversion efficiency at each frequency of only 10% but the peak power conversion efficiency was 50%. These efficiencies take into account only the power out one end of the OPO. Since an equal amount of power exits from the other end of the oscillator, the overall efficiencies are twice the above numbers. These efficiencies are comparable to those reported for many pulsed external systems [8,15], but are still far short of the theoretically possible 100% average power efficiency predicted in Appendix III and recently observed by Ammann [27].

#### G. Oscillator Bandwidth and Spectra

The factors which determine the spectral bandwidth of an OPO have been discussed in Chap. 4, Section E. There it was shown that instabilities in the resonator will usually give the largest contribution to the bandwidth. For the oscillator configuration used here, however, mechanical and thermal instabilities should not be important since the cavity length is fixed and the crystal temperature is controlled to better than  $0.1^{\circ}\text{C}$ . The instabilities in the pump frequency and the degree to which steady-state operation is achieved will thus be the limiting factors.

The observed full-width at half-maximum power spectral bandwidths are shown in Fig. 5-8 for both oscillators. As expected from

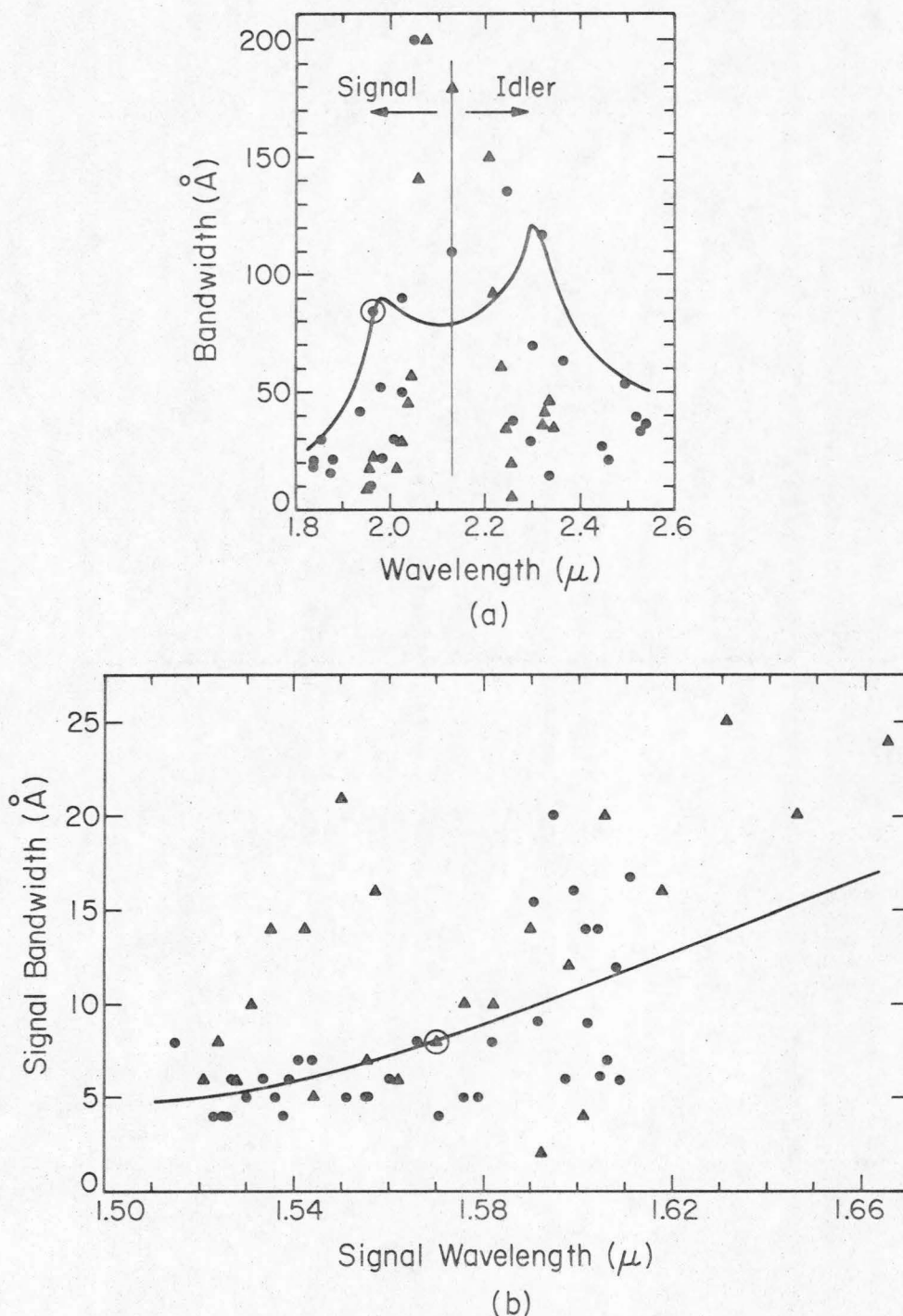


Figure 5-8. Parametric oscillator full-width at half-maximum spectral bandwidth for (a) 2.1μ oscillator, and (b) 1.6μ oscillator. The different symbols are for two different sets of mirror coatings. The solid curves are theoretical (Eq. (3.20)) normalized to the experimental data at the circled points.

the fluorescence theory, the OPO bandwidth increases as degeneracy is approached. The idler bandwidths for the  $1.6\mu$  oscillator could not be measured because of monochromator limitations. The solid-line theoretical curves in Fig. 5-8 were computed from Eq. (3.20) with  $\theta = 0$ . The observed bandwidths were much smaller than the theoretical bandwidths (see Fig. 3-15), so the solid curves in Fig. 5-8 are normalized to the experimental data at the single point indicated by the large circle. This procedure allows the wavelength dependence of the bandwidth to be compared with theory. The agreement of the experimental data with theory in Fig. 5-8 is only qualitative and there is a large amount of scatter in the experimental data.

The measured bandwidths in Fig. 5-8 are only about 1/10 of those predicted by the fluorescence theory. There are two possible explanations for this behavior. First, even though the OPO output pulses are only 25 nsec long (see section H) some degree of steady-state operation may be occurring. The higher threshold modes are thus held below threshold or to lower levels of oscillation. Second, because there is a strong interaction between the OPO and the laser, the pump field may be driven below the threshold level of the lower-gain OPO modes before they have time to turn on. This type of behavior is not a steady-state situation and should not be confused with the near-homogeneous saturation behavior of the true steady-state OPO. Because of the strong pump-depletion behavior of the OPO, the internal OPO can actually act as a "cavity-damping" mechanism for the laser, quickly driving the pump laser field to zero when the OPO oscillates strongly. This type of behavior has been discussed

theoretically by Falk, et al [5].

During the course of these experiments, three different mirror sets were used for both the 2.1 $\mu$  and the 1.6 $\mu$  oscillator. Two of these sets gave nearly identical results although one set of 1.6 $\mu$  mirrors had such high reflectivity that little output power was available from the OPO. The third set of mirrors was used with a less efficient Nd:YAG laser<sup>\*</sup>. In spite of its lower power, this laser produced OPO powers almost as high as the oscillators pumped by the higher power laser. The only observed difference in the OPO operation occurred in the spectra as measured by a monochromator.

Typical monochromator scans for both oscillators are shown in Fig. 5-9. The observed structure corresponds exactly to the  $c/2L'$  longitudinal mode spacing of the OPO resonators. This type of spectra was present in the one pair of oscillators at all output powers and at all oscillation frequencies, but was totally absent from the spectra of the other two pairs of oscillators which were pumped by the more efficient laser. The precise reason for the appearance of the longitudinal mode structure in only one of the three pairs of oscillators is not understood, but it is suspected that the less efficient laser-plus-OPO was single-frequency, while the other laser-OPO combinations had a multi-frequency pump. As noted in Section E of Chap. 4, a multi-frequency pump would tend to "wash out" any OPO mode structure.

---

<sup>\*</sup>This laser had a maximum multi-mode output of 3.8 watts cw compared to 5.5 watts for the laser used in most of the experiments.

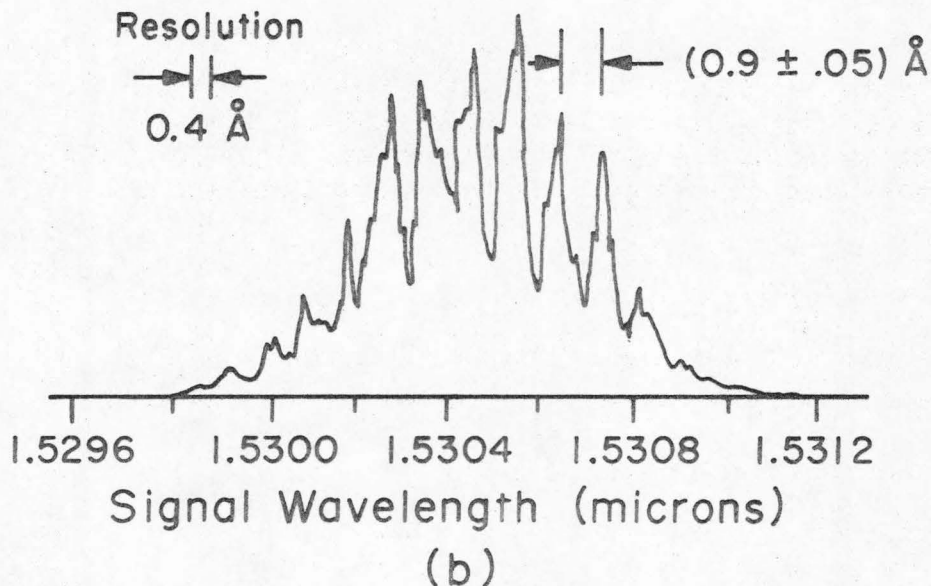
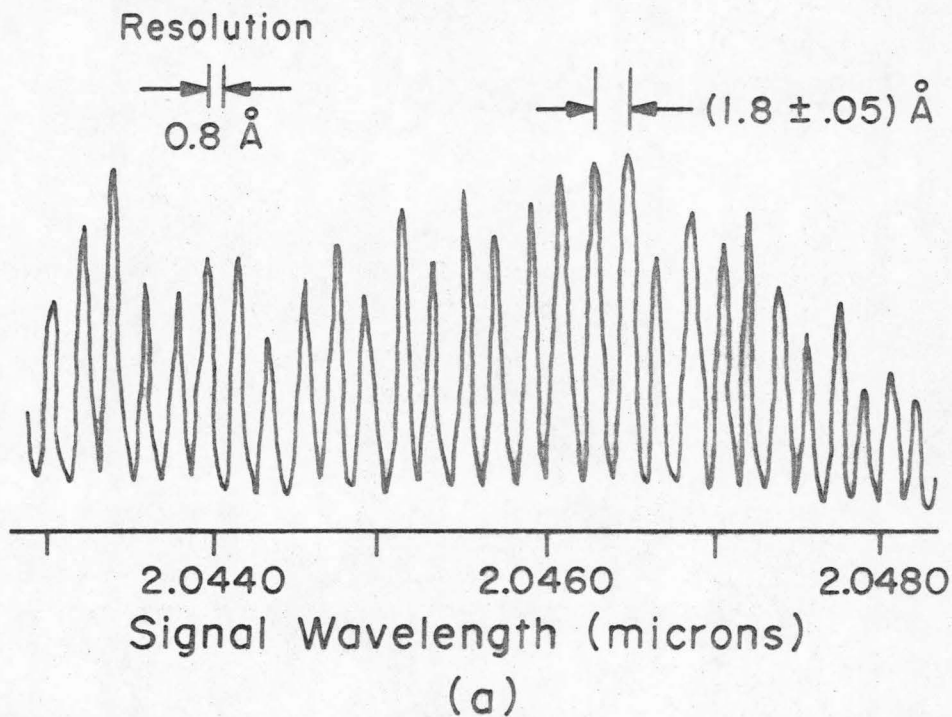


Figure 5-9. Typical monochromator scans for oscillators pumped by less efficient laser. (a)  $2.1\mu$  oscillator. (b)  $1.6\mu$  oscillator. The observed structure corresponds exactly to the longitudinal mode spacing of each oscillator.

## H. Time Behavior

Falk, et al [5] have analyzed the time behavior of the pulsed internal OPO by solving the laser rate equations simultaneously with the OPO equations (Eqs. (2.21)). Their analysis predicts a unique pulsing behavior in which optical energy is alternately exchanged between the laser and parametric optical fields with the stored inversion in the laser medium acting as an energy reservoir. During each high-Q period of the laser, the laser and OPO fields are alternately driven to strong oscillation levels until all of the stored energy in the inverted laser medium is used up. Thus, depending on the laser gain, initial inversion level, and OPO gain and loss, a number of OPO output pulses can occur each time the laser is Q-switched. Up to five such pulses have been reported by the workers in Ref. 5 and by Ammann [27].

For low drive levels, only a single OPO pulse will be observed. This type of behavior for the  $2.1\mu$  oscillator is shown in Fig. 5-10 along with oscilloscope traces of the depleted and non-depleted pump pulses. The response time of the detector-oscilloscope combination was approximately 10 nsec. Although the undepleted pump pulse width is roughly 100 nsec, the OPO pulse width is only 20-25 nsec long, and its peak occurs roughly near the peak of the undepleted pump pulse.

As the laser drive is increased, a second OPO pulse, and then a third pulse appear as available pump power is increased. This type of behavior is illustrated for the  $1.6\mu$  oscillator in Fig. 5-11. Note the "stretching" of the depleted pump pulse from 130 nsec (no

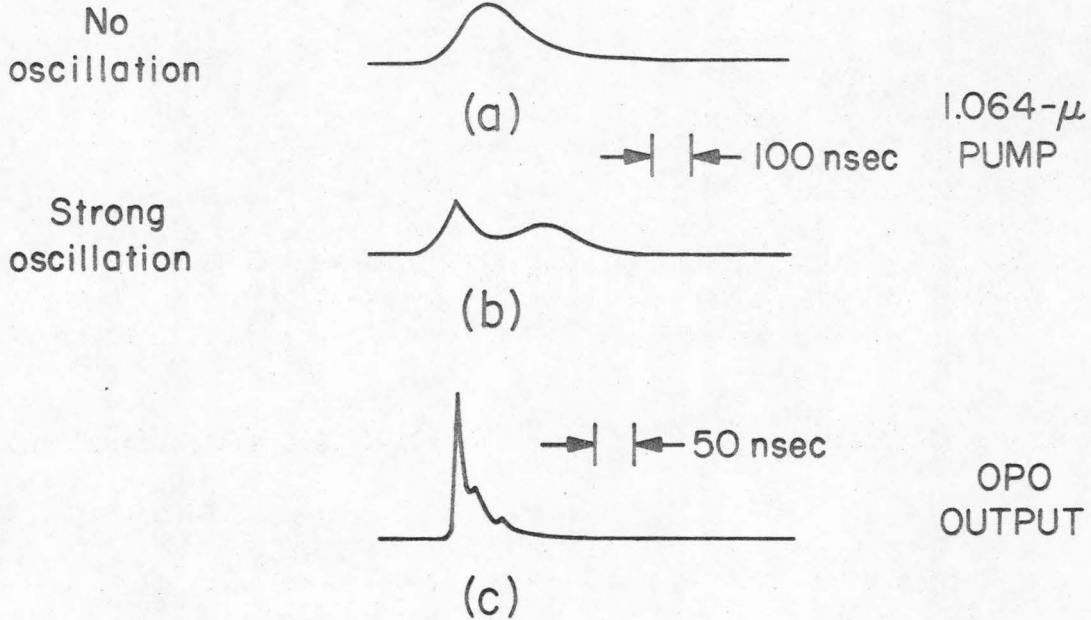


Figure 5-10. Experimental time behavior of the 2.1 oscillator for low pump levels. (a) Nondepleted pump with no parametric oscillation. (b) Pump pulse showing strong depletion when the OPO oscillates. (c) Parametric oscillator output pulse. The vertical scales are different in each picture.

oscillation, see Fig. 5-10(a)) to over 200 nsec as multiple-pulse operation sets in.

As the pump power is increased and multiple-pulsing occurs, the additional OPO power output is almost entirely in the second and third pulses. As the second pulse begins to increase, the first pulse height remains nearly constant, but it will narrow in width [5]. As the pump power is further increased, the second pulse continues to increase in peak power until it has roughly the same peak power and

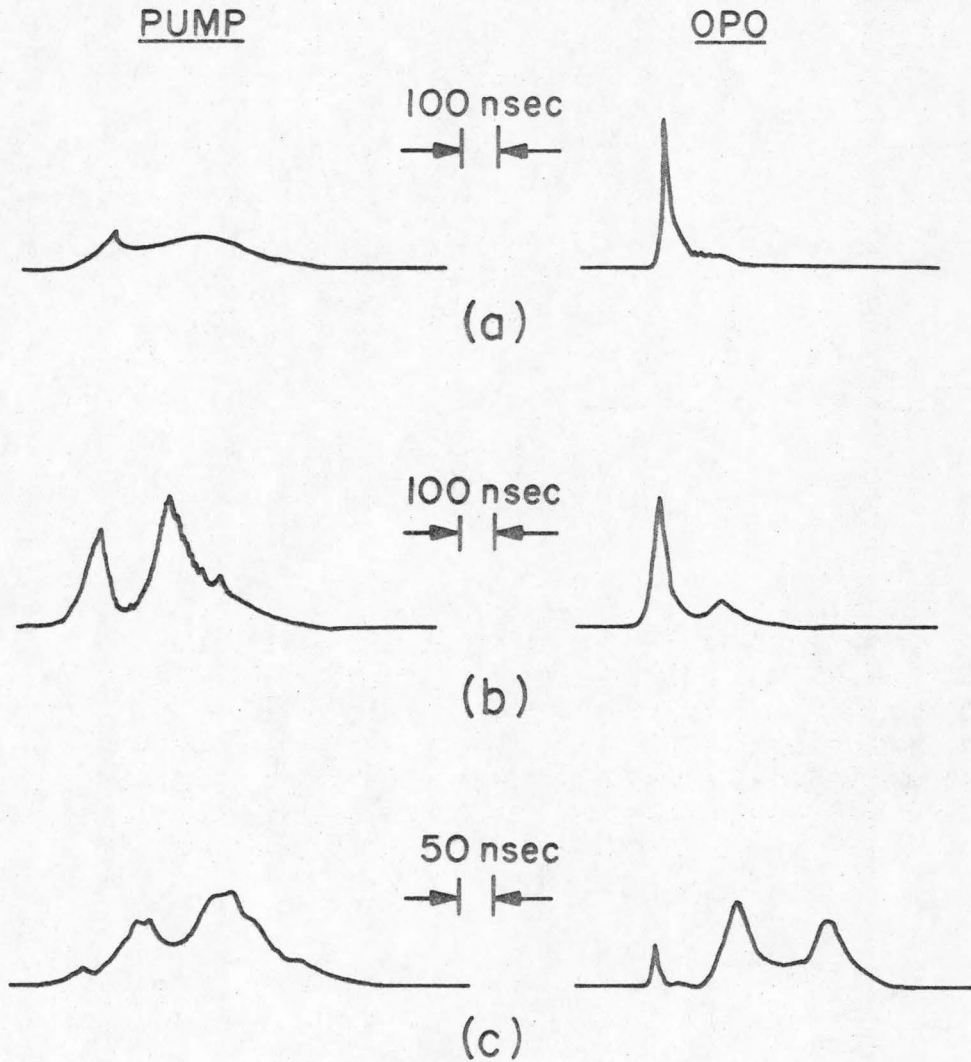


Figure 5-11. Experimentally observed pulse shapes for the  $1.6\mu$  oscillator for various pumping laser drive levels. (a) Low drive levels giving only a single OPO pulse but showing strong pump depletion. (b) Stronger pumping than in (a) with the OPO having two output pulses. (c) Stronger pumping than in (b). The OPO now exhibits three pulses and the pump is strongly depleted on each OPO pulse. The vertical scales in all the figures are arbitrary.

width of the first pulse; the third pulse then appears and the process could continue if additional laser power was available.

The appearance of the multiple-pulsing behavior is evidence of efficient OPO operation; the OPO is pumped so hard that it can "dump" the laser and actually drive the  $1.06\mu$  field to zero [5]. Total average powers as high as 20 mw have been observed in the oscillators reported here and higher powers would be expected with higher-transmitting OPO mirrors.

#### I. Suggestions for Improving Oscillator Performance

Although moderate efficiencies have been obtained from the oscillators reported here, there is certainly room for improvement. Higher pump powers would produce larger OPO outputs and could be conveniently obtained by using cw or pulsed krypton lamps instead of cw tungsten lamps in the single-ellipse pump cavity. Lower loss OPO mirrors would reduce insertion loss of the OPO when it is placed inside the laser resonator. An acoustic Q-switch instead of a rotating mirror would allow the laser inversion to be used more efficiently by providing a long high-Q time when the OPO operates in the multiple-pulse region.

Since the oscillators appear to be quite under-coupled, and since the dominant loss is mirror scatter, the OPO output could be significantly increased by using mirror transmissions in the 1%-3% range. Until the mirror transmission begins to exceed the scattering loss, there will be little effect on oscillator threshold. If sufficient pump power was available, it would also be worthwhile to

investigate the characteristics of a singly-resonant internal OPO and compare them to the DRO behavior observed here.

One final way to improve the operation of the internal OPO is to use a special laser cavity to achieve optimum focusing [35]. There are various ways to do this including modifying the two-mirror laser resonator [37,38] and using a 3-mirror resonator [39,40]. The 3-mirror configuration has the advantage that the optical mode sizes in the laser medium and the nonlinear crystal are independently adjustable so that optimum OPO operation can be obtained (optimum focusing) without affecting the laser gain. To further enhance the improvement due to focusing the laser, curved mirrors could be ground on the nonlinear crystal faces with the radii chosen to match the laser mode beam radii. In this way a degree of mode-matching is achieved and the slight reflectivities of the OPO mirrors at the pump frequency have a minimal effect on laser loss.

Finally, a mode-selecting etalon could be used in the Nd:YAG pump laser to insure single-frequency pump operation. If sufficient pump power was available, the OPO mirrors could be removed from the crystal faces and external mirrors used. In this way an etalon could also be used to mode-select the OPO. Either or both of these methods should reduce the spectral linewidth of the oscillator output.

Chapter 5

References

1. J. A. Giordmaine and R. C. Miller, "Tunable Coherent Parametric Oscillation in  $\text{LiNbO}_3$  at Optical Frequencies", Phys. Rev. 14, pp. 973-976 (1965).
2. S. E. Harris, "Tunable Optical Parametric Oscillators", Proc. IEEE 57, pp. 2096-2113 (1969).
3. E. O. Ammann, M. K. Oshman, J. D. Foster, and J. M. Yarborough, "Repetitively Pumped Optical Parametric Oscillator at  $2.13\mu$ ", Appl. Phys. Lett. 15, pp. 131-133 (1969).
4. E. O. Ammann, J. M. Yarborough, M. K. Oshman, and P. C. Montgomery, "Efficient Internal Optical Parametric Oscillation", Appl. Phys. Lett. 16, pp. 309-312 (1970).
5. J. Falk, J. M. Yarborough, and E. O. Ammann, "Internal Optical Parametric Oscillation", IEEE J. Quant. Electr. QE-7, pp. 359-369 (1971).
6. L. B. Kreuzer, "Ruby-Laser-Pumped Optical Parametric Oscillator with Electro-Optic Effect Tuning", Appl. Phys. Lett. 10, pp. 336-338 (1967).
7. J. E. Bjorkholm, "Efficient Optical Parametric Oscillation Using Doubly and Singly-Resonant Cavities", Appl. Phys. Lett. 13, pp. 53-56 (1968).
8. L. B. Kreuzer, "High-Efficiency Optical Parametric Oscillation and Power Limiting in  $\text{LiNbO}_2$ ", Appl. Phys. Lett. 13, pp. 57-59 (1968).
9. J. E. Bjorkholm, "Some Spectral Properties of Doubly and Singly Resonant Pulsed Optical Parametric Oscillators", Appl. Phys. Lett. 13, pp. 399-401 (1968).
10. J. Falk and J. E. Murray, "Single-Cavity Noncollinear Optical Parametric Oscillation", Appl. Phys. Lett. 14, pp. 245-247 (1969).

11. L. B. Kreuzer, "Single-Mode Oscillation of a Pulsed Singly Resonant Optical Parametric Oscillator", Appl. Phys. Lett. 15 pp. 263-265 (1969).
12. J. E. Bjorkholm, "Some Effects of Spatially Nonuniform Pumping in Pulsed Optical Parametric Oscillators", IEEE J. Quant. Electr. QE-7, pp. 109-118 (1971).
13. L. S. Goldberg, "Optical Parametric Oscillation in Lithium Iodate", Appl. Phys. Lett. 17, pp. 489-491 (1971).
14. R. G. Smith, J. E. Geusic, H. J. Levinstein, J. J. Rubin, S. Singh, and L. G. Van Uitert, "Continuous Optical Parametric Oscillation in  $\text{Ba}_2\text{NaNb}_5\text{O}_{15}$ ", Appl. Phys. Lett. 12, pp. 308-310 (1968).
15. R. W. Wallace, "Stable, Efficient, Optical Parametric Oscillators Pumped with Doubled Nd:YAG", Appl. Phys. Lett. 17, pp. 497-499 (1970).
16. R. L. Byer, M. K. Oshman, J. F. Young, and S. E. Harris, "Visible cw Parametric Oscillator", Appl. Phys. Lett. 13, pp. 109-111 (1968).
17. R. G. Smith and J. V. Parker, "Experimental Observation of and Comments on Optical Parametric Oscillation Internal to the Laser Cavity", J. Appl. Phys. 41, pp. 3401-3408 (1970).
18. H. Kogelnik, "Imaging of Optical Modes--Resonators with Internal Lenses", Bell Syst. Tech. J. 44, pp. 455-494 (1965).
19. H. Kogelnik and T. Li, "Laser Beams and Resonators", Proc. IEEE 54, pp. 1312-1329 (1966).
20. B. E. Francois, F. M. Libreht, and J. J. Engelen, "Mode Matching with a Single Thin Lens", Appl. Opt. 10, pp. 1157-1159 (1971).
21. D. A. Kleinman and P. P. Kisliuk, "Discrimination against Unwanted Orders in the Fabry-Perot Resonator", Bell Syst. Tech. J. 41, pp. 453-462 (1962).

22. L. B. Kreuzer, "Single and Multi-Mode Oscillation of the Singly-Resonant Optical Parametric Oscillator," Proc. Joint Conf. Lasers and Opto-Electronics (Univ. of Southampton, I.E.R.E., London), pp. 52-63 (1969).
23. J. E. Bjorkholm, "Analysis of the Doubly Resonant Optical Parametric Oscillator without Power-Dependent Reflections", IEEE J. Quant. Electr. QE-5, pp. 293-295 (1969).
24. J. E. Geusic, H. J. Levinstein, S. Singh, R. G. Smith, and L. G. Van Uitert, "Continuous 0.532 $\mu$  Solid-State Source Using Ba<sub>2</sub>NaNb<sub>5</sub>O<sub>15</sub>", Appl. Phys. Lett. 12, pp. 306-308 (1968).
25. R. G. Smith, "Theory of Intracavity Optical Second-Harmonic Generation", IEEE J. Quant. Electr. QE-6, pp. 215-223 (1970).
26. A. Stein and R. A. Kaplan, "One-Watt Average Second Harmonic Power with a Repetitively Q-Switched Nd:YAG Laser", Appl. Phys. Lett. 16, pp. 338-341 (1970).
27. E. O. Ammann, "3- to 5-Micron Parametric Oscillator", GTE Sylvania Inc., Mountain View, Calif. 94040, Report No. AFAL-TR-72-13, January 1972.
28. L. S. Goldberg, "Repetitively-Pulsed LiIO<sub>3</sub> Internal Optical Parametric Oscillator", presented at the VII International Quantum Electronics Conference, May 1972.
29. J. E. Bjorkholm, "Relative Signs of the Optical Nonlinear Coefficients  $d_{31}$  and  $d_{22}$  in LiNgO<sub>3</sub>", Appl. Phys. Lett. 13, pp. 36-37 (1968).
30. S. E. Harris, M. K. Oshman, and R. L. Byer, "Observation of Tunable Optical Parametric Fluorescence", Phys. Rev. Lett. 18, pp. 732-734 (1967).
31. C. Laurence and F. Tittel, "Prediction of the Tuning Characteristics of an Optical Parametric Oscillator Using Parametric Fluorescence", Opto-Electr. 3, pp. 1-4 (1971).

32. J. E. Pearson, U. Ganiel, and A. Yariv, "Parametric Oscillator Tuning Curve from Observations of Total Parametric Fluorescence", *IEEE J. Quant. Electr.* QE-8, pp. 383-385 (1972).
33. The author is grateful to Bernie Soffer of the Hughes Research Laboratories, Malibu, California for measuring the transmission curve.
34. M. V. Hobden and J. Warner, "The Temperature Dependence of the Indices of Refraction of Pure Lithium Niobate", *Phys. Lett.* 22, pp. 243-244 (1966).
35. G. D. Boyd and D. A. Kleinman, "Parametric Interaction of Focused Gaussian Light Beams", *J. Appl. Phys.* 39, pp. 3597-3639 (1968).
36. J. E. Pearson, T. C. McGill, S. Kurtin, and A. Yariv, "Diffraction of Gaussian Beams by a Semi-Infinite Plane", *J. Opt. Soc. Am.* 59, pp. 1440-1445 (1969).
37. R. B. Chesler and D. Maydan, "Convex-Concave Resonators for  $TEM_{00}$  Operation of Solid State Ion Lasers", unpublished.
38. R. B. Chesler and D. Maydan, "Short, Efficient, and Stable Nd:YAlG Laser Cavities Using Imaged Mirrors", presented at Conf. on Laser Engineering and Appl., Washington, D.C., June 1971.
39. D. Maydan and R. B. Chesler, "Q-Switching and Cavity Dumping of Nd:YAlG Lasers", *J. Appl. Phys.* 42, pp. 1031-1034 (1971).
40. H. W. Kogelnik, E. P. Ippen, A. Dienes, and C. V. Shank, "Astigmatically Compensated Cavities for cw Dye Lasers," *IEEE J. Quant. Electr.* QE-8, pp. 373-379 (1972).

Chapter 6

CONCLUSION

The theoretical and experimental aspects of optical parametric fluorescence and oscillation have been discussed in detail. The non-linear interaction equations were derived in a general form which exhibited both the spatial and temporal dependence of the fields. The role of index mismatch and of the relative phase of the interacting waves was also explicitly shown. A steady-state nondepleted-pump solution of these equations gave the outputs of a low-gain parametric amplifier in terms of its inputs. Maximization of the amplifier output power gave an optimum value for the relative phase of the three waves.

The theory of parametric fluorescence was reviewed by considering the fluorescence as the output of a parametric amplifier whose inputs are the zero-point vibrations of the electromagnetic field. The total fluorescence power emitted from a nonlinear crystal was studied using a  $1.06\mu$  pump laser; comparison with theory gave good agreement. Infrared-pumped, narrow-bandwidth fluorescence was studied with a monochromator and again the experimental data on power, bandwidth, and tuning agreed well with theory. These observations constitute the first measurement of parametric fluorescence in the infrared.

Several parameters of parametric oscillators were discussed theoretically. The threshold behavior in a near-field approximation (loose-focusing) was found by studying a parametric amplifier inside a Fabry-Perot resonator. The analysis allowed the oscillation frequencies and the oscillator threshold to be calculated as a function of

mirror reflectivities, cavity roundtrip phase changes, and wave vector mismatch. The oscillator bandwidth and stability near threshold were also examined using the results of the Fabry-Perot analysis. It was concluded that a parametric oscillator would operate very near the passive Fabry-Perot resonances even when  $\Delta k \neq 0$ . The analysis also showed that mechanical and thermal instabilities would make the largest contribution to the bandwidth of a steady-state parametric oscillator, although the output of a perfectly-stabilized parametric oscillator should be single frequency and homogeneously saturated. Using a time-dependent analysis, the risetime of a pulsed parametric oscillator was calculated. The results showed that the observed threshold of a pulsed oscillator could be greatly increased over the "cw" threshold depending on the cavity optical length and the pump pulse width.

The experimental properties of infrared-pumped parametric oscillators were studied using a pulsed,  $1.06\mu$ -pumped,  $\text{LiNbO}_3$  oscillator. Because of threshold considerations and because of its simplicity, the oscillator was operated internal to the laser cavity. In this way, the parametric oscillator acted as a nonlinear output coupler for the laser. A method was presented for predicting the tuning curve of parametric oscillators using a measurement of total fluorescence power. The technique accurately predicted the tuning curves of two oscillators (one degenerate and one nondegenerate). The two oscillators provided wavelength tuning which was nearly continuous from  $1.51\mu$  to  $3.55\mu$ .

With thresholds on the order of 450 watts, both oscillators had average power outputs of 6 mw and peak powers of 600 watts. In terms of the available  $1.06\mu$  power, these powers correspond to conversion efficiencies of 10% and 50%, respectively. These efficiencies are comparable to the highest observed for visible-pumped oscillator systems. The nondegenerate oscillator (wavelength outputs around  $1.6\mu$  and  $3.2\mu$ ) had bandwidths of 5 to 15 angstroms ( $1.9-5.9 \text{ cm}^{-1}$ ) and the degenerate oscillator bandwidths ranged from 20 to  $180\text{\AA}$  ( $4.5 - 41 \text{ cm}^{-1}$ ). Both oscillators showed the theoretically predicted increase in bandwidth closer to degeneracy. Distinct longitudinal mode spectra were observed for the first time and were attributed to the accident of a single-frequency pump laser. Several suggestions were made for improving this type of parametric oscillator.

These studies have provided useful insights into the design and operation of optical parametric oscillators. The present level of the theory, however, allows the various parameters such as threshold and bandwidth to be predicted only qualitatively. Further refinements in the theory must include pump depletion and account for non-steady state operation where saturation effects do not dominate the behavior of the oscillator.

Much experimental work remains to be done in the area of optimum oscillator output coupling and in the design of laser-plus-oscillator resonators for internal parametric oscillators. Efforts to achieve efficient operation of a singly-resonant internal oscillator should also be undertaken. An efficient singly-resonant oscillator could provide high output powers along with narrow linewidths even

when using a multi-frequency pump. Singly-resonant operation would also reduce the difficulties of obtaining broadband multilayer mirror coatings.

When many of the remaining practical problems of parametric oscillators are solved, the devices will provide high brightness, coherent, narrow bandwidth, tunable radiation. Such a light source will have numerous applications in both industrial and scientific areas.

Appendix I

Effective Nonlinear Coefficients

During the derivation of the interaction equations in Chapter 2, an effective nonlinear coefficient for three-wave parametric interactions was defined in Eq. (2.12) as

$$d = d_{ijk} e_i^1 e_j^2 e_k^3 \quad (2.12)$$

A similar definition has also been given by Boyd and Kleinman [1]. In order to evaluate  $d$  for a given crystal class, the polarization directions of the three modes must be chosen. In uniaxial crystals phase-matching can be achieved by choosing one or two of the three waves as "ordinary-polarized" and the remaining waves as "extraordinary-polarized" [2]; each choice defines a different "type" of phase matching, depending on the sign of the crystal birefringence.

Following the type-definitions of Midwinter and Warner [3], the two types of phase-matching are defined by the number of extraordinary waves:

A. Negative uniaxial crystals ( $n^e < n^o$ )

$$\begin{aligned} \text{Type 1: } \quad \omega_3^e &\rightarrow \omega_1^o + \omega_2^o & \text{SHG: } \quad 2\omega_1^o &\rightarrow \omega_2^e \\ \\ \text{Type 2: } \quad \omega_3^e &\rightarrow \omega_1^o + \omega_2^e & & \\ & \text{or} & \text{SHG: } \quad \omega_1^o + \omega_1^e &\rightarrow \omega_2^e \\ & \omega_3^e &\rightarrow \omega_1^e + \omega_2^o & \end{aligned} \quad (I.1)$$

B. Positive uniaxial crystals ( $n^e > n^o$ )

Type 1:  $\omega_3^o \rightarrow \omega_1^o + \omega_2^e$

or

$\omega_3^o \rightarrow \omega_1^e + \omega_2^o$

SHG:  $\omega_1^e + \omega_1^o \rightarrow \omega_2^o$

(I.2)

Type 2:  $\omega_3^o \rightarrow \omega_1^e + \omega_2^e$

SHG:  $2\omega_1^e \rightarrow \omega_2^o$

The superscripts "e" and "o" refer to extraordinary and ordinary polarizations and the subscripts on the radian frequencies refer to the pump, signal, and idler waves as defined in Chapter 2. For completeness, the polarizations for second harmonic generation (SHG) are also shown. As noted in Ref. 3, Type 1 matching for negative uniaxial crystals gives the same form for  $d$  as Type 2 matching in positive crystals of the same crystal class, and vice-versa.

The geometry used for calculating  $d$  is shown in Fig. I-1. All three waves are assumed to propagate in the direction defined by  $\vec{k}$ . The phase-matching angle,  $\theta_m$ , is the angle between  $\vec{k}$  and the crystal z(optic)-axis. The double-refraction angle,  $\rho$ , is the angle between  $\vec{D}$  and  $\vec{E}$  and is found from

$$\tan \rho = \frac{1}{2} n_e^2(\theta_m) \left( \frac{1}{n_e^2} - \frac{1}{n_o^2} \right) \sin 2\theta_m \quad (1.3)$$

where

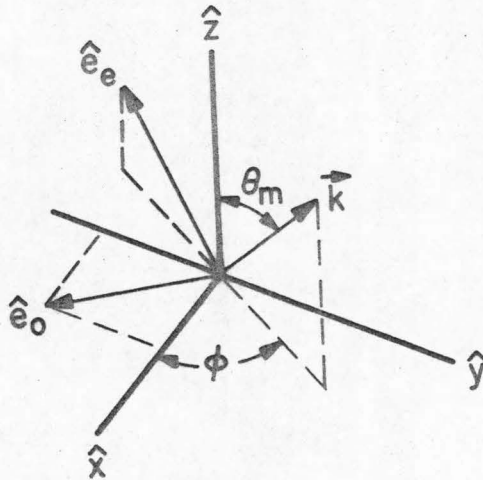


Figure I-1. Geometry for calculating effective nonlinear coefficients. The crystalline axes are defined by  $\hat{x}$ ,  $\hat{y}$ , and  $\hat{z}$ . The electric field polarization directions are  $\hat{e}_o$  for an ordinary wave and  $\hat{e}_e$  for an extraordinary wave. The phase matching angle is  $\theta_m$  and  $\phi$  is the azimuthal angle measured from the crystal x-axis.

$$\frac{1}{n_e^2(\theta)} = \frac{\cos^2\theta}{n_o^2} + \frac{\sin^2\theta}{n_e^2} \quad (I.4)$$

The indices of refraction in Eq. (I.4) are evaluated at the frequency of the extraordinary wave. Note that  $\rho > 0$  for negative uniaxial crystals ( $n_e < n_o$ ) and  $\rho < 0$  for positive crystals.

The azimuthal angle  $\phi$  is the angle between the crystal x-axis and the projection of  $\vec{k}$  on the xy plane. With this geometry the electric field polarization directions for ordinary and extraordinary waves are

$$\hat{e}_o = \sin\phi \hat{e}_x - \cos\phi \hat{e}_y \quad (\text{I.5})$$

$$\hat{e}_e = -\cos\theta(\cos\phi\hat{e}_x + \sin\phi\hat{e}_y) + \sin\theta \hat{e}_z .$$

All vectors  $\hat{e}_j$  in Eq. (I.5) have a magnitude of unity and  $\theta = \theta_m + \rho$ .

By using Eq. (I.5) in Eq. (2.12), the effective nonlinear coefficients for a number of commonly used crystals have been calculated. Whenever there are two extraordinary fields and  $\theta_m \neq 90^\circ$ , the slight difference between the values of  $\rho$  at the two frequencies has been neglected. The results are shown in Table I-1 along with optimum values for  $\phi$  and measured values of the nonzero nonlinear coefficients. Since these values were measured by second-harmonic generation techniques, the effective nonlinear coefficient for SHG is one-half that given in Table I-1 for a 3-wave interaction [1].

To illustrate the procedure for calculating  $d$ , consider Type 1 matching in KDP. The only nonzero coefficients are  $d_{14} = d_{25} = d_{36}$  in the contracted notation of Ref. 17. The equality between the three coefficients is a result of Kleinman's symmetry condition [18]. Equation (2.12) can also be written as

$$d = \hat{e}_1 \cdot \tilde{\alpha} : \hat{e}_2 \hat{e}_3 \quad (\text{I.6})$$

where  $\hat{e}_j$  is the unit vector in the polarization direction of the  $\omega_j$  field. Equation (2.7) allows Eq. (I.6) to be written as

$$d = \hat{e}_1 \cdot \vec{P}_{NL}(\omega_1) \quad (\text{I.7})$$

where  $\vec{P}_{NL}(\omega_1)$  has unity magnitude. Because of the Kleinman condition [18],  $d$  could also be expressed in terms of the polarizations at  $\omega_2$  or  $\omega_3$ . The nonlinear polarization at  $\omega_1$  can be written as

$$\vec{P}_{NL}(\omega_1) = P_x \hat{e}_x + P_y \hat{e}_y + P_z \hat{e}_z \quad (I.8)$$

where [17]

$$\begin{aligned} P_x &= 2d_{14} E_y E_z \\ P_y &= 2d_{14} E_x E_z \\ P_z &= 2d_{14} E_x E_y \end{aligned} \quad (I.9)$$

For Type 1 matching, only the  $\omega_3$  field is extraordinary, so

$\hat{e}_1 = \hat{e}_2 = \hat{e}_o$  and  $\hat{e}_3 = \hat{e}_e$ . The field components in (I.9) are the total field so, for example,  $E_y = E_y(\omega_1) + E_y(\omega_2) + E_y(\omega_3)$  or

$$E_y = 2(\hat{e}_o)_y + (\hat{e}_e)_y = -2\cos\phi - \sin\phi\cos\theta_m \quad (I.10)$$

for Type 1 matching. In a similar manner,

$$E_x = 2\sin\phi - \cos\phi\cos\theta_m \quad (I.11)$$

Combining Eqs. (I.5), (I.7), (I.8), (I.10), and (I.11) gives the final result

$$d = -2d_{14} \sin\theta \sin 2\phi \quad (I.12)$$

TABLE I-1. EFFECTIVE NONLINEAR COEFFICIENTS

Crystal	Class	$n_e - n_o$	$d(\text{Type 1}) \theta = \theta_m + \rho$	$d(\text{Type 2}) \theta = \theta_m + \rho$	$d_{ij}^* \left( \begin{array}{l} 10^{-9} \text{esu, or} \\ 1/27 \times 10^{-22} \text{mks} \end{array} \right)$	[Ref.]
KDP, RDP, ADP, RDA	Tetragonal 42m	(-)	$-2d_{14} \sin \theta, \sin 2\phi$ $\phi_{\text{opt}} = \pi/4$	$2d_{14} \sin 2\theta \cos 2\phi$ $\phi_{\text{opt}} = 0, \pi/2$	$d_{14} = 1.26$ (ADP) $= 1.04$ (others)	[4-6]
LiNbO <sub>3</sub>	Trigonal 3m	(-)	$2d_{15} \sin \theta - 2d_{22} \cos \theta \sin 3\phi$ $\phi_{\text{opt}} = \pi/2$	$2d_{22} \cos^2 \theta \cos 3\phi$ $\phi_{\text{opt}} = 0, \pi/2$	$d_{15} = 13.0 \pm .6$ $d_{22} = -6.2 \pm 1$ $d_{33} = 90 \pm 22$	[4] [7-9] [4,9,10]
LiIO <sub>3</sub>	Hexagonal 6	(-)	$2d_{15} \sin \theta, \phi$ arbitrary	0	$d_{15} = 13.2 \pm .6$	[4,6,11]
Ba <sub>2</sub> NaNb <sub>5</sub> O <sub>15</sub>	Ortho- rhombic mm2	(-) (slightly biaxial)	$2 \sin \theta (d_{15} \sin^2 \phi + d_{24} \cos^2 \phi)$ $\phi_{\text{opt}} = \pi/2$	$(d_{24} - d_{15}) \sin 2\theta$ $\times \sin 2\phi$ $\phi_{\text{opt}} = \pi/4$	$d_{15} = 48 \pm 2.4$ $d_{24} = 46 \pm 2.6$ $d_{33} = 66 \pm 4.8$	[10,12]
Ag <sub>3</sub> AsS <sub>3</sub>	Trigonal 3m	(-)	$2d_{15} \sin \theta - 2d_{22} \cos \theta \sin 3\phi$ $\phi_{\text{opt}} = \pi/2$	$2d_{22} \cos^2 \theta \cos 3\phi$ $\phi_{\text{opt}} = 0, \pi/2$	$d_{15} = 39 \pm 8$ $d_{22} = 62 \pm 8$	[10,13,14]
CdSe	Hexagonal 6mm	(+)	0	$2d_{15} \sin \theta$ $\phi$ arbitrary	$d_{15} = 74 \pm 18$ $d_{31} = 68 \pm 15$ $d_{33} = 130 \pm 30$	[15,16]

\* The contracted notation defined in Ref. 17 is used; see Ref. 10 for a comprehensive listing of measured values of  $d_{ij}$ .

APPENDIX I

References

1. G. D. Boyd and D. A. Kleinman, "Parametric Interaction of Focused Light Beams", *J. Appl. Phys.* 39, pp. 3597-3639 (1968).
2. J. A. Giordmaine and R. C. Miller, "Optical Parametric Oscillation in  $\text{LiNbO}_3$ " in Physics of Quantum Electronics, P. O. Kelley, B. Lax, and P. E. Tannenwald, Eds. (McGraw-Hill Book Co., New York, 1966), pp. 31-42.
3. J. E. Midwinter and J. Warner, "The Effects of Phase-Matching Method and of Uniaxial Crystal Symmetry on the Polar Distribution of Second Order Nonlinear Optical Polarization", *Brit. J. Appl. Phys.* 16, pp. 1135-1142 (1965).
4. B. F. Levine and C. G. Bethea, "Nonlinear Susceptibility of GaP; Relative Measurement and Use of Measured Values to Determine a Better Absolute Value", *Appl. Phys. Lett.* 20, pp. 272-275(1972).
5. V. S. Suvorov, A. S. Sonin, and I. S. Rez, "Some Nuclear Optical Properties of Crystals of the KDP Group", *Soviet Phys. JETP* 26, pp. 33-37 (1968).
6. J. E. Pearson, G. A. Evans, and A. Yariv, "Measurement of the Relative Nonlinear Coefficients of KDP, RDP, RDA, and  $\text{LiIO}_3$ ", *Opt. Comm.* 4, pp. 366-367 (1972).
7. G. D. Boyd, R. C. Miller, K. Nassau, W. L. Bond, and A. Savage, " $\text{LiNbO}_3$ : An Efficient Phase Matchable Nonlinear Optical Material", *Appl. Phys. Lett.* 5, pp. 234-236 (1964).
8. J. E. Bjorkholm, "Relative Signs of the Optical Nonlinear Coefficients  $d_{31}$  and  $d_{22}$  in  $\text{LiNbO}_3$ ", *Appl. Phys. Lett.* 13, pp. 36-37 (1968).
9. R. C. Miller and A. Savage, "Temperature Dependence of the Optical Properties of Ferroelectric  $\text{LiNbO}_3$  and  $\text{LiTaO}_3$ ", *Appl. Phys. Lett.* 9, pp. 169-171 (1966).

10. R. Bechmann and S. K. Kurtz, "Second Harmonic Generation in Crystalline Solids" in Landolt-Börnstein, Group III: Crystal and Solid State Physics, Vol. 1 (Springer-Verlag, Berlin, 1970), pp. 167-232.
11. F. R. Nash, J. G. Bergman, G. D. Boyd, and E. H. Turner, "Optical Nonlinearities in  $\text{LiIO}_3$ ", J. Appl. Phys. 40, pp. 5201-5206 (1969).
12. S. Singh, D. A. Draegert, and J. E. Geusic, "Optical and Ferroelectric Properties of Barium Sodium Niobate", Phys. Rev. B2, pp. 2709-2724 (1970).
13. K. F. Hulme, O. Jones, P. H. Davies, and M. V. Hobden, "Synthetic Proustite ( $\text{Ag}_3\text{AsS}_3$ ): A New Crystal for Optical Mixing", Appl. Phys. Lett. 10, pp. 133-135 (1967).
14. W. B. Gandrud, G. D. Boyd, J. H. McFee, and F. H. Wehmeier, "Nonlinear Optical Properties of  $\text{Ag}_3\text{SbS}_3$ ", Appl. Phys. Lett. 16, pp. 59-61 (1970).
15. R. C. Miller, "Optical Second Harmonic Generation Piezoelectric Crystals", Appl. Phys. Lett. 5, pp. 17-19 (1964).
16. C. K. N. Patel, "Optical Harmonic Generation in the Infrared Using a  $\text{CO}_2$  Laser", Phys. Rev. Lett. 16, pp. 613-616 (1966).
17. A. Yariv, Quantum Electronics (John Wiley and Sons, New York, 1967), Chap. 21.
18. D. A. Kleinman, "Nonlinear Dielectric Polarization in Optical Media", Phys. Rev. 126, pp. 1977-1979 (1962).

Appendix II

Mode-Coupling Coefficients  
for Parametric Interactions

In any process which involves the mixing of two or more waves, the strength of the interaction depends on the spatial overlap of the interacting beams. It is also important for the beams to have nearly equal transverse amplitude and phase distributions. In three-wave parametric interactions, this requirement appears as an "overlap integral" as defined in Eq. (2.18). Since this integral multiplies the nonlinear coefficient, the gain of a parametric amplifier will be reduced if the transverse field distributions deviate from the optimum configuration. Such a reduction in gain will also produce a higher threshold in a parametric oscillator.

Since the present work concerns laser-pumped optical interactions, only light beams which can be described by confocal resonator theory [1,2] will be considered. In this case, the near-field, transverse (x,y) field distribution of a TEM<sub>mn</sub> mode at frequency  $\omega_j$  is given by [1,2]

$$\text{TEM}_{mn}(x,y) = u_j(x,y) = h_m(\alpha_j x) h_n(\alpha_j y) \exp\left[-\frac{\alpha_j^2}{2}(x^2+y^2)\right] \quad (\text{II.1})$$

where  $h_m(\alpha_j x)$  is a normalized hermite polynomial given by

$$h_m(\alpha_j x) = \frac{1}{N_{mj}} H_m(\alpha_j x) \quad (\text{II.2})$$

and

$$N_{mj}^2 = \int_{-\infty}^{\infty} H_m^2(\alpha_j x) e^{-(\alpha_j x)^2} dx = \frac{2^m m! \sqrt{\pi}}{\alpha_j} \quad (II.3)$$

The constant  $\alpha_j$  is given by

$$\alpha_j = \frac{\sqrt{2}}{W_j} \quad (II.4)$$

where  $W_j$  is the beam radius at  $\omega_j$ . In the near-field approximation, diffraction effects are neglected; in the most general case,  $\alpha$  will be complex and a function of  $z$  [3-5].

The functions  $u_j(x,y)$  in Eq. (II.1) satisfy the normalization condition, Eq. (2.15), and thus can be used to evaluate the overlap integral for three-wave parametric interactions. Asby [5] and Kingston and McWhorter [6] have calculated the overlap integral for the case of second-harmonic generation and the results of Ref. 5 could be extended to the three-wave case. The overlap integral for three-wave interactions is given by Eq. (2.18):

$$I = \int_{-\infty}^{\infty} \int_{-\infty}^{\infty} u_1(x,y) u_2(x,y) u_3(x,y) dx dy \quad (2.18)$$

Since  $u_j(x,y)$  is a product of independent functions of  $x$  and  $y$ , the double integral in Eq. (2.18) reduces to a product of single integrals given by

$$I = X_{lmn} Y_{pqr} \quad (II.5)$$

where

$$X_{\ell mn} = \int_{-\infty}^{\infty} h_{\ell}(\alpha_1 x) h_m(\alpha_2 x) h_n(\alpha_3 x) \exp\left[-\frac{x^2}{2}(\alpha_1^2 + \alpha_2^2 + \alpha_3^2)\right] dx . \quad (\text{II.6})$$

A similar expression can be written for  $Y_{pqr}$  .

In general,  $h_m(\alpha x)$  is an even or odd function of  $x$  depending on whether  $m$  is even or odd [7]. The overlap integral will thus be zero unless  $\ell+m+n$  and  $p+q+r$  are both even integers; not all possible mode combinations can mix in a three-wave interaction. Rather than treat the most general case of arbitrary mode orders in all 3 waves, only three cases will be considered here: (1) plane waves with no transverse variation; (2) Gaussian beams so  $\ell+m+n = p+q+r = 0$  ; (3) lowest order modes such that  $\ell+m+n$  and  $p+q+r$  equal 0 or 2. These three cases will correspond to most experimental conditions.

#### A. Plane Waves

An ideal plane-wave is infinite in extent, but physically even uniform beams are limited to a finite cross-section. Consider a uniform amplitude beam of cross-sectional area  $A$  . Equations (II.1) - (II.3) can be used to find

$$u_j = \left[ \int_{-\infty}^{\infty} \int_{-\infty}^{\infty} dx dy \right]^{-1/2} = \frac{1}{A^{1/2}} . \quad (\text{II.7})$$

Equation (2.18) then gives

$$I_{pw} = \frac{1}{A^{1/2}} . \quad (\text{II.8})$$

B. Gaussian Beams

For this case,  $h_m^2(\alpha x) = \alpha/\sqrt{\pi}$  and Eqs. (II.5) and (II.6) give

$$I_o = \frac{2\alpha_1\alpha_2\alpha_3}{\sqrt{\pi}(\alpha_1^2 + \alpha_2^2 + \alpha_3^2)} \quad (II.9)$$

By using Eq. (II.4), Eq. (II.8) can be expressed in terms of the mode spot sizes. The result is

$$I_o = 2\sqrt{\frac{2}{\pi}} \frac{W_1W_2W_3}{(W_1W_2)^2 + (W_1W_3)^2 + (W_2W_3)^2} \quad (II.10)$$

This result has previously been given by Boyd and Ashkin [8] and by Byer [9]. In the limit of equal confocal parameters\* ( $b_1 = b_2 = b_3 = b$ ) and nearly equal refractive indices ( $n = n_3 \approx n_1 \approx n_2$ ), Eq. (II.9) reduces to

$$I_o = 4\left(\frac{n}{b}\right)^{1/2} \frac{(\lambda_1\lambda_2\lambda_3)^{1/2}}{(\lambda_1\lambda_2 + \lambda_1\lambda_3 + \lambda_2\lambda_3)} \quad (II.11)$$

The condition  $b_1 = b_2 = b_3$  is the condition for optimum three-wave interaction if the fields at  $\lambda_1$  and  $\lambda_2$  share the same mirror surfaces [8,10].

The wavelength dependence of Eq. (II.10) can be simplified by defining  $\lambda_1$  and  $\lambda_2$  in terms of their deviation from degeneracy ( $\lambda_1 = \lambda_2 = 2\lambda_3$ ). Following Boyd and Kleinman [10],  $\lambda_1$  and  $\lambda_2$  are

---

\* For wavelength  $\lambda_j$ , index of refraction  $n_j$ , and spot size  $W_j$ , the confocal parameter is  $b_j = 2\pi n_j W_j^2 / \lambda_j$ .

written as

$$\lambda_1 = \frac{2\lambda_3}{1+\delta} \quad , \quad \lambda_2 = \frac{2\lambda_3}{1-\delta} \quad (\text{II.12})$$

where  $0 \leq \delta < 1$  . Equation (II.12) then becomes

$$I_o^2 = \frac{n(1 - \delta^2)}{\lambda_3 b} \quad . \quad (\text{II.13})$$

When  $\delta = 0$  , it is straightforward to show that  $I_o^2 = 1/2A_3 = I_{pw}^2/2$  where  $A_3 = \pi W_3^2$  is the area of the pump beam.

### C. Low-Order Gaussian Modes

The three lowest order normalized hermite functions are given by [7]

$$\begin{aligned} h_0(\alpha x) &= (\alpha/\sqrt{\pi})^{1/2} \\ h_1(\alpha x) &= (2\alpha/\sqrt{\pi})^{1/2} \alpha x \\ h_2(\alpha x) &= (2\alpha/\sqrt{\pi})^{1/2} [(\alpha x)^2 - \frac{1}{2}] \quad . \end{aligned} \quad (\text{II.14})$$

In the usual parametric oscillator experimental situation, the pump mode ( $\lambda_3$ ) is known and the signal ( $\lambda_1$ ) and idler ( $\lambda_2$ ) are determined by the optical resonator. Three cases of interest will be considered here: the pump mode is either  $TEM_{00}$ ,  $TEM_{10}$ , or  $TEM_{11}$  . For each case the value of  $I_o^2/I^2$  will give the increase in the threshold of a parametric oscillator from its minimum value. In all of the following discussion, the conditions  $n = n_3 = n_1 = n_2$  and  $b = b_1 = b_2 = b_3$  are assumed and Eq. (II.12) is used to express the results in terms of  $\delta$  .

Table II-1 shows the transverse mode threshold factor  $I_0^2/I^2$  for parametric oscillators driven by the three different pump modes. Where no value is given,  $I$  is zero because of the required symmetry on the modes ( $l+m+n$  and  $p+q+r$  are even integers). Note that occasionally there are two combinations of signal and idler modes which have the same threshold factor. Unless there is something in the parametric oscillator to discriminate against one combination, both will be driven by the pump. Since the independent transverse modes will share the pump power equally, the total oscillator threshold power will be increased by twice the factor given in the tables for a single combination of modes. At degeneracy ( $\delta = 0$ ) there are occasionally four mode combinations with the same threshold factor. The total oscillator threshold will then be four times that for a single combination of signal and idler modes.

Table II-1  
 THRESHOLD FACTORS  $I_0^2/I^2$  FOR VARIOUS COMBINATIONS OF  
 SIGNAL ( $u_1$ ), IDLER ( $u_2$ ), AND PUMP ( $u_3$ ) TRANSVERSE MODES

$u_3 = \text{TEM}_{00}$						
$u_1 \backslash u_2$	TEM <sub>00</sub>	TEM <sub>10</sub>	TEM <sub>01</sub>	TEM <sub>11</sub>	TEM <sub>20</sub>	TEM <sub>02</sub>
TEM <sub>00</sub>	1	-	-	-	$8/(1-\delta)^2$	$8/(1-\delta)^2$
TEM <sub>10</sub>	-	$4/(1-\delta^2)$	-	-	-	-
TEM <sub>01</sub>	-	-	$4/(1-\delta^2)$	-	-	-
TEM <sub>11</sub>	-	-	-	$16/(1-\delta^2)^2$	-	-
TEM <sub>20</sub>	$8/(1+\delta)^2$	-	-	-	$64/9(1-\delta^2)$	$16/(1-\delta^2)^2$
TEM <sub>02</sub>	$8/(1+\delta)^2$	-	-	-	$16/(1-\delta^2)^2$	$64/9(1-\delta^2)$
$u_3 = \text{TEM}_{10} \text{ or } [\text{TEM}_{01}]$						
TEM <sub>00</sub>	-	$2/(1+\delta)$	$[2/(1+\delta)]$	-	-	-
TEM <sub>10</sub>	$2/(1-\delta)$	-	-	$[8/(1+\delta)(1-\delta^2)]$	-	$16/(1-\delta)^3$
TEM <sub>01</sub>	$[2/(1-\delta)]$	-	-	$8/(1+\delta)(1-\delta^2)$	$[16/(1-\delta)^3]$	-
TEM <sub>11</sub>	-	$[8/(1-\delta)(1-\delta^2)]$	$8/(1-\delta)(1-\delta^2)$	-	-	-
TEM <sub>20</sub>	-	-	$[16/(1+\delta)^3]$	-	-	-
TEM <sub>02</sub>	-	$16/(1+\delta)^3$	-	-	-	-
$u_3 = \text{TEM}_{11}$						
TEM <sub>00</sub>	-	-	-	$4/(1+\delta)^2$	-	-
TEM <sub>10</sub>	-	-	$4/(1-\delta^2)$	-	-	-
TEM <sub>01</sub>	-	$4/(1-\delta^2)$	-	-	-	-
TEM <sub>11</sub>	$4/(1-\delta)^2$	-	-	-	-	-

Appendix II

References

1. G. D. Boyd and J. P. Gordon, "Confocal Multimode Resonator for Millimeter through Optical Wavelength Masers", Bell Syst. Tech. J. 40, pp. 489-508 (1961).
2. G. D. Boyd and H. Kogelnik, "Generalized Confocal Resonator Theory", Bell Syst. Tech. J. 41, pp. 1347-1369 (1962).
3. H. Kogelnik and T. Li, "Laser Beams and Resonators", Appl. Opt. 5, pp. 1550-1567 (1966).
4. H. Kogelnik, "Coupling and Conversion Coefficients for Optical Modes", in Proceedings of Symp. Quasi-Optics (Polytechnic Press, Brooklyn, 1964), pp. 333-347.
5. R. Asby, "Optical-Mode Interaction in Nonlinear Media", Phys. Rev. 187, pp. 1062-1069 (1969).
6. R. H. Kingston and A. L. McWhorter, "Electromagnetic Mode Mixing in Nonlinear Media", Proc. IEEE 53, pp. 4-12 (1965).
7. M. Abramowitz and I. A. Stegun, Handbook of Mathematical Functions (U.S. Government Printing Office, Washington, D. C., 1964), Chap. 22.
8. G. D. Boyd and A. Ashkin, "Theory of Parametric Oscillator Threshold with Single-Mode Optical Masers and Observation of Amplification in  $\text{LiNbO}_3$ ", Phys. Rev. 146, pp. 187-198 (1966).
9. R. L. Byer, "Parametric Fluorescence and Optical Parametric Fluorescence", Ph.D. Thesis (available as M.L. Report No. 1711), Stanford University, 1968.
10. G. D. Boyd and D. A. Kleinman, "Parametric Interaction of Focused Gaussian Light Beams", J. Appl. Phys. 39, pp. 3597-3639 (1968).

Appendix III

Optimum Laser Output Coupling Using Internal  
Optical Parametric Oscillation

Extraction of the maximum optical power from a laser is a very important practical problem. If the optical output coupling is too low, most of the laser power is contained within the optical resonator and little is available as useful output. If the coupling is too high, the laser threshold is high and most of the gain in the laser medium is used to overcome this threshold. Again, there is little useful optical power output. Somewhere in between these two extremes there is an optimum value for the output coupling which gives maximum laser output.

The traditional way to couple power out of a laser is to use a partially-transmitting mirror. The optimum mirror transmission is related to the laser gain and saturation parameters and to the losses other than output coupling [1]. Two other useful methods of coupling the power out of a laser are acoustic deflection [2] and second-harmonic generation [3,4]. Acoustic deflection can give high repetition rates for pulsed operation and second-harmonic generation extracts the laser power at a higher frequency than in normal laser operation. Both methods can provide optimum laser coupling.

An alternate method of output coupling for a laser is to use an optical parametric oscillator (OPO). The method is similar to internal-cavity second-harmonic generation, but with the OPO, the laser energy appears in two lower frequencies which are tunable. Consider the system

shown schematically in Fig.III-1. The laser and the OPO have separate optical cavities, but they coincide inside the nonlinear crystal. In practice such a system could be achieved by using dispersing prisms inside the resonators. The steady-state behavior of a doubly-resonant

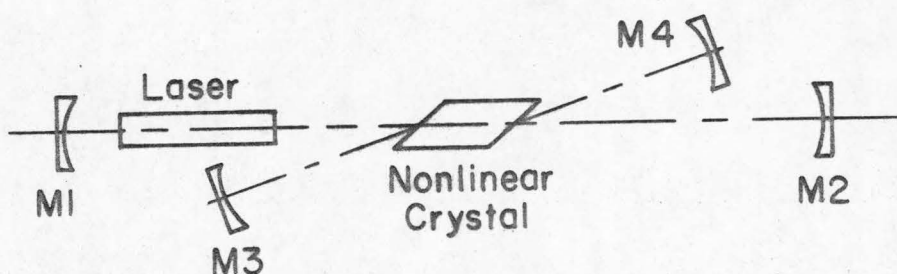


Figure III-1. Schematic of possible internal OPO configuration. The laser cavity (M1,M2) is separate from the OPO cavity (M3,M4) except over the length of the nonlinear crystal.

internal OPO has been discussed by Oshman and Harris [5], and Falk, et al [6] have analyzed the pulsed operation of the device.

To demonstrate the use of an internal OPO as a laser output coupler, the simplest case to consider is a steady-state singly-resonant oscillator (SRO). The procedure is to use a self-consistent Fabry Perot analysis similar to that in Chap. 4. By solving for the laser field in the presence of the steady state SRO, the condition for optimum coupling can be found.

Consider the system shown in Fig.III-1 and take the signal field ( $\omega_1$ ) to be resonant in the OPO. In steady-state operation this field will be very large. Assuming that the roundtrip OPO gain is small,

the signal field is assumed to be nearly constant over the length of the nonlinear crystal. In this approximation, the pump ( $\omega_3$ ) and idler ( $\omega_2$ ) fields at the "output" of the nonlinear crystal are given in terms of the input values by [7]

$$(a) \quad A_2(l) = A_3(0)\sin\beta l \quad (III.1)$$

$$(b) \quad A_3(l) = A_3(0)\cos\beta l$$

where

$$\beta^2 = \Gamma^2 A_3^2 \quad (III.2)$$

and all other quantities are defined in Chap. 2. For simplicity, all losses are neglected, perfect phase-matching is assumed ( $\Delta k = 0$ ), and the relative phase of the three waves taken as  $\Delta\phi = \pi/2$  (see Chap. 2, Eqs. (2.17) and (2.21)).

For low gain lasers with large saturation powers such as Nd:YAG, the pump field in the laser medium is described by

$$\begin{aligned} \frac{dA_3}{dz} &= -\alpha_3 A_3 + g_0 \frac{A_3}{\left(1 + \frac{\omega_3}{n_3^2 S} A_3^2\right)} \\ &\approx -\alpha_3 A_3 + g_0 A_3 \left(1 - \frac{\omega_3}{n_3^2 S} A_3^2\right) \end{aligned} \quad (III.3)$$

where  $g_0$  is the small-signal gain and  $\alpha_3$  is the loss per unit length in the laser medium, and  $S$  is the electric-field saturation parameter [1]. The index of refraction in the laser material is  $n_3$ . By

defining new constants as

$$\begin{aligned} \gamma &= g_0 - \alpha_3 \\ \xi &= \frac{g_0 \omega_3}{S n_3} \end{aligned} \quad , \quad (III.4)$$

Eq. (III.3) becomes

$$\frac{dA_3}{dz} = \gamma A_3 - \xi A_3^3 \quad . \quad (III.5)$$

The solution to Eq. (III.5) for a gain medium of length  $L$  is

$$A_3^2(L) = \frac{\gamma/\xi}{1 + c_0 e^{-2\gamma L}} \quad (III.6)$$

where

$$c_0 = \frac{\gamma}{\xi A_3^2(0)} - 1 \quad .$$

Now assume an initial field intensity  $A_{30}^2$  next to mirror 1 in the pump laser resonator and traveling to the right (see Fig. (III-1)). The laser mirrors have intensity reflection coefficients  $R_1$  and  $R_2$  and the OPO mirrors both have a transmission  $T$  at the laser frequency. The pump field is computed at each point in the cavity for one complete round-trip and self-consistency requires that the resultant field equal the assumed initial field. This procedure gives

$$(1 - e^{-2\gamma L}) \left[ 1 + \frac{e^{-2\gamma L}}{R_2 T^2 \cos^4 \beta L} \right] A_{30}^2 + \frac{\gamma e^{-4\gamma L}}{\xi R_2 T^2 \cos^4 \beta L} = R_1 \frac{\gamma}{\xi} \quad . \quad (III.7)$$

If the OPO is not present,  $T = 1$  and  $\beta = 0$ . Considering  $R_2$  as the laser "output" mirror gives

$$P_{\text{out}} \propto (1-R_2)A_3^2 = \frac{\gamma(1-R_2)(R_1R_2e^{-4\gamma L})}{R_2\xi(1-e^{-2\gamma L})(R_1+e^{-2\gamma L})} \quad (\text{III.8})$$

where Eq.(III.6) has been used to find the last relation. The output power will be maximum when

$$\begin{aligned} (R_2)_{\text{opt}} &= \frac{e^{-2\gamma L}}{R_1^{\frac{1}{2}}} \\ &\approx 1 - 2\gamma L \end{aligned} \quad (\text{III.9})$$

This is the same result given in Ref. 1 for low gain and large saturation parameter. The approximate expression is valid for  $2\gamma L \ll 1$  (low gain laser) and  $R_1 \approx 1$ . with  $R_2$  given by Eq.(III.9), the laser output is

$$\begin{aligned} P_{\text{out}} &\propto \frac{\gamma(R_1^{\frac{1}{2}} - e^{-2\gamma L})^2}{\xi(1-e^{-2\gamma L})(R_1+e^{-2\gamma L})} \\ &\approx \frac{\gamma^2 L}{\xi(1-\gamma L)} \end{aligned} \quad (\text{III.10})$$

From Eqs.(III.7) and (III.9) it is clear that the OPO can provide optimum laser coupling if

$$R_2^{\dagger} = R_2 T^2 \cos^4 \beta L = \frac{e^{-2\gamma L}}{R_1^{\frac{1}{2}}} \approx 1-2\gamma L \quad (\text{III.11})$$

The laser power output will still be given by Eq.(III.10) but will now be at the lower OPO frequencies. In the limits that  $R_1, R_2 \approx 1$ , and  $\gamma L, \beta l \ll 1$ , Eq.(III.11) gives the resonant signal power as

$$P_1 \propto A_1^2 = \frac{[\gamma L - 2(1 - T^{\frac{1}{2}})]}{(\Gamma L)^2 T^{\frac{1}{2}}} . \quad (\text{III.12})$$

Optimum laser coupling using an internal OPO has recently been reported by Ammann [8]; 100% of the available average laser power was observed in the parametric frequencies.

Appendix III

References

1. W. W. Rigrod, "Gain Saturation and Output Power of Optical Masers", J. Appl. Phys. 34, pp. 2602-2609 (1963).
2. D. Maydan, "Fast Modulator for Extraction of Internal Laser Power", J. Appl. Phys. 41, pp. 1552-1559 (1970).
3. J. E. Geusic, H. J. Levinstein, S. Singh, R. G. Smith, and L. G. Van Vliet, "Continuous 0.532 $\mu$  Solid-state Source Using Ba<sub>2</sub>Nb<sub>5</sub>O<sub>15</sub>", Appl. Phys. Lett. 12, pp. 306-308 (1968).
4. R. G. Smith, "Theory of Intracavity Optical Second-Harmonic Generation", IEEE J. Quant. Electr. QE-6, pp. 215-223 (1970).
5. M. K. Oshman and S. E. Harris, "Theory of Optical Parametric Oscillation Internal to the Laser Cavity", IEEE J. Quant. Electr. QE-4, pp. 485-502 (1968).
6. J. Falk, J. M. Yarborough, and E. O. Ammann, "Internal Optical Parametric Oscillation", IEEE J. Quant. Electr. QE-7, pp. 359-369 (1971).
7. L. B. Kreuzer, "Single and Multi-Mode Oscillation of the Singly-Resonant Optical Parametric Oscillator", Proc. Joint Conf. Lasers and Opto-Electronics (Univ. of Southampton, I.E.R.E., London), pp. 52-63 (1969).
8. E. O. Ammann, "3- to 5- Micron Parametric Oscillator", GTE Sylvania Inc., Mountain View, Calif. 94040, Report No. AFAL-TR-72-13, Jan. 1972.